G-CSF SECRETED BY EPIGENETICALLY REPROGRAMMED MUTANT IDH1 GLIOMA STEM CELLS REVERSES THE MYELOID CELLS'-MEDIATED IMMUNOSUPPRESSIVE TUMOR MICROENVIRONMENT

Mahmoud S Alghamri[1,2], Ruthvik P Avvari[1,2], Rohit Thalla[1,2], Neha Kamran[1,2], Li Zhang[1,2], Maria Ventosa[1,2], Ayman Taher[1,2], Syed Mohd Faisal[1,2], Felipe J. Núñez[1,2†], María Belén Garcia-Fabiani[1,2], Santiago Haase[1,2], Stephen Carney[1,2], Daniel Orringer[1#], Shawn Hervey-Jumper[3], Jason Heth[1], Parag G Patil[1], Wajd N Al-Holou[1], Karen Eddy[1], Sophia Merajver[4], Peter J Ulintz[4], Joshua Welch[5], Chao Gao[5], Jialin Liu[5], Gabriel Núñez[6], Dolores Hambardzumyan[7], Pedro R Lowenstein[1,2,8] and Maria G Castro[1,2,8*]

[1] Department of Neurosurgery, University of Michigan Medical School, Arbor, MI 48109, USA.

[2] Department of Cell and Developmental Biology, University of Michigan Medical School, Ann Arbor, MI 48109, USA.

[3] Department of Neurosurgery, University of California San Francisco, USA.

[4] Department of Internal Medicine, University of Michigan Medical School, Ann Arbor, MI 48109, USA.

[5] Department of Computational Medicine and Bioinformatics, University of Michigan Medical School Ann Arbor, MI 48109, USA

[6] Department of Pathology, University of Michigan Medical School, Ann Arbor, MI 48109, USA

[7] Department of Oncological Sciences, The Tisch Cancer Institute and Department of Neurosurgery, Mount Sinai Icahn School of Medicine, New York, NY, USA

[8] Rogel Cancer Center, University of Michigan, Ann Arbor, MI 48109, USA

[#] Current address: Department of Neurosurgery, New York University, New York, NY, USA

[†] Current Address: Leloir Institute Foundation, Buenos Aires, Argentina

***CORRESPONDENCE:** Maria G Castro, Room 4570C, MSRB II, 1150 West Medical Center Drive, Michigan Medicine, Ann Arbor, MI 48109 e-mail: mariacas@umich.edu

Running title: Immune-permissive myeloid cells in the *mIDH1* glioma microenvironment

Keywords: Glioma microenvironment, IDH1, Epigenetic, G-CSF, Myeloid-Derived Suppressor Cells

ABSTRACT

Mutation in isocitrate dehydrogenase (*mIDH*) is a gain of function mutation resulting in the production of the oncometabolite, R-2-hydroxyglutarate, that inhibits DNA and histone demethylases. The resultant hypermethylation phenotype reprograms the glioma cells' transcriptome and elicits profound effects on glioma immunity. We report that in mouse models and human gliomas, *mIDH1* in the context of *ATRX* and *TP53* inactivation results in global expansion of the granulocytic myeloid cells' compartment. Single-cell RNA-sequencing coupled with mass cytometry analysis revealed that these granulocytes are mainly non-immunosuppressive neutrophils and pre-neutrophils; with a small fraction of polymorphonuclear myeloid-derived suppressor cells. The mechanism of *mIDH1* mediated pre-neutrophils expansion involves epigenetic reprogramming which leads to enhanced expression of the granulocyte colony-stimulating factor (G-CSF). Blocking G-CSF restored the inhibitory potential of PMN-MDSCs and enhanced tumor progression. Thus, G-CSF induces remodeling of the inhibitory PMN-MDSCs in *mIDH1* glioma rendering them non-immunosuppressive; and having significant therapeutic implications.

SIGNIFICANCE

mIDH1 is the most common mutation in gliomas associated with improved prognosis. Gliomas harboring *mIDH1*, together with *ATRX* and *TP53* inactivation, exhibit higher circulating levels of G-CSF, ensuing the recruitment and expansion of non-suppressive neutrophils, pre-neutrophils and small fraction of PMN-MDSCs to the TME leading to an immune permissive phenotype.

INTRODUCTION

Mutation in isocitrate dehydrogenase (*mIDH*) is a common genetic lesion occurring in adult glioma patients (1). Approximately 90% of *IDH1* mutations occur in exon 4 at codon 132, resulting in a change of a single amino acid from arginine to histidine (R132H). Less common *IDH2* mutations occur in an analogous codon at position R172 (2). Although IDH1/2 mutations are always heterozygous, they exert a dominant gain of function enzymatic activity which leads to the production of 2-hydroxyglutarate (2HG). Excessive 2HG production causes DNA hypermethylation via inhibition of methylcytosine dioxygenase *TET2* (3,4), and also promotes histone hypermethylation through competitive inhibition of α-ketoglutarate (αKG)-dependent Jumonji-C histone demethylases (5,6). This leads to epigenetic reprogramming of gene expression within the *mIDH1* glioma cells (5,7,8).

The *IDH1* mutation plays an important role in glioma development and progression, by modulating tumor cells' intrinsic mechanisms and also by remodeling the tumor microenvironment. Metabolically, IDH1 is one of the enzymes that encodes an irreversible reaction in the tricyclic acid cycle. Disruption of the IDH reaction results in defective mitochondrial oxidative phosphorylation, glutamine metabolism, lipogenesis, glucose sensing, and altering cellular redox status (9-14). Mutation in *IDH1* also inhibits glioma stem cell differentiation (5,13), upregulates vascular endothelial growth factor (15,16), and produces high levels of hypoxia-inducible factor-1α, all of which promote glioma invasion (14,17,18). We have recently shown that *mIDH1* when expressed concomitantly with *ATRX* and *TP53* inactivation, results in enhanced DNA damage response, leading to radio-resistance in mouse and human glioma cells *in vitro* and extending the median survival (MS) in a genetically engineered mouse

glioma model (19). Nevertheless, the molecular mechanisms that mediate enhanced survival in patients with *mIDH1* glioma remain elusive. We hypothesize that epigenetic-mediated mechanisms could be an important contributing factor modulating the immune microenvironment

The success of immunotherapeutic approaches in several non-central nervous system (CNS) cancers has driven the evaluation of numerous immune-mediated therapeutic strategies in glioma clinical trials (20). To date, Immune checkpoint blockade used as a monotherapy in combination with standard of care did not demonstrate survival benefits in glioma patients (21-23). The lack of therapeutic efficacy of immunotherapies in the clinical arena, can be attributed in part, to the immunosuppressive properties elicited by glioma infiltrating immune cells (22-24). Myeloid-derived suppressor cells (MDSCs) have emerged as one of the dominant immunosuppressive cells that directly interfere with the efficacy of immunotherapy (25-27). In glioma patients, it has been demonstrated that granulocytic-MDSCs (also known as PMN-MDSCs) are a major subset that expands during glioma progression which negatively correlates with patient's survival (28-30). We have recently shown that depletion of MDSCs in wild-type *IDH1* glioma-bearing mice markedly enhanced the efficacy of an immune stimulatory/conditional cytotoxic gene therapy (25); highlighting the role of MDSCs in hampering anti-glioma immunity.

Several studies suggested that *mIDH1* may play a critical role in shaping the immunological landscape of the tumor microenvironment (31-34). Glioma samples from patients with *mIDH1* have decreased PD-L1 expression (due to hypermethylation of the CD274 promoter) (32),

reduced level of inflammation, and reduced levels of infiltrating immune cells (31,33,35). Myeloid cells represent the major immune cells in glioma TME (25,36,37). It has been shown that *mIDH1* glioma with mixed genetic background (*PDGFB/shP53/ Ink4a/Arf*$^{-/-}$*/mIDH1*) exhibit fewer tumor-infiltrating macrophages, dendritic cells (DCs), and neutrophils, compared to the wild-type *IDH1* counterparts (31). Nevertheless, the impact of *mIDH1* on tumor-infiltrating myeloid cells' phenotype and function have not been explored; particularly in the context of concurrent inactivation mutation in *ATRX* and *TP53* (1,38).

Granulocytes are the major population within the bone marrow (BM) myeloid cells' compartment, which differentiate under steady-state conditions into neutrophils. Under physiological conditions, these cells have emerged as major contributors to protection against pathogens and are important mediators of tissue remodeling (39,40). However, during inflammation and cancer, the activation of various signaling pathways, such as Jak-Stat, and MAPK pathways, results in rapid mobilization of granulocytes and neutrophils from the BM, favoring the generation of immunosuppressive PMN-MDSCs (41-43). These cells share the same origin (granulocyte-macrophage progenitors (GMPs)) and differentiation pathways, yet, PMN-MDSCs have distinct genomic and biochemical features and are immunosuppressive (44,45). Therefore, it became critical to incorporate both transcriptomic analysis at the single-cell level (single-cell RNA sequencing) as well as functional characterization to uncover the immunosuppressive tumor-infiltrating PMN-MDSCs in glioma.

We report that in genetically engineered mouse glioma models, *IDH1* mutation, in the context of *ATRX* and *TP53* deficiency, caused an expansion of tumor-infiltrating granulocytes.

Upon phenotypic and functional characterization, we uncovered that granulocytes in *mIDH1* glioma, counter to the granulocytes infiltrated in *wtIDH1*, did not exhibit immune-suppressive properties. Single-cell sequencing coupled with mass cytometry analysis revealed that these granulocytes are heterogeneous and composed of neutrophils and pre-neutrophils, with a smaller proportion of *bona fide* immunosuppressive PMN-MDSCs. Moreover, primary human gliomas showed a higher frequency of cells exhibiting the PMN-MDSCs gene signature in *wtIDH1* tumors when compared to *mIDH1* glioma. Our data demonstrate that the mechanism by which *mIDH1* in glioma mediates the expansion of non-immune suppressive granulocytes involves epigenetic reprogramming. This leads to enhanced expression of granulocyte colony-stimulating factor (G-CSF) by stem-like *mIDH1* glioma cells. Blocking G-CSF restored the inhibitory potential of PMN-MDSCs and substantially enhanced tumor progression, whereas recombinant G-CSF administration, prolonged the MS of *wtIDH1* glioma bearing mice. Consistent with that, LGG-astrocytoma with *mIDH1* is the sole tumor cohort within all TCGA data sets in which high *CSF3* gene expression correlates with favorable patients' outcome. Our work provides a new insight of the impact of *mIDH1* on the phenotypic and functional properties of myeloid cells in the glioma TME.

RESULTS

mIDH1 glioma causes a systemic increase in polymorphonuclear (PMN) myeloid cells

The role of *IDH1* mutation in shaping the immune landscape of glioma remains unexplained. We generated a *mIDH1* genetically engineered mouse model (GEMM) of glioma using the Sleeping Beauty (SB) transposon system (46-48) to uncover the impact of $IDH1^{R132H}$ in the context of ATRX and TP53 deficiency on glioma infiltrating immune cells (Fig. 1A). Two groups of tumors were generated using the SB method, each contains a combination of genetic lesions commonly encountered in astrocytoma; *mIDH1* (*NRASG12V*+ *shp53* + *shATRX* + $mIDH1^{R132H}$) and control *wtIDH1* group (*NRASG12V*+ *shp53* + *shATRX* + *wtIDH1*) (Fig. 1B). We used the merit of mass cytometry (CyTOF) (Supplementary Table S1) which measures 37 parameters simultaneously to analyze immune cell composition within the TME from each group. Using SPADE analysis, we found that glioma TME contains several immune cell types including macrophages, dendritic cells (DCs), B-cells, NK cells, $CD8^+$ T-cells, and $CD4^+$ T-cells (Fig. 1C, D). Moreover, there was an expansion of cells (depicted by the large red/yellow nodes) characteristic for myeloid-derived suppressor cells ($CD45^{high}/CD11b^+/Gr\text{-}1^+$) in the TME of *mIDH1* glioma compared to *wtIDH1* glioma (Fig. 1C, D). Similarly, visual inspection of viSNE plots, which represent high-dimensional CyTOF output in two dimensions (49), showed a higher percentage of $Gr\text{-}1^+$ cells in the TME from *mIDH1* glioma compared to those from *wtIDH1* glioma (Fig. 1C, D; insets). We confirmed that this difference is statistically significant using a χ^2 test ($p < 0.0001$). The Gr-1 antibody can detect both the granulocytic ($CD45^{high}/CD11b^+/Ly6G^+/Ly6C^{low}$) and monocytic ($CD45^{high}/CD11b^+/Ly6G^-/Ly6C^{high}$) MDSCs population. We found that the majority of the expanded myeloid cells in *mIDH1* tumor belonged to the granulocytic population, with no changes in the frequency of the monocytic population

(Supplementary Fig S1A). In addition to the increase in granulocytes, *mIDH1* tumors showed a decreased frequency of macrophages (2.7 fold) and dendritic cells ((DCs) ~ 4 fold) with no significant change in the frequency of lymphocytes (including NK cells, B-cells, $CD8^+$ and $CD4^+$ T-cells) as compared to *wtIDH1* tumors (Supplementary Fig. S1B-G). Notably, there was no significant difference in the percentage of $CD45^+$ cells between *wtIDH1* and *mIDH1* glioma (Supplementary Fig. S1H). We generated neurospheres (NS) from mouse glioma subgroups (Fig 1B), and we used the implantable animal model to analyze the frequency of $CD45^{high}/CD11b^+/Gr\text{-}1^+$ population at mid-stage (12 days after implantation) and at symptomatic stage of tumor development (Fig 1E, F). In both time points, we found that the *mIDH1* tumor group had an increased number and percentage of $CD45^{high}/CD11b^+/Gr\text{-}1^+$ cells compared to the *wtIDH1* group (Mid-stage: 6.91 ± 1.4% vs. 17.52 ± 3.6%, Symptomatic stage: 32.5 ± 4.07% vs. 73.9 ± 4.6% in *wtIDH1*vs *mIDH1*; respectively, Fig. 1E, F; Supplementary Fig. S2A); the majority of these cells belong to granulocytic ($Ly6G^+$) origin (Fig. 1G). We validated our results using an animal model of *mIDH1* glioma independent of *RAS* activating mutation (36,50). Brain tumors were induced with replication-competent avian leukemia virus splice acceptor (RCAS) expressing platelet-derived growth factor β (*PDGFB*), *shP53*, and *mIDH1* or *wtIDH1* in mixed background *NTva_Ink4a*/*Arf* $^{-/-}$ mice. The neurospheres generated from these tumors were engineered to encode *shATRX* to generate glioma cells with the following molecular alterations: *PDGFB/shP53/shATRX/Ink4a/Arf*$^{-/-}$*/mIDH1* or *PDGFB/shP53/shATRX/Ink4a/Arf*$^{-/-}$*/wtIDH1 (46)*. Using this additional GEMM, we confirmed that *mIDH1* tumor-bearing animals exhibit an expanded $CD45^{high}/CD11b^+/Gr\text{-}1^+$ population with a high predominance of $CD45^{high}/CD11b^+/Ly6G^+$ population (~2-fold, $P<0.001$; Supplementary Fig. S2D, E). The expansion of $CD45^{high}/CD11b^+/Gr\text{-}1^+$ cells was not limited to the tumor site; in both the

circulation and the spleen of *mIDH1* tumor-bearing animals, there was a higher (*P<0.005*) number and percentage of $CD45^{high}/CD11b^{+}/Gr\text{-}1^{+}$ (Blood; 17.65 ± 2.3% vs. 50.05 ± 4.4%, spleen; 26.6 ± 2.7 vs. 66.8 ± 5.4% in *wtIDH1* vs *mIDH1* tumor, respectively), the majority of which belong to granulocytic origin (Fig. 1H-M, Supplementary Fig. S2B, C). Similar to the TME, in the circulation and spleen from tumor-bearing animals, there was no significant difference in the M-MDSCs between *wtIDH1* and *mIDH1* glioma bearing mice. However, *mIDH1* exhibited a decreased number of macrophages, with no differences in the DCs or lymphocytes (Supplementary Fig. S3, 4). Collectively, these results suggest that *mIDH1* tumor causes activation of pathways involved in granulocytic myeloid cells' expansion.

***mIDH1* glioma development results in profound remodeling of BM hematopoiesis**

The expansion of the granulocytic myeloid cells within the TME, blood, and spleen suggested that *mIDH1* tumor growth induces profound alterations in the bone marrow (BM) hematopoiesis. Therefore, we examined the changes in hematopoiesis within the BM and spleen of the SB-induced murine glioma model. The absolute number and relative proportion of hematopoietic stem cells (HSCs) were decreased in the BM from *mIDH1* tumor-bearing mice (2.2-fold, $p < 0.05$, Fig. 2A, B). In contrast, BM from *mIDH1* tumors contained higher numbers and frequencies of myeloid progenitors (MPs) (%MP ~35%, $p < 0.05$, Fig. 2C). In the spleen, there were no differences in the frequency of HSCs between the *wtIDH1* and *mIDH1* tumor-bearing animals (Supplementary Fig. S5A, B). However, spleens from *mIDH1* tumor-bearing animals showed more than two-fold increase in MPs compared to *wtIDH1* tumors (*P<0.05*, Supplementary Fig. S5A, C). There was also a higher frequency (2-fold) of granulocyte-macrophage precursors (GMPs) in both the BM and spleen of *mIDH1* tumor-bearing animals (*P<0.05*, Fig. 2D, Supplementary Fig. S5D, F). Despite the increase in MPs and GMPs, there

was no significant change in the frequency of common lymphocyte progenitors (CLPs) between the two groups (Fig. 2E, Supplementary Fig. S5E, G). The increased production of granulocytes, MPs, and GMPs in BM and spleen supports the activation of the granulocytic myeloid differentiation pathway in the *mIDH1* tumor-bearing animals (Fig. 2F).

Molecular and functional characterization of *mIDH1* tumor-infiltrating granulocytes

A hallmark of the glioma microenvironment is the accumulation of immunosuppressive immune cells, which in part is elicited by MDSCs infiltration in the tumor (25). Thus, we investigated the molecular and functional characteristics of the expanded $CD45^{high}/CD11b^{+}/Ly6G^{+}$ in *mIDH1* tumors. First, we examined the surface expression of T-cell suppressive/co-stimulatory molecules commonly expressed by PMN-MDSCs in *wtIDH1*, and *mIDH1* tumors. Interestingly, in the $CD45^{high}/CD11b^{+}/Ly6G^{+}$ cells from *mIDH1* TME, the expression level of immunosuppressive as well as costimulatory molecules, such as PD-L1, CD86, CD80, IL-4Rα, iNOS, and Arginase1, was lower compared to the $Ly6G^{+}$ cells from *wtIDH1* TME (Fig. 2 H-M). In order to characterize the molecular differences between mIDH1 and wtIDH1 tumor-infiltrating $CD45^{high}/CD11b^{+}/Gr\text{-}1^{+}$, we purified these cells from tumor-bearing animals of these two groups, and performed transcriptome analysis. Granulocytes from *mIDH1* tumors have decreased expression of all immunosuppressive genes associated with the PMN-MDSCs signature, such as *Il1β*, *Arg1*, *Tgfb1*, *CD274*, and *Stat3* (Fig. 2G). Genes which mediate innate immunity, such as *tlr2*, *tlr7*, and *tlr8*, as well as antigen presentation and processing, were upregulated in granulocytes from *mIDH1* TME (Supplementary Fig. S6A). To further investigate the functions of the differentially expressed genes, we performed gene set enrichment analysis (GSEA) (51). The most significantly enriched gene sets in the *mIDH1* group were related to the immune response (Supplementary Fig. 6B). *Tlr7*, *tlr8*, and *tlr13* were upregulated, whereas

genes important for monocyte differentiation (*cebp-β*, and *Irf8)*, as well as immunosuppressive genes in myeloid cells (*Il1β*, and *Arg1*), were downregulated (Supplementary Fig. 6B). Collectively, these results suggest that the expanded granulocytes in *mIDH1* tumor exhibit downregulation of immunosuppressive PMN-MDSCs gene signature.

Immunosuppressive PMN-MDSCs are characterized by their ability to suppress T cells' expansion, therefore we examined the influence of tumor-infiltrating $CD45^{high}/CD11b^{+}/ Ly6G^{+}$ myeloid cells on antigen-specific T-cell proliferation. We isolated granulocytes by flow cytometry from gliomas expressing *wtIDH1* or *mIDH1* and co-cultured them with carboxyfluorescein diacetate succinimidyl ester (CFSE)-labeled splenocytes from OT-1 mice (Fig. 2N). Isolated granulocytes were next stimulated with the cognate ova albumin peptide SIINFEKL (SIIN) to induce OT-1 splenocyte proliferation (Fig. 2N) (52). In response to SIIN, T-cells proliferation spiked to ~90 ± 4.9% in the control condition (T+ SIIN) (Fig. 2 O, P). When $CD45^{high}/CD11b^{+}/Ly6G^{+}$ myeloid cells from the TME of *wtIDH1* tumors were added to the culture at different ratios (1:1, 2:1, 4:1), the percentage of proliferating T-cells was reduced to ~48%, 64%, and 75%, respectively ($P<0.001$; Fig. 2O, P). Interestingly, $CD45^{high}/CD11b^{+}/Ly6G^{+}$ cells isolated from the TME of *mIDH1* gliomas did not suppress antigen-specific T-cell proliferation at any co-culturing ratio (Fig. 2O, P). Together, these results suggest that the granulocytes from the *wtIDH1* tumor are inhibitory and thus can be defined as PMN-MDSCs, whereas the expanded granulocytes in *mIDH1* TME are not inhibitory and cannot be classified as PMN-MDSCs.

To further investigate the impact of *mIDH1* in the context of *ATRX* and *TP53* inactivating mutations on the phenotype and function of $CD45^{high}/CD11b^{+}/Ly6G^{+}$ cells, we performed an *ex-vivo* MDSC differentiation assay. We isolated BM cells from WT animals and co-cultured them

with *wtIDH1*, or *mIDH1* NS (2:1; BM cells: neurospheres; respectively) (Supplementary Fig. S7A). After seven days, we analyzed the frequency of granulocytes formed in each condition. Results showed that in the *mIDH1* NS co-culture, there was a higher frequency of $CD45^+/CD11b^+/Ly6G^+$ cells compared to those generated by co-cultures with *wtIDH1* NS (63.3 ± 2.1% vs. 85.3 ± 1.5% for wtIDH1 vs. mIDH1, respectively, $p < 0.05$ Supplementary Fig. S7B). Granulocytes in the *mIDH1* NS co-culture expressed lower levels of Arg1, PD-L1 and CD80 compared to those from *wtIDH1* NS co-culture, (Supplementary Fig. S7C-E). The immunosuppressive property of the *ex vivo*-generated $CD45^+/CD11b^+/Ly6G^+$ cells was investigated by *in vitro* suppression assays. Consistent with the *in vivo* experiments, $CD45^+/CD11b^+/Ly6G^+$ cells generated by co-culturing with *wtIDH1* NS (1:1) inhibit T-cell proliferation, whereas those generated from *mIDH1* NS were not inhibitory (Supplementary Fig. S7F, G). Collectively, these data validate that a tumor-derived factor is responsible for developing the non-immunosuppressive granulocytes in *mIDH1* glioma TME.

Single-cell transcriptomes analysis reveals neutrophils and pre-neutrophils are the major granulocytic lineages in *mIDH1* TME

Single-cell RNA-seq provides a powerful approach to dissect heterogeneous immune cells, by providing a transcriptome-wide profiling at the cellular level (53). We used this approach coupled with mass cytometry to compare the molecular differences of the TME-derived granulocytes on an individual cell basis (Fig. 3A). Two biological replicates of purified immune cells from TME of *mIDH1* mice (8,881 cells) and TME of *wtIDH1* mice (7,408 cells) were sequenced at an average depth of ~20,000 reads per cell. After filtering cells with low overall expression and/or high mitochondrial gene expression, we performed dimensionality reduction and unsupervised cell clustering using methods implemented in the Seurat software suite

independently for *mIDH1* and *wtIDH1* datasets to identify distinct cell populations (54). In *mIDH1*, we identified 14 distinct cell clusters expressing known markers of major immune cell types (Fig. 3B). Granulocytes formed the largest population and consisted of three clusters, which we refer to as C1, C2, and C3 (Fig. 3B; Supplementary Fig. S8B, D). C1 displayed high expression of PMN-MDSCs-related genes such as *Il1*b and *Arg2*, two major immunosuppressive factors previously used to define PMN-MDSCs in cancer models (55,56) (Fig. 3C; Supplementary Fig. S8B, D). C2 constitutes the largest granulocytic cluster, expressing high levels of *S100a8*, inflammatory cytokines involved in the recruitment of $CD8^+$ T-cells (*Ccl3*, and *Ccl4*), and cell cycle genes such as (*Cdc20*, and *G0s2*) (Fig. 3B; Supplementary Fig. S8B, D) (57). C3 expressed genes involved in neutrophil maturation (*Cebpe* and *Mpo*; Fig. 3C, Supplementary Fig. S8B, D). These results suggested that C1 represents the true PMN-MDSCs population within the TME of *mIDH1* tumors, whereas C2 and C3 correspond to pre-neutrophils and neutrophils, respectively. Interestingly, in *wtIDH1*, there was only one cluster of granulocytes (C7; Supplementary Fig. S8A, C). This cluster expressed PMN-MDSC related genes such as *Il1*b and *Arg2*, similar to cluster C1 in TME-*mIDH1* (Supplementary Fig. S8A, C). To confirm that granulocytes in *wtIDH1* tumor (C7) are similar to C1 granulocytes in the *mIDH1* tumor, we integrated the *wtIDH1* and *mIDH1* tumor-infiltrating immune cell datasets using functionality available in the Seurat3 package (58). Jointly clustering *wtIDH1* and *mIDH1* tumor-infiltrating immune cells showed that the granulocytic population formed three clusters corresponding to the C1, C2, and C3 clusters found in the TME of *mIDH1* tumors (Supplementary Fig. S9A). Interestingly, the majority of granulocytes from the TME of the *wtIDH1* tumor clustered with C1 cluster of granulocytes from *mIDH1* tumors (Supplementary Fig. S9B, C), suggesting that these cells share a common origin and have a similar function.

To further determine if C1 represents the true PMN-MDSCs within TME-*mIDH1*, we looked for a cell surface marker differentially expressed in C1 that would allow us to isolate cells from this cluster and assess their function. Among the top 50 differentially expressed genes in cluster C1, *CD274* (PD-L1) was the only cell surface marker that showed high expression in C1 compared to moderate and low expression in C2 and C3, respectively (Fig. 3C; Supplementary Table S4). Based on *CD274* expression, we reclassified the granulocytic populations of both TMEs. We found that there was one granulocyte population in the *wtIDH1* tumor and three distinct granulocytic populations in the *mIDH1* tumor, corresponding to C1, C2, and C3 (Fig. 3D). We FACS sorted each population based on the expression of PD-L1 and determined their inhibitory potential by performing a T-cell proliferation assay. Similar to the results obtained with granulocytes from *wtIDH1* TME (C7 cluster), co-culturing with C1 cells from *mIDH1* glioma results in ~40% inhibition of T-cell proliferation ($p < 0.05$), whereas C2 and C3 from *mIDH1* TME did not inhibit T-cell proliferation (Fig. 3E). These results validate the inhibitory potential of C1 as the true PMN-MDSCs cluster in *mIDH1* glioma TME.

CD16/32 is a specific marker that defines immunosuppressive PMN-MDSCs in mice

Our next goal was to identify a specific myeloid biomarker that would allow us to distinguish the inhibitory PMN-MDSCs from the non-inhibitory granulocytes. To identify a unique marker, we used a myeloid-specific antibody panel (Supplementary Table S1) that measures ~30 myeloid-specific parameters simultaneously and used it to perform CYTOF analysis of the granulocytic clusters found in *mIDH1* and *wtIDH1* glioma TME. We found that granulocytes from *wtIDH1* and the C1 cluster from *mIDH1* TME have similar expression of the majority of the myeloid biomarkers, with the FC-gamma receptor family (CD16/32) upregulated in all inhibitory PMN-MDSCs (Fig. 3F). CD16/32 is expressed on macrophages and granulocytes, and its expression is

correlated with maturation and function (59,60). To confirm the correlation between PMN-MDSCs phenotype and CD16/32 expression, we performed unsupervised clustering and dimensionality reduction which showed that granulocytes from *mIDH1* TME clustered differently than granulocytes from the *wtIDH1* TME (Fig. 3G, H). We observed high CD16/32 expression exclusively in all granulocytes from *wtIDH1* and only in C1 from *mIDH1* tumors (Fig. 3G, H). The majority of granulocytes from *wtIDH1* TME (~90%) express high levels of CD16/32, while only ~12% of granulocytes form *mIDH1* have high expression of CD16/32, the majority of which belongs to cluster C1 ($p < 0.05$, Fig. 3G-I). This suggests that CD16/32 is a unique myeloid marker for immune-suppressive PMN-MDSCs in mice.

PMN-MDSC gene signature is expressed in a higher proportion of tumor-infiltrating immune cells in human *wtIDH1* glioma

We then performed scRNA-seq of immune cells isolated from primary tumor samples of patients with *wtIDH1* and *mIDH1* glioma. We collected 18 tumor samples from a total of 7 patients (8 samples from *wtIDH1* tumors, 10 samples from *mIDH1* tumors). After performing immune cell purification and applying quality controls, a total of 9,765 cells from *wtIDH1* tumors and 17,452 from *mIDH1* tumors were analyzed. All patients' clinical data are listed in Supplementary Table S5. *wtIDH1* and *mIDH1* datasets were analyzed separately using Seurat to reproduce cell type labels (Fig. 4A-D). Myeloid clusters were the most abundant immune cells infiltrating both the *wtIDH1* and *mIDH1* human gliomas (Fig. 4A-D). In *wtIDH1* tumors, there was a total of 5 clusters of myeloid cells (Myeloid C1-C5) (Fig. 4A, C); all of which expressed the granulocyte colony-stimulating factor receptor, a receptor that labels cells from granulocytic lineages (*CSF3R*) (Supp Fig. S9D). Only one cluster (C4) expressed high microglial genes (*C1Qc*, *AIF1*) (Fig. 4A, C). In the *mIDH1* tumor, there were 4 clusters expressing *CSF3R* (Supp Fig. S9E).

Similar to the mouse data, the largest cluster (Myeloid-C1) expressed *CCL3*, and *CCL4* (Fig. 4B, D). Myeloid cluster C2 (Myeloid-C2) expressed antigen presentation-like genes (*HLA-A* and *HLA-DRA*), whereas Myeloid-C3 expressed granulocytes differentiation genes (*CSF3R*, *NEAT1*; Fig. 4D). C4 cluster express the microglia-like genes (*C1QB*, *C1QC*). We then investigated the expression of the PMN-MDSCs gene signature (*IL1β*, *S100a8*, *S100a9, ARG1, TGFβ1*) within each cluster in *wtIDH1* and *mIDH1* myeloid cells, separately (Fig. 5A, B). In *wtIDH1* tumors, Myeloid-C1 expressed high score for the PMN-MDSCs gene signature, whereas in the *mIDH1* group, myeloid-C5 expressed the highest score of PMN-MDSCs signature (Fig. 5A, B, Supp Fig. S9D, E). Nearly 17% of all immune cells in *wtIDH1* tumors were PMN-MDSCs, whereas in the *mIDH1* glioma TME, PMN-MDSCs were only 2.5% of the total immune cells (Fig. 5C). These results are consistent with our preclinical model data which showed that PMN-MDSCs are present at higher fraction in the TME of *wtIDH1* glioma than in the TME of *mIDH1* glioma.

G-CSF is the major cytokine that is epigenetically regulated in *mIDH1* glioma

Our data demonstrate that the majority of the granulocytes found in *mIDH1* TME are non-inhibitory granulocytes. We hypothesized that the change in granulocytes' phenotype and function is due to epigenetic reprogramming which affects cytokines' expression in the *mIDH1* glioma cells. Therefore, we profiled cytokines known to influence myeloid differentiation in conditioned media (CM) collected from *wtIDH1*, or *mIDH1* cultured mouse glioma neurospheres. The expression of the majority of the cytokines was downregulated in CM from the *mIDH1* group compared to CM from *wtIDH1* (Fig. 6A ; Supplementary Fig. S10). GM-CSF, CXCL1, CXCL10, IL-5, MIP-2, IL-6, and TNF-α were among the downregulated cytokines in *mIDH1* CM (Fig. 6A; Supplementary Fig. S10). However, G-CSF, RNATES (CCL5), IL-33, and SCF were the only cytokines that were upregulated in *mIDH1* CM (Supplementary Fig. S10). To

investigate if these cytokines were epigenetically regulated by *mIDH1*, we used a ChIP-seq dataset that we have recently reported (NCBI's Omnibus identifier: GSE99806), which was obtained using SB- generated neurospheres from *mIDH1* and *wtIDH1* glioma (61). Gene promoters enriched for H3K4me3 peaks are generally associated with transcriptional activation. Among the genes encoding the cytokines that were upregulated in CM from *mIDH1*, only *CSF3* showed a dramatic change in the peak enrichment for H3K4me3 mark around the promoter region (Fig. 6B). Moreover, quantitative ELISA confirmed that the level of G-CSF was increased in *mIDH1* compared to *wtIDH1* in both the mouse serum of tumor-bearing animals, as well as in CM from cultured mouse and human neurospheres (~5-fold, $P < 0.05$, Fig. 6C-E). In addition, TCGA-LGG analysis revealed that *CSF3* gene expression level was significantly upregulate in *mIDH1* glioma patients harboring *ATRX* and *TP53* mutation as compare to wtIDH1-LGG patients (Figure 6F). The increased level of G-CSF in *mIDH1* could explain the significant expansion of granulocytes in *mIDH1* tumor-bearing mice as well as the enrichment of the cytokine signaling pathway triggered by G-CSF receptor expressed on myeloid cells.

To uncover the source of G-CSF within gliomas, we performed scRNA-seq of whole tumors (~5000 cells) isolated from SB induced *mIDH1* glioma model. Results show that the majority of G-CSF was expressed by the major tumor cell clusters, which belong to stem-like cells and express genes such as *sox2*, *sox4*, *tcf4* (Fig. 6G, H). These results indicate that the undifferentiated tumor cells established by the developing *mIDH1* tumor express high levels of G-CSF, resulting in the phenotypic remodeling of the granulocytic population to non-immunosuppressive neutrophils.

G-CSF neutralization restores the immunosuppressive properties of $CD45^{high}/CD11b^{+}/Ly6G^{+}$ in *mIDH1* TME

If the $CD45^{high}/CD11b^{+}/Ly6G^{+}$ phenotype in *mIDH1* is dependent on G-CSF expression, blocking G-CSF should reverse their immune-permissive phenotype. We depleted G-CSF in the *mIDH1* tumor-bearing animals using the αG-CSF neutralizing antibody (Fig. 7A). Treatment with αG-CSF significantly reduced the serum levels of G-CSF in *mIDH1* tumor-bearing mice (~86% and ~92% decrease in day 14 dpi and 21 dpi, respectively; $p < 0.01$) and decreased the frequency of granulocytes in the TME, spleen, and BM (~40%, ~63%, and ~10%, respectively, $p < 0.05$ Fig. 7B, C). Interestingly, G-CSF neutralization remodeled the $CD45^{high}/CD11b^{+}/Ly6G^{+}$ compartment within the TME of *mIDH1* tumor-bearing animals to an inhibitory phenotype, which results in ~35% inhibition of T-cell proliferation (Fig. 7D). Moreover, G-CSF neutralization shortened the MS of *mIDH1* (but not the *wtIDH1*) tumor-bearing animals (MS = 30dpi vs. MS = 18dpi; $p <0.05$, in control vs. α-GCSF, respectively, Fig. 7E). This demonstrates that the non-inhibitory properties of granulocytes in the *mIDH1* glioma bearing mice is driven by high expression of G-CSF.

***CSF3* expression is associated with favorable outcome only in LGG patients harboring mIDH1**

Tumor-derived G-CSF has been shown to promote tumor progression and enhanced metastasis in several tumor types (62,63). To evaluate the effect of G-CSF in LGG patients, we turned to the TCGA data and analyzed the median survival (MS) of all tumor types available in the context of G-CSF (*CSF3*) expression (i.e. MS of patients expressing high vs low levels of *CSF3*). We used the UCSC-Xena browser to identify the differences in survival between patients with high or low levels of *CSF3* expression. Interestingly, we found that LGG was the only tumor type in which a significant difference existed between the MS of patients with high vs low *CSF3* expression (Supplementary Fig. S11). Moreover, when we stratified the astrocytoma patients according to

mIDH1 and *CSF3* expression, we found that enhanced median survival related to high *CSF3* expression was solely observed in patients with *mIDH1* tumors (Fig. 7F). There were no significant differences in MS between high vs low expression of other cytokines responsible for PMN-MDSCs development such as *CSF1*, *IL4, IL1β, TNFα*, *IL6* in *mIDH1* patients (data not shown). These results suggest the unique correlation between G-CSF expression in *mIDH1* LGG patients and its impact on patients' survival.

Glioma derived G-CSF induces the expansion of neutrophils and prolongs survival in mice

To uncover if G-CSF alone is sufficient to induce the expansion of non-immunosuppressive neutrophils, we dosed *wtIDH1* tumor-bearing mice with recombinant G-CSF (rG-CSF) (Fig. 7G). We used 2 μg/day of rG-CSF to achieve steady-state serum G-CSF concentrations comparable to levels observed in *mIDH1* tumor-bearing mice (Fig. 7B), and similar to reported doses (64,65). Compared to vehicle-treated animals, *wtIDH1* tumor-bearing animals treated with rG-CSF showed expansion of granulocytes in the TME (Fig. 7H). These granulocytes expressed lower levels of CD16/32 and PD-L1 compared to granulocytes from vehicle-treated control (Fig. 7I, J). Interestingly, rG-CSF administration remodeled granulocytes to non-inhibitory phenotype and significantly prolonged the MS of tumor-bearing animals (MS = 47dpi vs. MS = 24dpi; $p < 0.05$, in rGCSF vs. control, respectively, Fig. 7K, L). These results supported the hypothesis that G-CSF leads to the expansion of non-immune suppressive neutrophils and confirmed the association between the increased G-CSF secretion and enhanced prognosis in glioma. To validate the source of G-CSF, *wtIDH1* neurospheres were stably transduced with lentivirus encoding G-CSF (lenti-G-CSF) or with an empty lentivirus vector (lenti-vector). Sucessfully ransduced neurospheres were cultured *in vitro* for 14 days before they were used for implantation (Supp Fig S12). The enhanced G-CSF expression was confirmed by RT-qPCR as well as by ELISA in CM of cultured

neurospheres (Supplementary Fig. S12B, C). As expected, results showed that animals implanted with *wtIDH1*-lenti-G-CSF neurospheres had increased $CD45^{high}/CD11b^{+}/Ly6G^{+}$ in the tumor, spleen, and BM compared to mice implanted with *wtIDH1*-Lenti-vector neurospheres (Supplementary Fig. S12D-F). Collectively, this data demonstrates the effect of tumor-derived G-CSF on the phenotype and function of granulocytes in *mIDH1* glioma.

DISCUSSION

A salient feature of *mIDH1* gliomas is the epigenetic modifications of the tumor cells' transcriptome mediated by inhibition of the methylcytosine dioxygenase TET2, and αKG dependent histone demethylases. This results in a genome-wide hypermethylation phenotype and enhanced survival (66,67). Our data shows that *mIDH1* stem-like glioma cells, through epigenetic modification, exhibit enhanced G-CSF expression, a strong inducer of myeloid cell development, proliferation, and mobilization (68-70). Enhanced G-CSF expression triggers a shift in myelopoiesis favoring the production of non-immunosuppressive granulocytes that infiltrate the *mIDH1* glioma TME. Thus, our study provides evidence of a novel mechanism that contributes to the enhanced median survival in *mIDH1* glioma.

Gliomas are characterized by a profound immunosuppressive milieu that is responsible, at least in part, for hindering the efficacy of immunotherapies (22-24). Previous studies have shown that glioblastoma patients have elevated levels of circulating MDSCs; the majority of which (~82%) belong to PMN-MDSCs, and are associated with poor prognosis (29,71,72). We have recently shown that the PMN-MDSCs are the predominant immunosuppressive myeloid cells which upon depletion, significantly enhanced the efficacy of immunotherapy and prolonged median survival in *wtIDH1* glioma-bearing mice (25). These results highlight the immunosuppressive nature of *wtIDH1* glioma infiltrating PMN-MDSCs. The exact phenotypic, molecular, and functional

characterization of MDSCs in *mIDH1* glioma has not been revealed yet. An algorithm defining the true immunosuppressive MDSCs based on phenotypic, biochemical, and functional characteristics has been recently proposed (42). In our GEMM, although *mIDH1* tumor-bearing animals have a higher expansion of $CD45^{high}/CD11b^{+}/Ly6G^{+}$ cells, transcriptome and phenotypic analysis revealed that they lack the characteristic immune-suppressive gene signature of *bona fide* PMN-MDSCs (41,42).

The exact mechanisms that control the switch between the suppressive vs. non-suppressive phenotype of polymorphonuclear myeloid cells remain unknown. One proposed mechanism is that two signals orchestrate the development of immunosuppressive myeloid cells (73). The first signal is responsible for the recruitment and proliferation of myeloid cells, i.e., GM-CSF, SCF, or G-CSF (73,74). The second signal belongs to inflammatory cytokines such as IL-1β, IL-6, TGF-β, or IL-4 that trigger an inflammatory milieu responsible for the development of the immune-suppressive properties of the tumor-infiltrating myeloid cells (23,43,75). In line with this hypothesis, our data show that a cytokine belonging to the first signal (G-CSF) was epigenetically upregulated in *mIDH1* glioma bearing mice, whilst, all inflammatory cytokines responsible for the induction of MDSCs immunosuppression properties we tested were downregulated in *mIDH1* glioma. In addition, we found that G-CSF was expressed at a higher level in CM collected from cultured human glioma cells expressing *mIDH/ATRX and TP53* inactivating mutations, when compared to CM collected from *wtIDH1* glioma cells. Moreover, TCGA analysis revealed that the expression of *CSF3* was higher in astrocytoma patients harboring *mIDH1* along with inactivation mutations in *TP53*, *ATRX* as compared to *wtIDH1*. Overall, our data demonstrated that *mIDH1* gliomas exhibited enhanced expression of *CSF3*.

It has been recently shown that gliomas are highly heterogeneous tumors, having both inter-tumor and intra-tumor heterogeneity at the cellular and genomic levels (76-81). The mechanism by which genetic heterogeneity influences the tumor immune microenvironment remains elusive (82-85). The use of scRNA-seq technologies has now provided additional granularity which enables to chart subtypes of glioma immune cellular infiltrates within the glioma microenvironment. This technology enabled us to identify the developmental hierarchies within the glioma infiltrating myelopoietic cell clusters, uncovering novel drivers, and revealing the infiltrating-immune surveillance/evasion cell types relevant to tumors with specific genetic lesions (81,86-88). We thus performed scRNA-seq of the tumor-infiltrating $CD45^+$ immune cells harvested from our glioma GEMMs; both *wtIDH1* and *mIDH1*. Transcriptome profiling at the single cell level uncovered the global landscape of glioma-infiltrating myeloid cells and captured their heterogeneity. We discovered that the *mIDH1* glioma-infiltrating granulocytes are comprised of three distinct cell clusters; C1, C2, and C3. We performed differential gene expression analysis between the three clusters and identified that cluster C1 was enriched in immunosuppressive PMN-MDSCs signature marker genes such as *tgfb*, *Il1b*, and *Arg2*. Cluster C2 expressed *S100a8*, *ccl3*, *ccl4*, and cell cycle genes such as *Cdc20*, *G0s2* indicating proliferating neutrophils (pre-neutrophils). Whereas C3 expressed neutrophils maturation genes such as *cebpe*, and *mpo*. In contrast, in the *wtIDH1* glioma model, the tumor-infiltrating granulocytes are comprised of one single cluster expressing genes similar to granulocyte cluster, C1 in the *mIDH1* group.

Since a hallmark of MDSCs, is their inhibition of antigen specific $CD8^+$ T cell proliferation, we

next aimed to isolate the three newly identified granulocytic clusters encountered within the *mIDH1* TME for functional characterization. An ideal marker would be expressed on the cell surface, and have different expression levels between the three clusters. Interrogation of the differentially expressed genes between C1, C2, and C3 revealed that *CD274* (PD-L1) was expressed at a high level in PMN-MDSCs (cluster C1); compared to intermediate and low levels in the pre-neutrophils (cluster C2) and neutrophils (cluster C3), respectively (Fig. 3C). This allowed us to isolate each cluster and examine their T-cell inhibitory potential. Using this approach, we found that in the *mIDH1* group, cells in cluster C1 were suppressive whereas the cluster C2 and C3 were non-immunosuppressive, whereas in the *wtIDH1* group, granulocytes expressing PD-L1 formed one single cluster of cells (C7), which inhibited $CD8^+$ T-cell proliferation. Finally, we performed in-depth high-dimensional mass cytometry characterization and phenotypic analysis of the three granulocytic clusters found in the *mIDH1* TME. An advantage of this approach is that automated clustering is done on data reduced to two tSNE dimensions, which allows visual verification of cluster boundaries at the single-cell resolution. Combined clustering of granulocytes infiltrating the TME of *mIDH1* or *wtIDH1* GEMMs of glioma revealed that the majority of granulocytes from the *wtIDH1* tumor were allocated along with the C1 cluster of the *mIDH1* group. Cytof analysis also led to the identification of CD16/32 as a unique, and reproducible myeloid marker that can be used to distinguish immunosuppressive PMN-MDSCs from non-immunosuppressive granulocytes.

Consistent with results from our GEMMs of glioma, we found that the majority of immune cells infiltrating human gliomas expressing *mIDH1*, exhibit a characteristic myeloid cell's gene signatures; all of which express the early granulocytic receptor G-CSFR. Interestingly, the

largest myeloid cluster in the *mIDH1* glioma group expressed genes (*CCL3*, *CCL4*) similar to cluster C2 in our *mIDH1* GEMM of glioma. Moreover, using a unique PMN-MDSCs gene signature, our data elucidated that human *mIDH1* gliomas exhibit a lower frequency of tumor-infiltrating *bona fide* PMN-MDSCs when compared to the *wtIDH1* glioma patients. Therefore, the molecular and phenotypic features of *mIDH1* on tumor-infiltrating PMN-MDSCs is largely conserved between our mouse model and human samples.

G-CSF was upregulated in the CM of cultured human and mouse *mIDH1* NS. This increase was also significant in the serum from *mIDH1* tumor-bearing mice. We demonstrated that the increased G-CSF expression in *mIDH1* NS was due to epigenetic reprogramming of the tumor cells' transcriptome, in which the *CSF3* gene showed an enrichment in the deposition of the H3K4me3 mark around the promoter region. We demonstrated that in our *mIDH1* GEMM of glioma, tumor cells express a higher level of *Sox2* and are less differentiated (46); consistent with earlier reports indicated that $IDH1^{R132H}$ suppresses cellular differentiation (89,90). scRNA-seq revealed that glioma stem-like cells that express *Sox2* and *Sox4* are the major source of G-CSF expression in *mIDH1* tumors. Therefore, the enhanced production of G-CSF is due to the presence of a higher proportion of less differentiated tumor cells in *mIDH1* glioma. In line with this, studies showed that within the glioma niche, glioma stem-like cells are found to be co-enriched with myeloid infiltrating immune cells (91,92).

The impact of G-CSF on tumor biology is still a point of debate. Recombinant G-CSF (Filgastim®) is a commercially available product indicated for chemo-induced neutropenia to reverse myelosuppression in cancer patients and it has been shown to reduce inflammation and reverse cognitive impairment in patients with Alzheimer (93,94). In addition, increased G-CSF

secretion has been implicated in the recruitment and infiltration of immunosuppressive MDSCs in breast cancer (62) and cervical cancer (63). In contrast, in mice bearing MCA203 sarcomas, G-CSF induced $CD11b^{+}/Gr\text{-}1^{hi}$ cells that were non-suppressive (95). It has also been shown that the administration of G-CSF leads to the formation of non-immunosuppressive $CD45^{+}/CD11b^{+}/Gr\text{-}1^{+}$ *in vivo* (95) and *in vitro* (96). Our data in *mIDH1* glioma show that the increased production of G-CSF by *mIDH1* glioma stem-like cells caused the expansion of $CD45^{high}/CD11b^{+}/Ly6G^{+}$ cells that exhibit a non-immunosuppressive phenotype. We also showed that rG-CSF administration to mice harboring *wtIDH1* glioma reversed the immunosuppressive properties of the PMN-MDSCs, leading to increased median survival, similar to the median survival observed for *mIDH1* glioma bearing mice.

In summary, our data demonstrate that *mIDH1* tumor-derived G-CSF reprograms myelopoiesis in glioma, which promotes the production of non-immunosuppressive granulocytes, a feature that can be harnessed to enhance the immunotherapeutic efficacy in *mIDH1* glioma patients (Supplementary Fig S13).

MATERIALS AND METHODS

Study design: To study the impact of glioma *IDH1*^{R123H} on myeloid cell phenotype and function, we generated a genetically engineered animal model injecting SB plasmids encoding NRA G12V, *shATRX* and *shp53* with or without *IDH1*^{R132H} (*wtIDH1* and *mIDH1* respectively) into the lateral ventricle of neonatal mice (46,97,98). Sample size and any data inclusion/exclusion were defined individually for each experiment. We also used an animal model generated by intracranial implantation of glioma NS (*wtIDH1* and *mIDH1*) derived from our genetically engineered animal model (46,99). Additionally, we used an alternative model (PDGFB/shP53/shATRX/Ink4a/Arf$^{-/-}$ *wtIDH1*-NS or *mIDH1*-NS) that does not encode RAS-activating mutations. We performed pan characterization of all immune cells by flow cytometry and mass cytometry and identified each immune cell population using unique biomarkers. Detailed information regarding the source of antibodies and immune cells' gating are listed in supplementary tables S1, S2, and S3. We also performed scRNA-seq to define the PMN-MDSCs cell population in both mouse and human glioma tissue derived from patients harboring *IDH1*^{R132H} or *wtIDH1*. We validated PMN-MDSCs by functional analysis of T-cell's inhibitory characteristics. The numbers of replicates are reported in the figure legends. All scRNA-seq data were deposited in public databases as is indicated in the respective sections. Materials and Methods are described in detail in the Supplementary Materials section.

Statistical analysis: Sample sizes were selected based on preliminary data from pilot experiments and previously published results in the literature and our laboratory. Unpaired Student t-test or one-way analysis of variance (ANOVA), followed by Tukey's multiple comparisons post-test were utilized for comparing experimental groups with controls from flow

cytometry analysis, cytokine analysis, mass cytometry analysis, and T-cell functional assays. RNA-seq, data were processed using the Tuxedo Suite, and differentially expressed genes were considered when FDR $\leq$ 0.05, and fold change $\geq \pm$ 1.5. All single-cell sequencing data were processed by Cell Ranger Pipeline version 3.1.0. Filtered digital gene expression matrix files (DGE) matrices containing the number of unique molecular identifiers (UMI) counts per gene per cell were analyzed using the Seurat R package version 3.1.4. Statistically significant principal components were determined using the jackstraw function (54,58). All quantitative data are presented as the Means ± SEM from at least three independent samples. ANOVA and two-sample t-tests were used to compare continuous outcomes between groups. Survival curves were analyzed using the Kaplan-Meier method and compared using Mantel-Cox tests; the effect size is expressed as MS. Differences were considered significant if $P < 0.05$. All analyses were conducted using GraphPad Prism software (version 8.00), or R (version 3.4). The statistical tests used are indicated in each figure legend.

Figure Legends

Figure 1. *mIDH1* glioma model has the highest expansion of granulocytic myeloid cells ($CD45^{high}/CD11b^{+}/Ly6G^{+}$). (A) Experimental design of sleeping beauty (SB)-based tumor development, immune cells isolation and CyTOF analysis. **(B)** Schematic representation illustrating the two groups of neurospheres generated with different genetic lesions using the SB model. **(C, D)** SPADE analysis of mass cytometry (CyTOF) data represents immune cell composition within the TME of SB induced *wtIDH1* **(C)** or *mIDH1* **(D)** tumors. Insets are viSNE visualizations of high-dimensional mass cytometry data; color intensity represents the Gr-1 expression level. **(E, F)** After neurospheres implantation, myeloid-derived suppressor cells were identified as $CD45^{high}/CD11b^{+}/Gr\text{-}1^{+}$ cells within the TME at mid-stage of tumor implantation and at symptomatic stage. The percentage of $CD45^{high}/CD11b^{+}/Gr\text{-}1^{+}$ cells was the highest in *mIDH1* tumors. **(G)** Phenotypic characterization of $CD45^{high}/CD11b^{+}/Gr\text{-}1^{+}$ population into granulocytic or monocytic based on the expression of Ly6G or Ly6C at symptomatic stage. The majority of the $CD45^{high}/CD11b^{+}/Gr\text{-}1^{+}$ in the *mIDH1* glioma TME are $CD45^{high}/CD11b^{+}/Ly6G^{+}$ (granulocytic) cells. **(H, I)** CyTOF analysis of $CD45^{high}/CD11b^{+}/Gr\text{-}1^{+}$ cells in blood from mice with no tumor (normal), and SB induced *wtIDH1* or *mIDH1* glioma. **(J)** Phenotypic characterization of circulating $CD45^{high}/CD11b^{+}/Gr\text{-}1^{+}$ cells according to expression of Ly6C or Ly6G. **(K, L)** CyTOF analysis of $CD45^{high}/CD11b^{+}/Gr\text{-}1^{+}$ cells from the spleens of mice with no tumor, and SB induced *wtIDH1* or *mIDH1* glioma. **(M)** Phenotypic characterization of splenic $CD45^{high}/CD11b^{+}/Gr\text{-}1^{+}$ cells according to expression of Ly6C or Ly6G. N: normal, *$P<0.05$, ** $P<0.01$, *** $P<0.005$, **** $P<0.0001$. Analysis of variance (ANOVA).

Figure 2. Phenotypic, molecular and functional characterization of myeloid cells lineages in *mIDH1* glioma. (A) Representative flow cytometry plots showing the percentage of hematopoietic stem cells (HSCs) ($Lin^-/c\text{-}Kit^+/Sca\text{-}1^+$) and myeloid progenitors (MP) ($Lin^-/c\text{-}Kit^-/Sca\text{-}1^+$) in BM from normal mice, and mice implanted with *wtIDH1* or *mIDH1* neurospheres. **(B, C)** Quantification of the number and frequency of **(B)** HSCs and **(C)** MPs from the BM of naïve mouse, and tumor-bearing animals at symptomatic stage. Mice with *mIDH1* tumor have a lower number and frequency of HSCs but higher frequency of MPs. Flow cytometry analysis of the frequency of **(D)** Granulocyte-macrophage progenitors (GMPs) ($Lin^-/IL\text{-}7R\alpha^-/c\text{-}kit^+/Sca\text{-}1^-/CD34^+/FcyRII/III^{high}$) and **(E)** Common lymphocyte progenitors (CLPs) ($c\text{-}kit^{low}/Sca\text{-}1^{low}/Lin^-/IL\text{-}7R\alpha^+$) in the BM from naïve and *wtIDH1* or *mIDH1* tumor-bearing animals. *mIDH1* tumor had a higher frequency of GMPs but not CLPs in the BM compared to the *wtIDH1* group. **(F)** Schematic diagram representing the shift in hematopoiesis towards granulocytic-lineage development in the bone marrow of *mIDH1* tumor-bearing mice. Thick arrows represent predominant developmental pathways in *mIDH1* tumor bearing mice. **(G)** Heat map showing the normalized expression of genes related to PMN-MDSCs immunosuppressive signature in granulocytes from *wtIDH1* or *mIDH1* TME. $CD45^{high}/CD11b^+/Ly6G^+$ cells from *mIDH1* TME have lower expression of immune suppressive markers. **(H-M)** Flow cytometry analysis of immunosuppressive/co-stimulatory markers in the $CD45^{high}/CD11b^+/Ly6G^+$ population within TME of *wtIDH1* (black) or *mIDH1* (blue) TME. Granulocytes from *mIDH1* tumors have lower expression of all tested markers. **(N)** Schematic of the *in vitro* T-cell proliferation assay to analyze immune suppressive properties of $CD45^{high}/CD11b^+/Ly6G^+$ cells. $CD45^{high}/CD11b^+/Ly6G^+$ cells were co-cultured with CFSE-labeled splenocytes from *Rag2/OT-1* transgenic mouse. Cultures were stimulated with 100 nM SIINFEKL peptide for 4 days, after

which proliferation was analyzed by flow cytometry **(O)** Representative flow plots showing CFSE staining of unstimulated splenocytes (T only), splenocytes undergoing rapid proliferation in response to SIINFEKL (T+ SIIN), and the effect of SIINFEKL-induced T-cell proliferation in the presence of $CD45^{high}/CD11b^{+}/Ly6G^{+}$ cells from the TME of *wtIDH1* or *mIDH1* tumors. **(P)** Flow analysis of the inhibitory potential of $CD45^{high}/CD11b^{+}/Ly6G^{+}$ cells from TME of *wtIDH1* or *mIDH1* tumor. $CD45^{high}/CD11b^{+}/Ly6G^{+}$ cells from TME-*wtIDH1* tumors are immunosuppressive, whereas $CD45^{high}/CD11b^{+}/Ly6G^{+}$ cells from TME of *mIDH1* tumors did not suppress T-cell proliferation. $^{*}P<0.05$, $^{**}P<0.01$, $^{***}P<0.005$, One-way ANOVA.

Figure 3. Neutrophils and pre-neutrophils are the major granulocytes population in *mIDH1* tumors. (A) Schematic overview of single-cell-seq and mass cytometry (CyTOF) analysis of immune cells purified from TME of SB *wtIDH1* and *mIDH1* tumor-bearing animals. **(B)** Combined Seurat analysis of immune cells from *mIDH1* shown in UMAP projection results in various distinct clusters of TME immune cells. Granulocytes were identified in three clusters in the *mIDH1* TME (C1, C2, C3) (N=2) **(C)** Heatmap of differentially expressed immunosuppressive and neutrophil-related genes between the three granulocytic clusters of *mIDH1* TME group. C1 has a high expression of immune suppressive genes, whereas C2 and C3 have lower expression. C3 has a high expression of characteristic neutrophil genes such as *MPO*, *CEBPE*, and *ETS1*. Arrow reperesent *CD274* expression. **(D)** Mass cytometry analysis of granulocytes from TME of *wtIDH1* (Top panel) or *mIDH1* (bottom panel) tumors. Based on PD-L1 expression, granulocytes from *wtIDH1* tumor clustered in one cell population whereas in *mIDH1*, PD-L1 (CD274) expression, separated the granulocytes into three clusters corresponding to clusters C1, C2, and C3 of the scRNA-seq data. **(E)** T-cell proliferation analysis to assess the

inhibitory potential of myeloid cells cluster (C7) from *wtIDH1* tumors or C1, C2, and C3 myeloid cells clusters isolated from *mIDH1* tumors. C7 myeloid cells cluster from the TME of *wtIDH1* tumors and C1 myeloid cells cluster from *mIDH1* tumor TME are immunosuppressive, whereas C2 and C3 from *mIDH1* TME did not suppress T-cell proliferation. **(F)** Heat map representing CyTOF normalized expression level of myeloid biomarkers within granulocytes from the TME of *wtIDH1* tumors or C1, C2, and C3 clusters from the TME of *mIDH1*. CD16/32 (arrow) is reproducibly expressed in immunosuppressive PMN-MDSCs. **(G, H)** Unsupervised clustering and viSNE visualization of granulocytes from *wtIDH1* **(G)** or *mIDH1* **(H)** tumors using biomarker shown in **(F)**. Circumscribed area indicates PMN-MDSCs from *wtIDH1*, which expressed a high level of CD16/32. **(I)** Proportion of PMN-MDSCs (% of total granulocytes) from TME of *wtIDH1* or *mIDH1* TME. The majority of granulocytes from *wtIDH1* (~90%) correspond to PMN-MDSCs, whereas only 12-16% of granulocytes from *mIDH1* belong to PMN-MDSCs. *$P<0.05$, **$P<0.01$. Student's *t*-test

Figure 4. Single-cell RNA-seq analysis of primary human gliomas expressing *wtIDH1* or *mIDH1*. (A, B) Seurat analysis of immune cells from **(A)** *wtIDH1* or **(B)** *mIDH1* primary tumor samples shown in UMAP projection results in various distinct clusters. In total, there were five myeloid clusters in *wtIDH1* tumors. The PMN-MDSCs cluster formed the major cell population in *wtIDH1* but not in the *mIDH1* group. **(C)** Heat map showing the differentially expressed genes in each cluster of *wtIDH1* tumor samples. **(D)** Heat map showing the differentially expressed genes in each cluster of the *mIDH1* tumor samples.

Figure 5. mIDH1 gliomas exhibit lower frequencies of tumor infiltrating PMN-MDSCs. (A) Bar plots showing the relative PMN-MDSCs score in each cluster of primary human samples from **(A)** *wtIDH1* or **(B)** *mIDH1* tumors**.** Cluster C1 in the *wtIDH1* and cluster C5 in the *mIDH1* exhibit the highest expression of PMN-MDSC gene signature. **(F)** Quantification of the percentage of tumor-infiltrating PMN-MDSCs/total immune cells calculated from scRNA-seq data in *wtIDH1* and *mIDH1* human gliomas.

Figure 6. G-CSF is the major epigenetically regulated cytokine expressed by glioma stem-like cells. (A) Cytokine array analysis performed on conditioned media from *wtIDH1*, or *mIDH1* neurospheres. Bar graphs show the pixel intensity of each spot. Dash boxes indicate the candidate cytokines that may contribute to the myeloid phenotypic change. **(B)** H3K4me3 occupancy at specific genomic regions of *CSF3* gene. Reads were visualized using IGV, and differential peaks (FDR < 0.05) in *mIDH1* neurospheres are represented in red compared to *wtIDH1* neurospheres in blue. **(C-E)** Quantitative ELISA of the G-CSF level in mouse serum of tumor-bearing animals **(C),** conditioned media from mouse neurospheres cultures **(D),** and conditioned media from human neurospheres cultures expressing *wtIDH1* or *mIDH1* **(E). (F)** Analysis of *CSF3* (G-CSF) gene expression for *mIDH1* glioma patients harboring *TP53* and *ATRX* mutation (n=99), and *wtIDH1* (n=82). RNA-seq data was obtained from TCGA (Xena browser platform). Graph displays the $\log_2$ expression value of *CSF3* mRNA. **(G, H)** Combined Seurat analysis shown in tSNE projection of whole tumor cells from *mIDH1* GEMM of glioma results in various distinct clusters of tumor cells**.** The expression of *CSF3* was analyzed between the clusters. Stem-like cells were the major clusters that have the highest *CSF3* expression. (N=2) * *P<0.05,* ** *P<0.01,* *** *P<0.005*

Figure 7. G-CSF neutralization restores the immunosuppressive potential of CD45^{high}/CD11b^{+}/Ly6G^{+} cells in *mIDH1* glioma and shortened the MS of mDH1 tumor-bearing mice. (A) Schematic showing experimental design of G-CSF neutralization in *wtIDH1* and *mIDH1* tumor-bearing mice. **(B)** Quantitative ELISA analysis of G-CSF level from serum of *mIDH1* glioma bearing mice treated with either isotype (red) or αG-CSF (blue). **(C)** Flow analysis of CD45^{high}/CD11b^{+}/Ly6G^{+} cells from tumor, spleen, and BM of tumor-bearing mice treated with either isotype or αG-CSF. G-CSF neutralization decreased the percentage of CD45^{high}/CD11b^{+}/Ly6G^{+} cells in *mIDH1* tumor-bearing mice but not in the *wtIDH1* tumor. **(D)** T-cell proliferation assay demonstrated that G-CSF neutralization restored the immune suppressive potential of CD45^{high}/CD11b^{+}/Ly6G^{+} in *mIDH1* tumor-bearing mice. **(E)** Kaplan-Meier survival analysis of mice implanted with either *wtIDH1* or *mIDH1* neurospheres treated with isotype or αG-CSF. Neutralization of G-CSF decreased the MS of *mIDH1* tumor-bearing mice, but it did not affect the MS of *wtIDH1*tumor bearing mice. **(F)** Kaplan-Meier survival analysis of TCGA-LGG astrocytoma *wtIDH1* or *mIDH1* patients with high vs low level of *CSF3* expression. **(G)** Experimental design of recombinant G-CSF (rG-CSF) or vehicle administration in *wtIDH1* tumor-bearing animals. **(H)** Flow analysis of granulocytes from the tumor of *wtIDH1* tumor-bearing animals treated with vehicle or rG-CSF. **(I, J)** Flow analysis of CD16/32 and PD-L1 expression on granulocytes isolated from *wtIDH1* tumor-bearing animals treated with vehicle (blue) or rG-CSF (Red). **(K)** Flow analysis of the inhibitory potential of CD45^{high}/CD11b^{+}/Ly6G^{+} cells isolated from TME of *wtIDH1* tumor-bearing mice treated with vehicle (blue) or with rG-CSF (red). CD45^{high}/CD11b^{+}/Ly6G^{+} cells from TME of *wtIDH1*+ veh tumors are immunosuppressive, whereas CD45^{high}/CD11b^{+}/Ly6G^{+} cells from TME of *wtIDH1*+rG-CSF tumors did not suppress T-cell proliferation. **(L)** Kaplan-Meier survival analysis of animals

bearing *wtIDH1* tumors treated with either isotype (blue) or rG-CSF (red). rG-CSF treatment increased the MS of *wtIDH1* tumor-bearing animals (*wtIDH1*+ iso MS=24 dpi, *wtIDH1*+rGCSF MS=47 dpi). * $P<0.05$, ** $P<0.01$, *** $P<0.005$. ANOVA

1. Ceccarelli M, Barthel FP, Malta TM, Sabedot TS, Salama SR, Murray BA*, et al.* Molecular Profiling Reveals Biologically Discrete Subsets and Pathways of Progression in Diffuse Glioma. Cell **2016**;164(3):550-63 doi 10.1016/j.cell.2015.12.028.
2. Yan H, Parsons DW, Jin G, McLendon R, Rasheed BA, Yuan W*, et al.* IDH1 and IDH2 Mutations in Gliomas. New England Journal of Medicine **2009**;360(8):765-73 doi 10.1056/NEJMoa0808710.
3. Figueroa ME, Abdel-Wahab O, Lu C, Ward PS, Patel J, Shih A*, et al.* Leukemic IDH1 and IDH2 Mutations Result in a Hypermethylation Phenotype, Disrupt TET2 Function, and Impair Hematopoietic Differentiation. Cancer cell **2010**;18(6):553-67 doi 10.1016/j.ccr.2010.11.015.
4. Turcan S, Rohle D, Goenka A, Walsh LA, Fang F, Yilmaz E*, et al.* IDH1 mutation is sufficient to establish the glioma hypermethylator phenotype. Nature **2012**;483(7390):479-83 doi 10.1038/nature10866.
5. Lu C, Ward PS, Kapoor GS, Rohle D, Turcan S, Abdel-Wahab O*, et al.* IDH mutation impairs histone demethylation and results in a block to cell differentiation. Nature **2012**;483(7390):474-8 doi 10.1038/nature10860.
6. Turcan S, Rohle D, Goenka A, Walsh LA, Fang F, Yilmaz E*, et al.* IDH1 mutation is sufficient to establish the glioma hypermethylator phenotype. Nature **2012**;483(7390):479-83 doi 10.1038/nature10866.
7. Ward PS, Patel J, Wise DR, Abdel-Wahab O, Bennett BD, Coller HA*, et al.* The common feature of leukemia-associated IDH1 and IDH2 mutations is a neomorphic enzyme activity converting alpha-ketoglutarate to 2-hydroxyglutarate. Cancer cell **2010**;17(3):225-34 doi 10.1016/j.ccr.2010.01.020.
8. Figueroa ME, Abdel-Wahab O, Lu C, Ward PS, Patel J, Shih A*, et al.* Leukemic IDH1 and IDH2 mutations result in a hypermethylation phenotype, disrupt TET2 function, and impair hematopoietic differentiation. Cancer cell **2010**;18(6):553-67 doi 10.1016/j.ccr.2010.11.015.
9. Izquierdo-Garcia JL, Viswanath P, Eriksson P, Chaumeil MM, Pieper RO, Phillips JJ*, et al.* Metabolic reprogramming in mutant IDH1 glioma cells. PloS one **2015**;10(2):e0118781 doi 10.1371/journal.pone.0118781.
10. Karpel-Massler G, Ishida CT, Bianchetti E, Zhang Y, Shu C, Tsujiuchi T*, et al.* Induction of synthetic lethality in IDH1-mutated gliomas through inhibition of Bcl-xL. Nature communications **2017**;8(1):1067 doi 10.1038/s41467-017-00984-9.
11. Ronnebaum SM, Ilkayeva O, Burgess SC, Joseph JW, Lu D, Stevens RD*, et al.* A pyruvate cycling pathway involving cytosolic NADP-dependent isocitrate dehydrogenase regulates glucose-stimulated insulin secretion. The Journal of biological chemistry **2006**;281(41):30593-602 doi 10.1074/jbc.M511908200.
12. Seltzer MJ, Bennett BD, Joshi AD, Gao P, Thomas AG, Ferraris DV*, et al.* Inhibition of glutaminase preferentially slows growth of glioma cells with mutant IDH1. Cancer research **2010**;70(22):8981-7 doi 10.1158/0008-5472.CAN-10-1666.
13. Dang L, White DW, Gross S, Bennett BD, Bittinger MA, Driggers EM*, et al.* Cancer-associated IDH1 mutations produce 2-hydroxyglutarate. Nature **2009**;462(7274):739-44 doi 10.1038/nature08617.
14. Reitman ZJ, Duncan CG, Poteet E, Winters A, Yan LJ, Gooden DM*, et al.* Cancer-associated isocitrate dehydrogenase 1 (IDH1) R132H mutation and d-2-hydroxyglutarate stimulate glutamine metabolism under hypoxia. The Journal of biological chemistry **2014**;289(34):23318-28 doi 10.1074/jbc.M114.575183.
15. Yalaza C, Ak H, Cagli MS, Ozgiray E, Atay S, Aydin HH. R132H Mutation in IDH1 Gene is Associated with Increased Tumor HIF1-Alpha and Serum VEGF Levels in Primary Glioblastoma Multiforme. Ann Clin Lab Sci **2017**;47(3):362-4.

16. Seok J, Yoon SH, Lee SH, Jung JH, Lee YM. The oncometabolite d2hydroxyglutarate induces angiogenic activity through the vascular endothelial growth factor receptor 2 signaling pathway. Int J Oncol **2019**;54(2):753-63 doi 10.3892/ijo.2018.4649.
17. Zhao S, Lin Y, Xu W, Jiang W, Zha Z, Wang P*, et al.* Glioma-derived mutations in IDH1 dominantly inhibit IDH1 catalytic activity and induce HIF-1alpha. Science (New York, NY) **2009**;324(5924):261-5 doi 10.1126/science.1170944.
18. Xu W, Yang H, Liu Y, Yang Y, Wang P, Kim SH*, et al.* Oncometabolite 2-hydroxyglutarate is a competitive inhibitor of alpha-ketoglutarate-dependent dioxygenases. Cancer cell **2011**;19(1):17-30 doi 10.1016/j.ccr.2010.12.014.
19. Núñez FJ, Mendez FM, Kadiyala P, Alghamri MS, Savelieff MG, Garcia-Fabiani MB*, et al.* IDH1-R132H acts as a tumor suppressor in glioma via epigenetic up-regulation of the DNA damage response. Science translational medicine **2019**;11(479):eaaq1427 doi 10.1126/scitranslmed.aaq1427.
20. Sampson JH, Gunn MD, Fecci PE, Ashley DM. Brain immunology and immunotherapy in brain tumours. Nature Reviews Cancer **2020**;20(1):12-25 doi 10.1038/s41568-019-0224-7.
21. Reardon DA, Brandes AA, Omuro A, Mulholland P, Lim M, Wick A*, et al.* Effect of Nivolumab vs Bevacizumab in Patients With Recurrent Glioblastoma: The CheckMate 143 Phase 3 Randomized Clinical Trial. JAMA oncology **2020** doi 10.1001/jamaoncol.2020.1024.
22. Garcia-Fabiani MB, Ventosa M, Comba A, Candolfi M, Nicola Candia AJ, Alghamri MS*, et al.* Immunotherapy for gliomas: shedding light on progress in preclinical and clinical development. Expert Opin Investig Drugs **2020**:1-26 doi 10.1080/13543784.2020.1768528.
23. Kamran N, Alghamri MS, Nunez FJ, Shah D, Asad AS, Candolfi M*, et al.* Current state and future prospects of immunotherapy for glioma. Immunotherapy **2018**;10(4):317-39 doi 10.2217/imt-2017-0122.
24. Altshuler DB, Kadiyala P, Nuñez FJ, Nuñez FM, Carney S, Alghamri MS*, et al.* Prospects of biological and synthetic pharmacotherapies for glioblastoma. Expert Opinion on Biological Therapy **2020**;20(3):305-17 doi 10.1080/14712598.2020.1713085.
25. Kamran N, Kadiyala P, Saxena M, Candolfi M, Li Y, Moreno-Ayala MA*, et al.* Immunosuppressive Myeloid Cells' Blockade in the Glioma Microenvironment Enhances the Efficacy of Immune-Stimulatory Gene Therapy. Molecular therapy : the journal of the American Society of Gene Therapy **2017**;25(1):232-48 doi 10.1016/j.ymthe.2016.10.003.
26. von Roemeling CA, Wang Y, Qie Y, Yuan H, Zhao H, Liu X*, et al.* Therapeutic modulation of phagocytosis in glioblastoma can activate both innate and adaptive antitumour immunity. Nature communications **2020**;11(1):1508 doi 10.1038/s41467-020-15129-8.
27. Chang AL, Miska J, Wainwright DA, Dey M, Rivetta CV, Yu D*, et al.* CCL2 Produced by the Glioma Microenvironment Is Essential for the Recruitment of Regulatory T Cells and Myeloid-Derived Suppressor Cells. Cancer research **2016**;76(19):5671-82 doi 10.1158/0008-5472.CAN-16-0144.
28. Raychaudhuri B, Rayman P, Huang P, Grabowski M, Hambardzumyan D, Finke JH*, et al.* Myeloid derived suppressor cell infiltration of murine and human gliomas is associated with reduction of tumor infiltrating lymphocytes. Journal of neuro-oncology **2015**;122(2):293-301 doi 10.1007/s11060-015-1720-6.
29. Dubinski D, Wölfer J, Hasselblatt M, Schneider-Hohendorf T, Bogdahn U, Stummer W*, et al.* CD4+ T effector memory cell dysfunction is associated with the accumulation of granulocytic myeloid-derived suppressor cells in glioblastoma patients. Neuro-oncology **2015**;18(6):807-18 doi 10.1093/neuonc/nov280.
30. Gielen PR, Schulte BM, Kers-Rebel ED, Verrijp K, Petersen-Baltussen HMJM, ter Laan M*, et al.* Increase in Both CD14-Positive and CD15-Positive Myeloid-Derived Suppressor Cell Subpopulations in the Blood of Patients With Glioma But Predominance of CD15-Positive

Myeloid-Derived Suppressor Cells in Glioma Tissue. Journal of Neuropathology & Experimental Neurology **2015**;74(5):390-400 doi 10.1097/NEN.0000000000000183.

31. Amankulor NM, Kim Y, Arora S, Kargl J, Szulzewsky F, Hanke M*, et al.* Mutant IDH1 regulates the tumor-associated immune system in gliomas. Genes & development **2017**;31(8):774-86 doi 10.1101/gad.294991.116.
32. Mu L, Long Y, Yang C, Jin L, Tao H, Ge H*, et al.* The IDH1 Mutation-Induced Oncometabolite, 2-Hydroxyglutarate, May Affect DNA Methylation and Expression of PD-L1 in Gliomas. Frontiers in Molecular Neuroscience **2018**;11(82) doi 10.3389/fnmol.2018.00082.
33. Berghoff AS, Kiesel B, Widhalm G, Wilhelm D, Rajky O, Kurscheid S*, et al.* Correlation of immune phenotype with IDH mutation in diffuse glioma. Neuro-oncology **2017**;19(11):1460-8 doi 10.1093/neuonc/nox054.
34. Cimino PJ, Zager M, McFerrin L, Wirsching H-G, Bolouri H, Hentschel B*, et al.* Multidimensional scaling of diffuse gliomas: application to the 2016 World Health Organization classification system with prognostically relevant molecular subtype discovery. Acta neuropathologica communications **2017**;5(1):39- doi 10.1186/s40478-017-0443-7.
35. Auezova R, Ivanova N, Akshulakov S, Zhetpisbaev B, Kozhakhmetova A, Ryskeldiyev N*, et al.* Isocitrate dehydrogenase 1 mutation is associated with reduced levels of inflammation in glioma patients. Cancer Manag Res **2019**;11:3227-36 doi 10.2147/CMAR.S195754.
36. Chen Z, Feng X, Herting CJ, Garcia VA, Nie K, Pong WW*, et al.* Cellular and Molecular Identity of Tumor-Associated Macrophages in Glioblastoma. Cancer research **2017**;77(9):2266 doi 10.1158/0008-5472.CAN-16-2310.
37. Chen Z, Hambardzumyan D. Immune Microenvironment in Glioblastoma Subtypes. Frontiers in Immunology **2018**;9(1004) doi 10.3389/fimmu.2018.01004.
38. Louis DN, Perry A, Reifenberger G, von Deimling A, Figarella-Branger D, Cavenee WK*, et al.* The 2016 World Health Organization Classification of Tumors of the Central Nervous System: a summary. Acta neuropathologica **2016**;131(6):803-20 doi 10.1007/s00401-016-1545-1.
39. Yvan-Charvet L, Ng LG. Granulopoiesis and Neutrophil Homeostasis: A Metabolic, Daily Balancing Act. Trends in immunology **2019**;40(7):598-612 doi 10.1016/j.it.2019.05.004.
40. Németh T, Sperandio M, Mócsai A. Neutrophils as emerging therapeutic targets. Nature Reviews Drug Discovery **2020**;19(4):253-75 doi 10.1038/s41573-019-0054-z.
41. Kumar V, Patel S, Tcyganov E, Gabrilovich DI. The Nature of Myeloid-Derived Suppressor Cells in the Tumor Microenvironment. Trends in immunology **2016**;37(3):208-20 doi 10.1016/j.it.2016.01.004.
42. Bronte V, Brandau S, Chen SH, Colombo MP, Frey AB, Greten TF*, et al.* Recommendations for myeloid-derived suppressor cell nomenclature and characterization standards. Nature communications **2016**;7:12150 doi 10.1038/ncomms12150.
43. Gabrilovich DI, Nagaraj S. Myeloid-derived suppressor cells as regulators of the immune system. Nature reviews Immunology **2009**;9(3):162-74 doi 10.1038/nri2506.
44. Bronte V, Brandau S, Chen S-H, Colombo MP, Frey AB, Greten TF*, et al.* Recommendations for myeloid-derived suppressor cell nomenclature and characterization standards. Nat Commun **2016**;7:12150- doi 10.1038/ncomms12150.
45. Veglia F, Perego M, Gabrilovich D. Myeloid-derived suppressor cells coming of age. Nature Immunology **2018**;19(2):108-19 doi 10.1038/s41590-017-0022-x.
46. Nunez FJ, Mendez FM, Kadiyala P, Alghamri MS, Savelieff MG, Garcia-Fabiani MB*, et al.* IDH1-R132H acts as a tumor suppressor in glioma via epigenetic up-regulation of the DNA damage response. Science translational medicine **2019**;11(479) doi 10.1126/scitranslmed.aaq1427.

47. Koschmann C, Calinescu AA, Nunez FJ, Mackay A, Fazal-Salom J, Thomas D*, et al.* ATRX loss promotes tumor growth and impairs nonhomologous end joining DNA repair in glioma. Science translational medicine **2016**;8(328):328ra28 doi 10.1126/scitranslmed.aac8228.
48. Calinescu AA, Nunez FJ, Koschmann C, Kolb BL, Lowenstein PR, Castro MG. Transposon mediated integration of plasmid DNA into the subventricular zone of neonatal mice to generate novel models of glioblastoma. Journal of visualized experiments : JoVE **2015**(96) doi 10.3791/52443.
49. Amir el AD, Davis KL, Tadmor MD, Simonds EF, Levine JH, Bendall SC*, et al.* viSNE enables visualization of high dimensional single-cell data and reveals phenotypic heterogeneity of leukemia. Nature biotechnology **2013**;31(6):545-52 doi 10.1038/nbt.2594.
50. Hambardzumyan D, Amankulor NM, Helmy KY, Becher OJ, Holland EC. Modeling Adult Gliomas Using RCAS/t-va Technology. Translational oncology **2009**;2(2):89-95 doi 10.1593/tlo.09100.
51. Subramanian A, Tamayo P, Mootha VK, Mukherjee S, Ebert BL, Gillette MA*, et al.* Gene set enrichment analysis: a knowledge-based approach for interpreting genome-wide expression profiles. Proceedings of the National Academy of Sciences of the United States of America **2005**;102(43):15545-50 doi 10.1073/pnas.0506580102.
52. Alghamri MS, Kamran N, Kadiyala P, Lowenstein PR, Castro MG. Chapter Twelve - Functional assay to assess T-cell inhibitory properties of myeloid derived suppressor cells (MDSCs) isolated from the tumor microenvironment of murine glioma models. In: Galluzzi L, Rudqvist N-P, editors. Methods in enzymology. Volume 632: Academic Press; 2020. p 215-28.
53. Tanay A, Regev A. Scaling single-cell genomics from phenomenology to mechanism. Nature **2017**;541(7637):331-8 doi 10.1038/nature21350.
54. Butler A, Hoffman P, Smibert P, Papalexi E, Satija R. Integrating single-cell transcriptomic data across different conditions, technologies, and species. Nature biotechnology **2018**;36(5):411-20 doi 10.1038/nbt.4096.
55. Gabrilovich DI. Myeloid-Derived Suppressor Cells. Cancer immunology research **2017**;5(1):3-8 doi 10.1158/2326-6066.CIR-16-0297.
56. Alshetaiwi H, Pervolarakis N, McIntyre LL, Ma D, Nguyen Q, Rath JA*, et al.* Defining the emergence of myeloid-derived suppressor cells in breast cancer using single-cell transcriptomics. Science Immunology **2020**;5(44):eaay6017 doi 10.1126/sciimmunol.aay6017.
57. Honey K. CCL3 and CCL4 actively recruit CD8+ T cells. Nature Reviews Immunology **2006**;6(6):427- doi 10.1038/nri1862.
58. Stuart T, Butler A, Hoffman P, Hafemeister C, Papalexi E, Mauck WM, III*, et al.* Comprehensive Integration of Single-Cell Data. Cell **2019**;177(7):1888-902.e21 doi 10.1016/j.cell.2019.05.031.
59. Elghetany MT. Surface Antigen Changes during Normal Neutrophilic Development: A Critical Review. Blood Cells, Molecules, and Diseases **2002**;28(2):260-74 doi https://doi.org/10.1006/bcmd.2002.0513.
60. Lambert C, Preijers FWMB, Yanikkaya Demirel G, Sack U. Monocytes and macrophages in flow: an ESCCA initiative on advanced analyses of monocyte lineage using flow cytometry. Cytometry Part B: Clinical Cytometry **2017**;92(3):180-8 doi 10.1002/cyto.b.21280.
61. Nunez FJ, Mendez FM, Kadilaya P, Alghamri MS, Savelieff M, Koschmann C*, et al.* IDH1R132H acts as a tumor suppressor in glioma via epigenetic upregulation of the DNA damage response. bioRxiv **2018** doi 10.1101/389817.
62. Casbon AJ, Reynaud D, Park C, Khuc E, Gan DD, Schepers K*, et al.* Invasive breast cancer reprograms early myeloid differentiation in the bone marrow to generate immunosuppressive neutrophils. Proceedings of the National Academy of Sciences of the United States of America **2015**;112(6):E566-75 doi 10.1073/pnas.1424927112.

63. Kawano M, Mabuchi S, Matsumoto Y, Sasano T, Takahashi R, Kuroda H*, et al.* The significance of G-CSF expression and myeloid-derived suppressor cells in the chemoresistance of uterine cervical cancer. Scientific reports **2015**;5:18217 doi 10.1038/srep18217.
64. Meyer MA, Baer JM, Knolhoff BL, Nywening TM, Panni RZ, Su X*, et al.* Breast and pancreatic cancer interrupt IRF8-dependent dendritic cell development to overcome immune surveillance. Nature communications **2018**;9(1):1250 doi 10.1038/s41467-018-03600-6.
65. Casbon A-J, Reynaud D, Park C, Khuc E, Gan DD, Schepers K*, et al.* Invasive breast cancer reprograms early myeloid differentiation in the bone marrow to generate immunosuppressive neutrophils. Proceedings of the National Academy of Sciences **2015**;112(6):E566 doi 10.1073/pnas.1424927112.
66. Parsons DW, Jones S, Zhang X, Lin JC, Leary RJ, Angenendt P*, et al.* An integrated genomic analysis of human glioblastoma multiforme. Science (New York, NY) **2008**;321(5897):1807-12 doi 10.1126/science.1164382.
67. Cancer Genome Atlas Research N, Brat DJ, Verhaak RG, Aldape KD, Yung WK, Salama SR*, et al.* Comprehensive, Integrative Genomic Analysis of Diffuse Lower-Grade Gliomas. The New England journal of medicine **2015**;372(26):2481-98 doi 10.1056/NEJMoa1402121.
68. Wengner AM, Pitchford SC, Furze RC, Rankin SM. The coordinated action of G-CSF and ELR + CXC chemokines in neutrophil mobilization during acute inflammation. Blood **2008**;111(1):42-9 doi 10.1182/blood-2007-07-099648.
69. Petit I, Szyper-Kravitz M, Nagler A, Lahav M, Peled A, Habler L*, et al.* G-CSF induces stem cell mobilization by decreasing bone marrow SDF-1 and up-regulating CXCR4. Nat Immunol **2002**;3(7):687-94 doi 10.1038/ni813.
70. Knudsen E, Iversen PO, Boyum A, Seierstad T, Nicolaysen G, Benestad HB. G-CSF enhances the proliferation and mobilization, but not the maturation rate, of murine myeloid cells. Eur J Haematol **2011**;87(4):302-11 doi 10.1111/j.1600-0609.2011.01658.x.
71. Raychaudhuri B, Rayman P, Ireland J, Ko J, Rini B, Borden EC*, et al.* Myeloid-derived suppressor cell accumulation and function in patients with newly diagnosed glioblastoma. Neuro-oncology **2011**;13(6):591-9 doi 10.1093/neuonc/nor042.
72. Gan Y, Zhou X, Niu X, Li J, Wang T, Zhang H*, et al.* Neutrophil/Lymphocyte Ratio Is an Independent Prognostic Factor in Elderly Patients with High-Grade Gliomas. World neurosurgery **2019**;127:e261-e7 doi https://doi.org/10.1016/j.wneu.2019.03.085.
73. Condamine T, Mastio J, Gabrilovich DI. Transcriptional regulation of myeloid-derived suppressor cells. Journal of leukocyte biology **2015**;98(6):913-22 doi 10.1189/jlb.4RI0515-204R.
74. Condamine T, Gabrilovich DI. Molecular mechanisms regulating myeloid-derived suppressor cell differentiation and function. Trends in immunology **2011**;32(1):19-25 doi 10.1016/j.it.2010.10.002.
75. Serafini P, Borrello I, Bronte V. Myeloid suppressor cells in cancer: recruitment, phenotype, properties, and mechanisms of immune suppression. Semin Cancer Biol **2006**;16(1):53-65 doi 10.1016/j.semcancer.2005.07.005.
76. Vartanian A, Singh SK, Agnihotri S, Jalali S, Burrell K, Aldape KD*, et al.* GBM's multifaceted landscape: highlighting regional and microenvironmental heterogeneity. Neuro-oncology **2014**;16(9):1167-75 doi 10.1093/neuonc/nou035.
77. Inda M-D-M, Bonavia R, Seoane J. Glioblastoma multiforme: a look inside its heterogeneous nature. Cancers **2014**;6(1):226-39 doi 10.3390/cancers6010226.
78. The Cancer Genome Atlas Research N, Chang K, Creighton CJ, Davis C, Donehower L, Drummond J*, et al.* The Cancer Genome Atlas Pan-Cancer analysis project. Nature genetics **2013**;45:1113 doi 10.1038/ng.2764.

79. Wang Q, Hu B, Hu X, Kim H, Squatrito M, Scarpace L*, et al.* Tumor Evolution of Glioma-Intrinsic Gene Expression Subtypes Associates with Immunological Changes in the Microenvironment. Cancer cell **2017**;32(1):42-56 e6 doi 10.1016/j.ccell.2017.06.003.
80. Verhaak RG, Hoadley KA, Purdom E, Wang V, Qi Y, Wilkerson MD*, et al.* Integrated genomic analysis identifies clinically relevant subtypes of glioblastoma characterized by abnormalities in PDGFRA, IDH1, EGFR, and NF1. Cancer cell **2010**;17(1):98-110 doi 10.1016/j.ccr.2009.12.020.
81. Neftel C, Laffy J, Filbin MG, Hara T, Shore ME, Rahme GJ*, et al.* An Integrative Model of Cellular States, Plasticity, and Genetics for Glioblastoma. Cell **2019**;178(4):835-49.e21 doi https://doi.org/10.1016/j.cell.2019.06.024.
82. McLendon R, Friedman A, Bigner D, Van Meir EG, Brat DJ, M. Mastrogianakis G*, et al.* Comprehensive genomic characterization defines human glioblastoma genes and core pathways. Nature **2008**;455(7216):1061-8 doi 10.1038/nature07385.
83. Ding L, Ley TJ, Larson DE, Miller CA, Koboldt DC, Welch JS*, et al.* Clonal evolution in relapsed acute myeloid leukaemia revealed by whole-genome sequencing. Nature **2012**;481(7382):506-10 doi 10.1038/nature10738.
84. Pombo Antunes AR, Scheyltjens I, Duerinck J, Neyns B, Movahedi K, Van Ginderachter JA. Understanding the glioblastoma immune microenvironment as basis for the development of new immunotherapeutic strategies. eLife **2020**;9:e52176 doi 10.7554/eLife.52176.
85. Doucette T, Rao G, Rao A, Shen L, Aldape K, Wei J*, et al.* Immune Heterogeneity of Glioblastoma Subtypes: Extrapolation from the Cancer Genome Atlas. Cancer Immunology Research **2013**;1(2):112 doi 10.1158/2326-6066.CIR-13-0028.
86. Venteicher AS, Tirosh I, Hebert C, Yizhak K, Neftel C, Filbin MG*, et al.* Decoupling genetics, lineages, and microenvironment in IDH-mutant gliomas by single-cell RNA-seq. Science (New York, NY) **2017**;355(6332) doi 10.1126/science.aai8478.
87. Suvà ML, Tirosh I. The Glioma Stem Cell Model in the Era of Single-Cell Genomics. Cancer cell **2020**;37(5):630-6 doi https://doi.org/10.1016/j.ccell.2020.04.001.
88. Patel AP, Tirosh I, Trombetta JJ, Shalek AK, Gillespie SM, Wakimoto H*, et al.* Single-cell RNA-seq highlights intratumoral heterogeneity in primary glioblastoma. Science (New York, NY) **2014**;344(6190):1396-401 doi 10.1126/science.1254257.
89. Modrek AS, Golub D, Khan T, Bready D, Prado J, Bowman C*, et al.* Low-Grade Astrocytoma Mutations in IDH1, P53, and ATRX Cooperate to Block Differentiation of Human Neural Stem Cells via Repression of SOX2. Cell reports **2017**;21(5):1267-80 doi 10.1016/j.celrep.2017.10.009.
90. Lu C, Ward PS, Kapoor GS, Rohle D, Turcan S, Abdel-Wahab O*, et al.* IDH mutation impairs histone demethylation and results in a block to cell differentiation. Nature **2012**;483(7390):474-8 doi 10.1038/nature10860.
91. Otvos B, Silver DJ, Mulkearns-Hubert EE, Alvarado AG, Turaga SM, Sorensen MD*, et al.* Cancer Stem Cell-Secreted Macrophage Migration Inhibitory Factor Stimulates Myeloid Derived Suppressor Cell Function and Facilitates Glioblastoma Immune Evasion. STEM CELLS **2016**;34(8):2026-39 doi 10.1002/stem.2393.
92. Ye X-z, Xu S-l, Xin Y-h, Yu S-c, Ping Y-f, Chen L*, et al.* Tumor-Associated Microglia/Macrophages Enhance the Invasion of Glioma Stem-like Cells via TGF-β1 Signaling Pathway. The Journal of Immunology **2012**;189(1):444-53 doi 10.4049/jimmunol.1103248.
93. Sanchez-Ramos J, Song S, Sava V, Catlow B, Lin X, Mori T*, et al.* Granulocyte colony stimulating factor decreases brain amyloid burden and reverses cognitive impairment in Alzheimer's mice. Neuroscience **2009**;163(1):55-72 doi https://doi.org/10.1016/j.neuroscience.2009.05.071.
94. Li B, Gonzalez-Toledo ME, Piao C-S, Gu A, Kelley RE, Zhao L-R. Stem cell factor and granulocyte colony-stimulating factor reduce β-amyloid deposits in the brains of APP/PS1 transgenic mice. Alzheimer's Research & Therapy **2011**;3(2):8 doi 10.1186/alzrt67.

95. Dolcetti L, Peranzoni E, Ugel S, Marigo I, Fernandez Gomez A, Mesa C*, et al.* Hierarchy of immunosuppressive strength among myeloid-derived suppressor cell subsets is determined by GM-CSF. Eur J Immunol **2010**;40(1):22-35 doi 10.1002/eji.200939903.
96. Marigo I, Bosio E, Solito S, Mesa C, Fernandez A, Dolcetti L*, et al.* Tumor-induced tolerance and immune suppression depend on the C/EBPbeta transcription factor. Immunity **2010**;32(6):790-802 doi 10.1016/j.immuni.2010.05.010.
97. Calinescu A-A, Núñez FJ, Koschmann C, Kolb BL, Lowenstein PR, Castro MG. Transposon mediated integration of plasmid DNA into the subventricular zone of neonatal mice to generate novel models of glioblastoma. Journal of visualized experiments : JoVE **2015**(96):10.3791/52443 doi 10.3791/52443.
98. Koschmann C, Calinescu A-A, Nunez FJ, Mackay A, Fazal-Salom J, Thomas D*, et al.* ATRX loss promotes tumor growth and impairs nonhomologous end joining DNA repair in glioma. Science translational medicine **2016**;8(328):328ra28 doi 10.1126/scitranslmed.aac8228.
99. Alghamri MS, Núñez FJ, Kamran N, Carney S, Altshuler D, Lowenstein PR*, et al.* Chapter Six - Functional characterization of tumor antigen-specific T-cells isolated from the tumor microenvironment of sleeping beauty induced murine glioma models. In: Galluzzi L, Rudqvist N-P, editors. Methods in enzymology. Volume 631: Academic Press; 2020. p 91-106.
100. Hambardzumyan D, Amankulor NM, Helmy KY, Becher OJ, Holland EC. Modeling Adult Gliomas Using RCAS/t-va Technology. Transl Oncol **2009**;2(2):89-95.
101. Baker GJ, Castro MG, Lowenstein PR. Isolation and Flow Cytometric Analysis of Glioma-infiltrating Peripheral Blood Mononuclear Cells. Journal of visualized experiments : JoVE **2015**(105) doi 10.3791/53676.
102. Kamran N, Li Y, Sierra M, Alghamri MS, Kadiyala P, Appelman HD*, et al.* Melanoma induced immunosuppression is mediated by hematopoietic dysregulation. Oncoimmunology **2018**;7(3):e1408750 doi 10.1080/2162402X.2017.1408750.
103. Kotecha N, Krutzik PO, Irish JM. Web-based analysis and publication of flow cytometry experiments. Current protocols in cytometry **2010**;Chapter 10:Unit10 7 doi 10.1002/0471142956.cy1017s53.
104. Qiu P, Simonds EF, Bendall SC, Gibbs KD, Jr., Bruggner RV, Linderman MD*, et al.* Extracting a cellular hierarchy from high-dimensional cytometry data with SPADE. Nat Biotechnol **2011**;29(10):886-91 doi 10.1038/nbt.1991.
105. Langmead B, Trapnell C, Pop M, Salzberg SL. Ultrafast and memory-efficient alignment of short DNA sequences to the human genome. Genome biology **2009**;10(3):R25 doi 10.1186/gb-2009-10-3-r25.
106. Trapnell C, Pachter L, Salzberg SL. TopHat: discovering splice junctions with RNA-Seq. Bioinformatics **2009**;25(9):1105-11 doi 10.1093/bioinformatics/btp120.
107. Trapnell C, Hendrickson DG, Sauvageau M, Goff L, Rinn JL, Pachter L. Differential analysis of gene regulation at transcript resolution with RNA-seq. Nature biotechnology **2013**;31(1):46-53 doi 10.1038/nbt.2450.
108. Subramanian A, Tamayo P, Mootha VK, Mukherjee S, Ebert BL, Gillette MA*, et al.* Gene set enrichment analysis: a knowledge-based approach for interpreting genome-wide expression profiles. Proceedings of the National Academy of Sciences of the United States of America **2005**;102(43):15545-50 doi 10.1073/pnas.0506580102.
109. Macosko Evan Z, Basu A, Satija R, Nemesh J, Shekhar K, Goldman M*, et al.* Highly Parallel Genome-wide Expression Profiling of Individual Cells Using Nanoliter Droplets. Cell **2015**;161(5):1202-14 doi https://doi.org/10.1016/j.cell.2015.05.002.

Figure 1

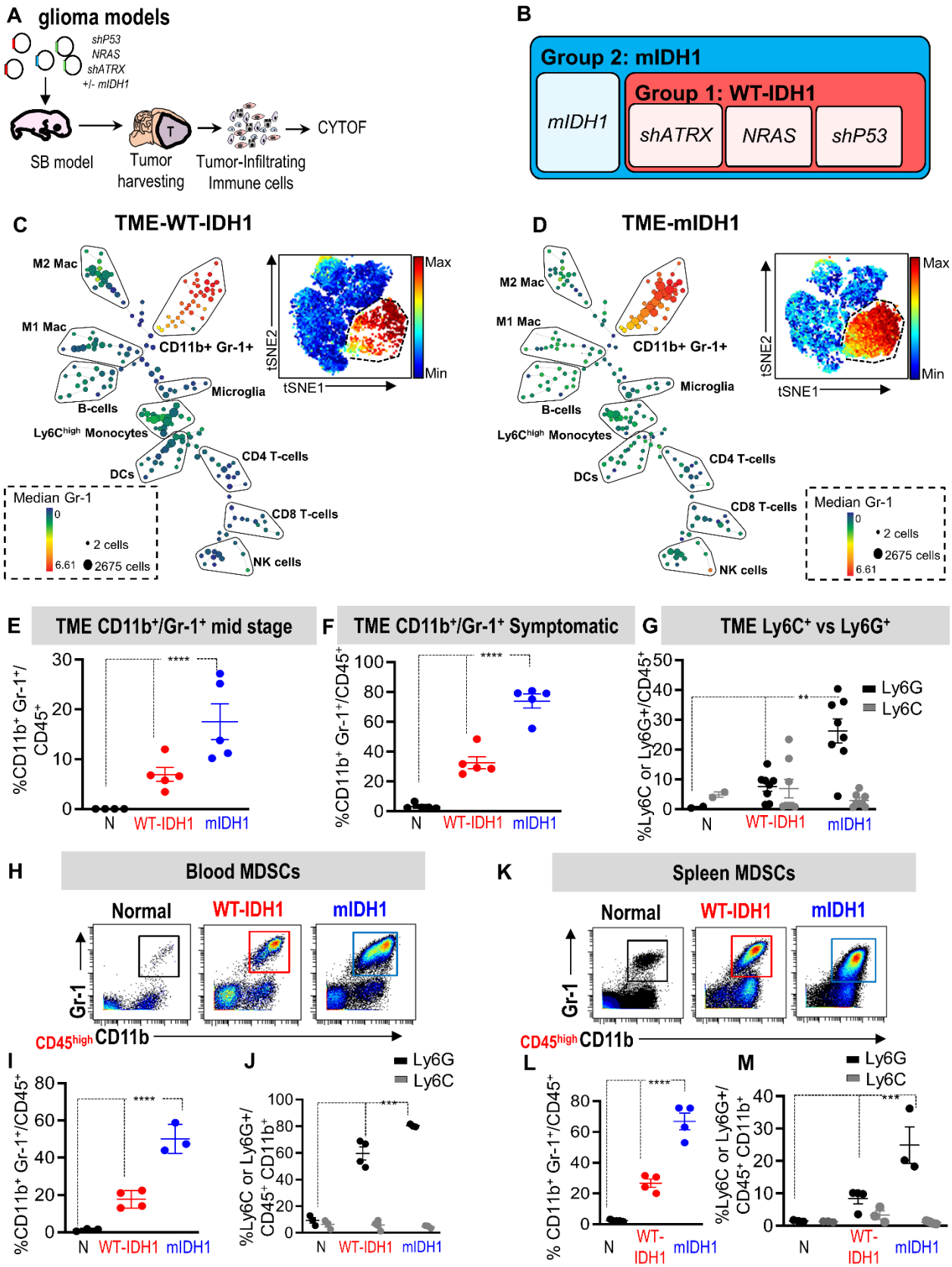
A glioma models
shP53
NRAS
shATRX
+/- mIDH1
SB model
Tumor harvesting
Tumor-Infiltrating Immune cells
CYTOF
B
Group 2: mIDH1
mIDH1
Group 1: WT-IDH1
shATRX
NRAS
shP53
C TME-WT-IDH1
M2 Mac
M1 Mac
CD11b+ Gr-1+
Microglia
B-cells
Ly6C^high Monocytes
DCs
CD4 T-cells
CD8 T-cells
NK cells
tSNE1
tSNE2
Max
Min
Median Gr-1
0
6.61
2 cells
2675 cells
D TME-mIDH1
E TME CD11b+/Gr-1+ mid stage
F TME CD11b+/Gr-1+ Symptomatic
G TME Ly6C+ vs Ly6G+
%CD11b+ Gr-1+/CD45+
%Ly6C or Ly6G+/CD45+
Ly6G
Ly6C
N
WT-IDH1
mIDH1
H Blood MDSCs
Normal
WT-IDH1
mIDH1
Gr-1
CD45^high CD11b
K Spleen MDSCs
I
J
L
M
%CD11b+ Gr-1+/CD45+
%Ly6C or Ly6G+/CD45+ CD11b+

Figure 2

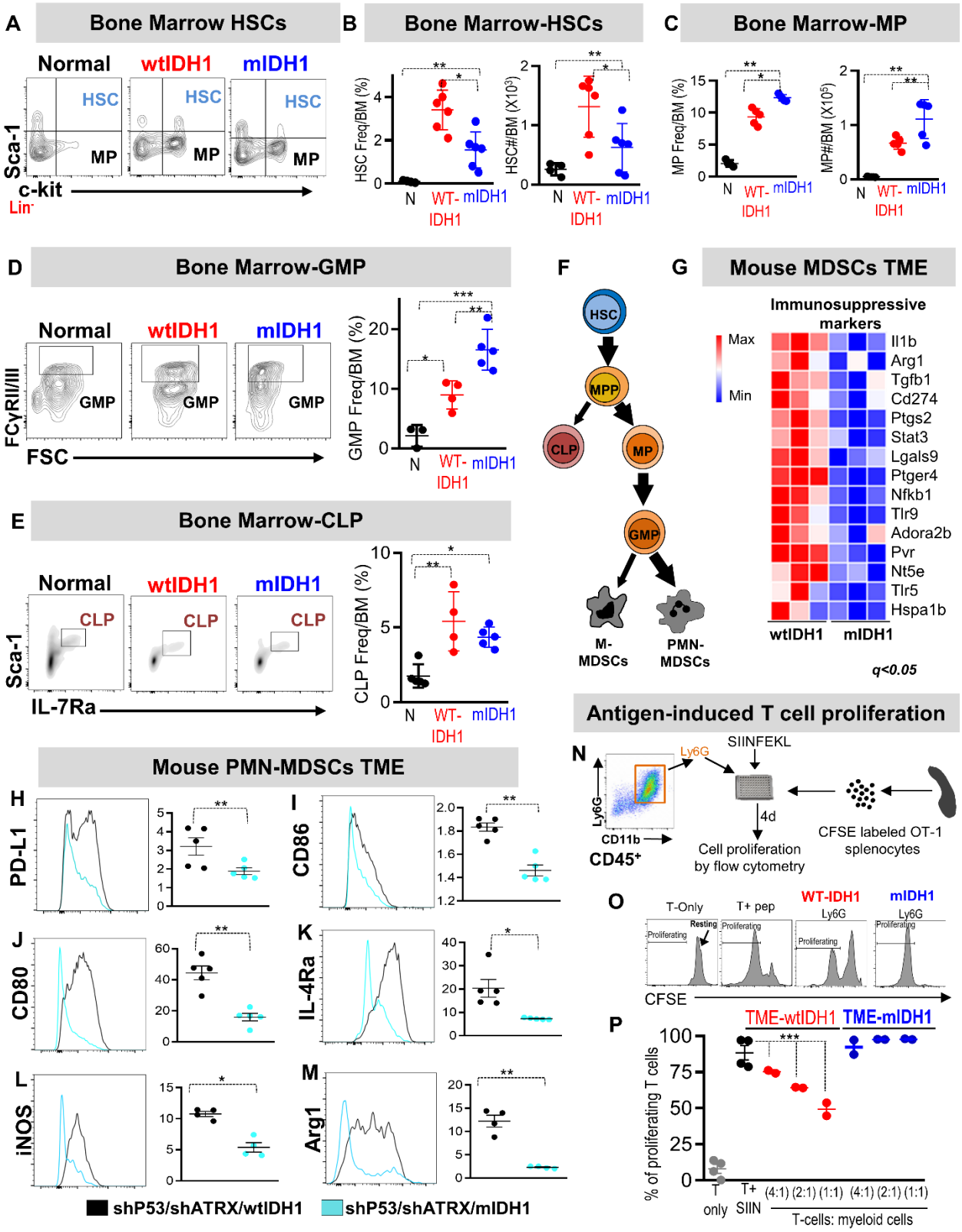
A
Bone Marrow HSCs
Normal
wtIDH1
mIDH1
HSC
MP
Sca-1
c-kit
Lin-
B
Bone Marrow-HSCs
HSC Freq/BM (%)
HSC#/BM (X10³)
N
WT-IDH1
mIDH1
C
Bone Marrow-MP
MP Freq/BM (%)
MP#/BM (X10⁵)
D
Bone Marrow-GMP
GMP
FCγRII/III
FSC
GMP Freq/BM (%)
E
Bone Marrow-CLP
CLP
IL-7Ra
CLP Freq/BM (%)
F
HSC
MPP
CLP
MP
GMP
M-MDSCs
PMN-MDSCs
G
Mouse MDSCs TME
Immunosuppressive markers
Max
Min
Il1b
Arg1
Tgfb1
Cd274
Ptgs2
Stat3
Lgals9
Ptger4
Nfkb1
Tlr9
Adora2b
Pvr
Nt5e
Tlr5
Hspa1b
wtIDH1
mIDH1
q<0.05
Mouse PMN-MDSCs TME
H
PD-L1
I
CD86
J
CD80
K
IL-4Ra
L
iNOS
M
Arg1
shP53/shATRX/wtIDH1
shP53/shATRX/mIDH1
Antigen-induced T cell proliferation
N
Ly6G
SIINFEKL
Ly6G
CD11b
CD45+
4d
Cell proliferation by flow cytometry
CFSE labeled OT-1 splenocytes
O
T-Only
T+ pep
WT-IDH1
mIDH1
Ly6G
Ly6G
Resting
Proliferating
CFSE
P
TME-wtIDH1
TME-mIDH1
% of proliferating T cells
T only
T+ SIIN
(4:1) (2:1) (1:1) (4:1) (2:1) (1:1)
T-cells: myeloid cells

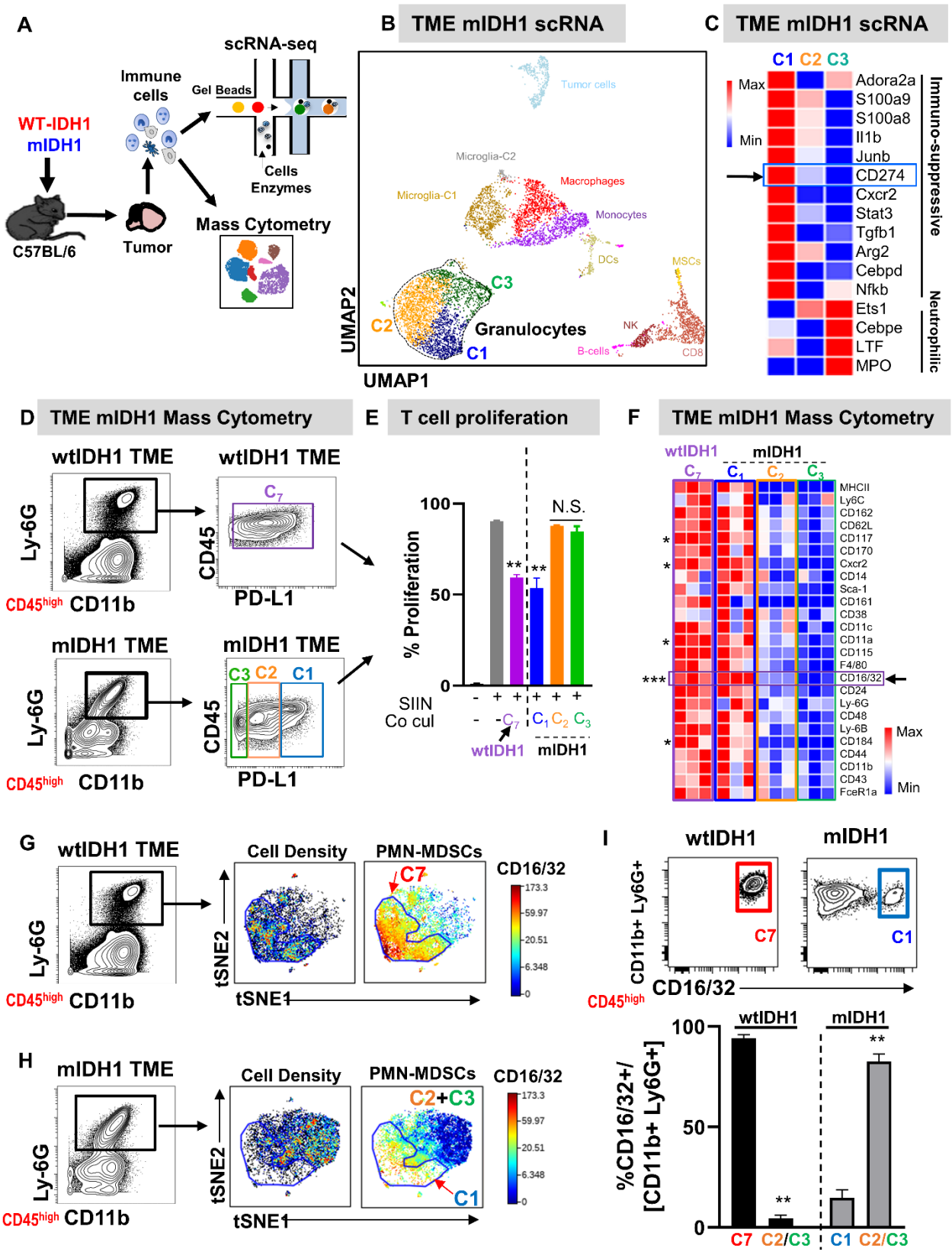
A
WT-IDH1
mIDH1
C57BL/6
Tumor
Immune cells
Gel Beads
scRNA-seq
Cells
Enzymes
Mass Cytometry
B TME mIDH1 scRNA
Tumor cells
Microglia-C2
Microglia-C1
Macrophages
Monocytes
DCs
MSCs
C3
C2
C1
Granulocytes
NK
B-cells
CD8
UMAP2
UMAP1
C TME mIDH1 scRNA
C1 C2 C3
Max
Min
Adora2a
S100a9
S100a8
Il1b
Junb
CD274
Cxcr2
Stat3
Tgfb1
Arg2
Cebpd
Nfkb
Ets1
Cebpe
LTF
MPO
Immuno-suppressive
Neutrophilic
D TME mIDH1 Mass Cytometry
wtIDH1 TME
Ly-6G
CD45high CD11b
CD45
PD-L1
mIDH1 TME
C3 C2 C1
E T cell proliferation
% Proliferation
N.S.
SIIN
Co cul
wtIDH1
mIDH1
F TME mIDH1 Mass Cytometry
MHCII
Ly6C
CD162
CD62L
CD117
CD170
Cxcr2
CD14
Sca-1
CD161
CD38
CD11c
CD11a
CD115
F4/80
CD16/32
CD24
Ly-6G
CD48
Ly-6B
CD184
CD44
CD11b
CD43
FceR1a
Max
Min
G wtIDH1 TME
Cell Density
PMN-MDSCs
CD16/32
tSNE2
tSNE1
H mIDH1 TME
C2+C3
I wtIDH1
mIDH1
CD11b+ Ly6G+
%CD16/32+/
[CD11b+ Ly6G+]
C7 C2/C3 C1 C2/C3

Figure 4

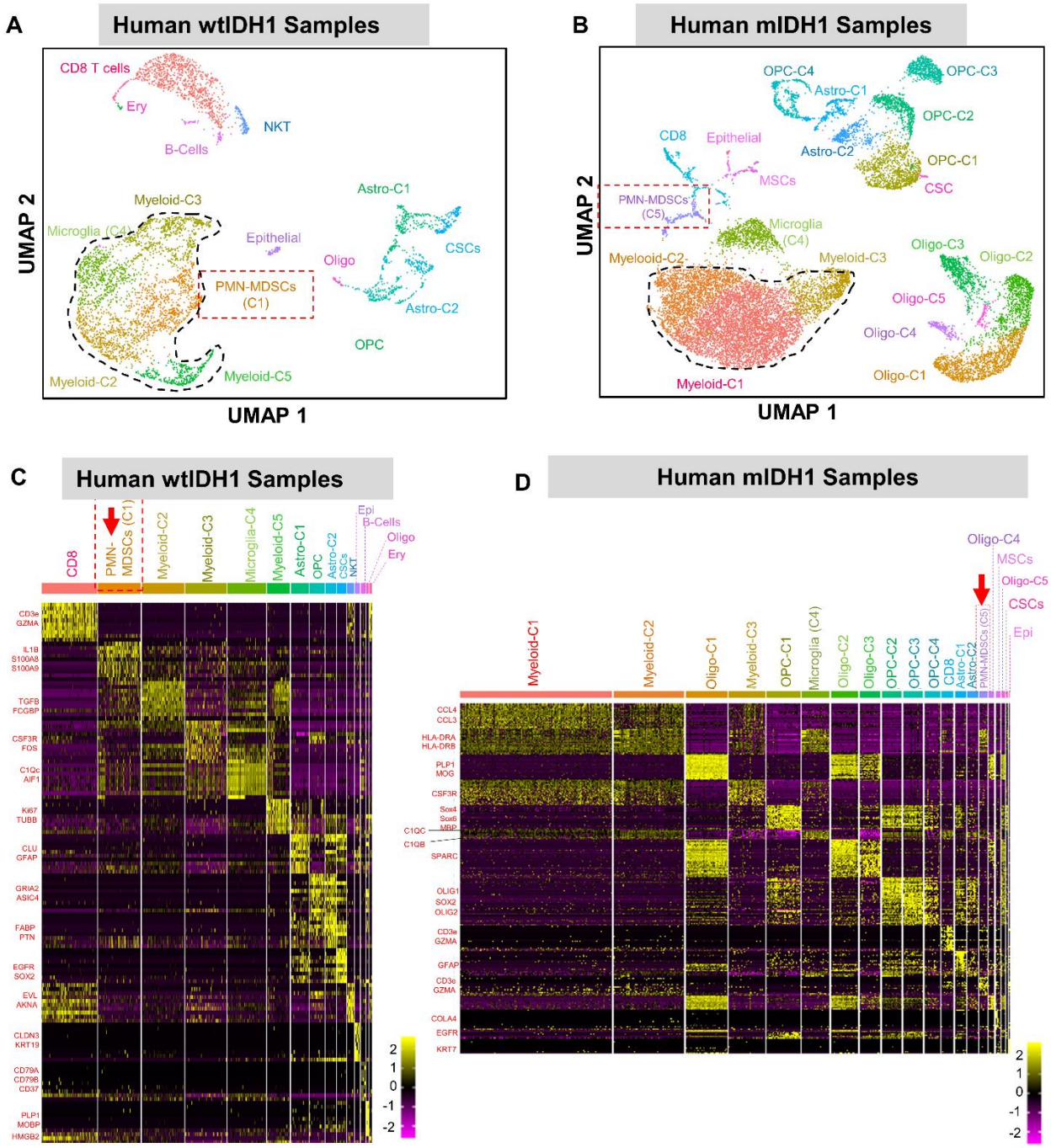
A
Human wtIDH1 Samples
CD8 T cells
Ery
NKT
B-Cells
Myeloid-C3
Microglia (C4)
Epithelial
Astro-C1
CSCs
Oligo
PMN-MDSCs (C1)
Astro-C2
OPC
Myeloid-C2
Myeloid-C5
UMAP 2
UMAP 1
B
Human mIDH1 Samples
OPC-C4
OPC-C3
Astro-C1
OPC-C2
CD8
Epithelial
Astro-C2
OPC-C1
MSCs
CSC
PMN-MDSCs (C5)
Microglia (C4)
Myelooid-C2
Myeloid-C3
Oligo-C3
Oligo-C2
Oligo-C5
Oligo-C4
Oligo-C1
Myeloid-C1
UMAP 2
UMAP 1
C
Human wtIDH1 Samples
CD8
PMN-MDSCs (C1)
Myeloid-C2
Myeloid-C3
Microglia-C4
Myeloid-C5
Astro-C1
OPC
Astro-C2
CSCs
NKT
Epi
B-Cells
Oligo
Ery
CD3e GZMA
IL1B S100A8 S100A9
TGFB FCGBP
CSF3R FOS
C1Qc AIF1
Ki67 TUBB
CLU GFAP
GRIA2 ASIC4
FABP PTN
EGFR SOX2
EVL AKNA
CLDN3 KRT19
CD79A CD79B CD37
PLP1 MOBP HMGB2
2
1
0
-1
-2
D
Human mIDH1 Samples
Oligo-C4
MSCs
Oligo-C5
CSCs
Epi
Myeloid-C1
Myeloid-C2
Oligo-C1
Myeloid-C3
OPC-C1
Microglia (C4)
Oligo-C2
Oligo-C3
OPC-C2
OPC-C3
OPC-C4
CD8
Astro-C1
Astro-C2
PMN-MDSCs (C5)
CCL4 CCL3
HLA-DRA HLA-DRB
PLP1 MOG
CSF3R
Sox4 Sox6 MBP
C1QC
C1QB
SPARC
OLIG1 SOX2 OLIG2
CD3e GZMA
GFAP
CD3e GZMA
COLA4
EGFR
KRT7
2
1
0
-1
-2

Figure 5

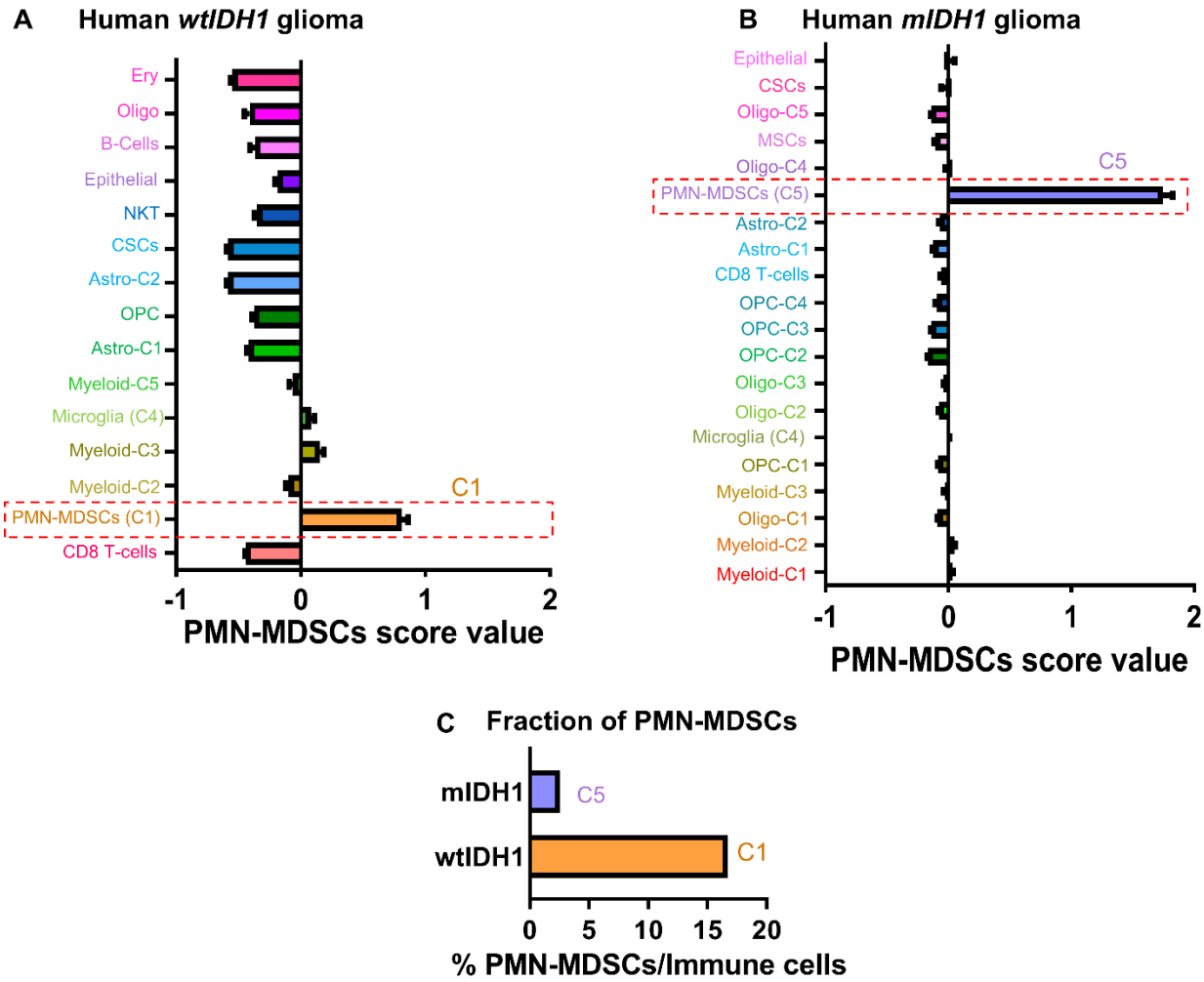
A
Human wtIDH1 glioma
Ery
Oligo
B-Cells
Epithelial
NKT
CSCs
Astro-C2
OPC
Astro-C1
Myeloid-C5
Microglia (C4)
Myeloid-C3
Myeloid-C2
PMN-MDSCs (C1)
CD8 T-cells
C1
-1
0
1
2
PMN-MDSCs score value
B
Human mIDH1 glioma
Epithelial
CSCs
Oligo-C5
MSCs
Oligo-C4
PMN-MDSCs (C5)
Astro-C2
Astro-C1
CD8 T-cells
OPC-C4
OPC-C3
OPC-C2
Oligo-C3
Oligo-C2
Microglia (C4)
OPC-C1
Myeloid-C3
Oligo-C1
Myeloid-C2
Myeloid-C1
C5
-1
0
1
2
PMN-MDSCs score value
C
Fraction of PMN-MDSCs
mIDH1
C5
wtIDH1
C1
0
5
10
15
20
% PMN-MDSCs/Immune cells

Figure 6

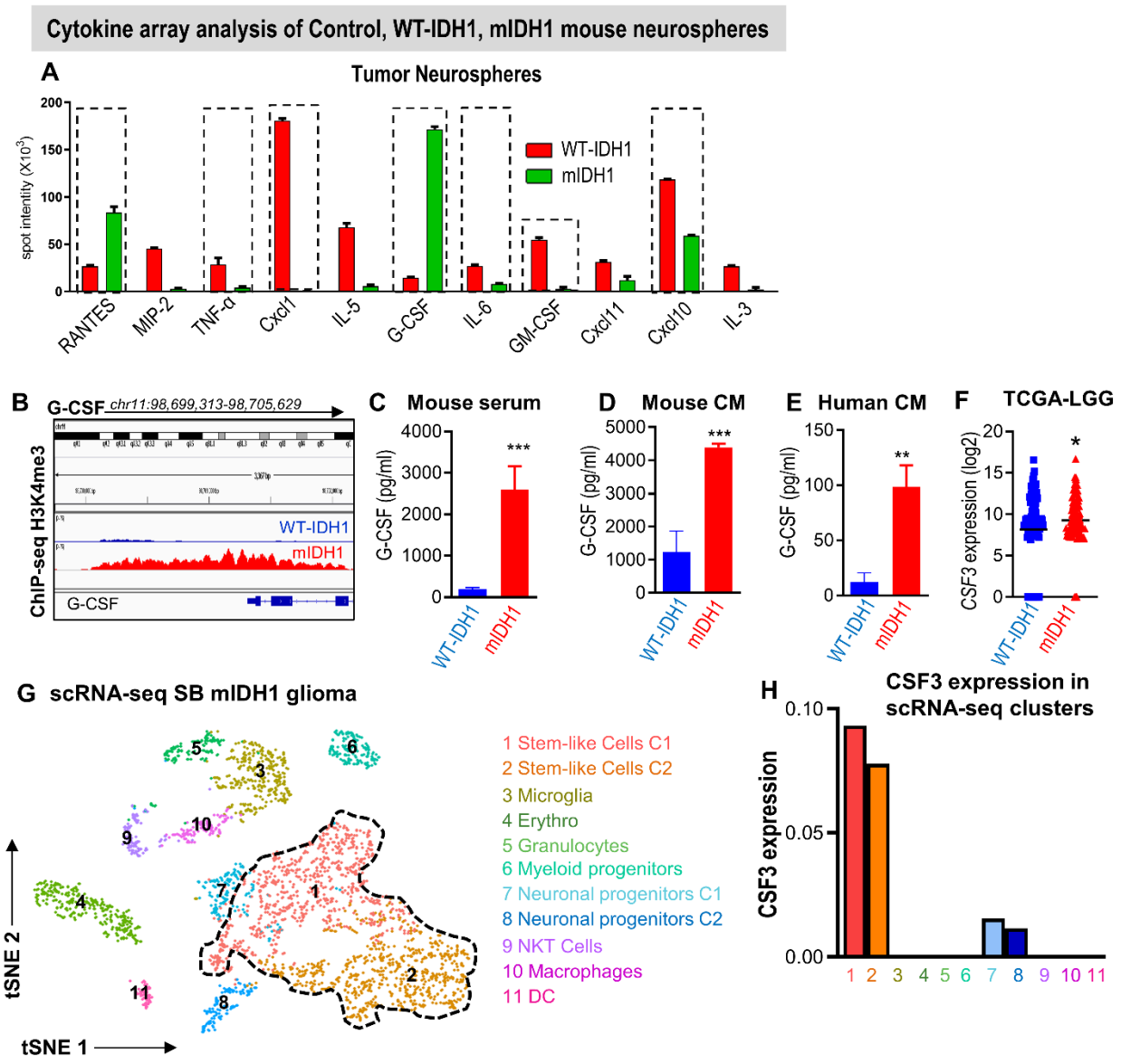
Cytokine array analysis of Control, WT-IDH1, mIDH1 mouse neurospheres
A
Tumor Neurospheres
spot intentity (X10^3)
WT-IDH1
mIDH1
RANTES
MIP-2
TNF-α
Cxcl1
IL-5
G-CSF
IL-6
GM-CSF
Cxcl11
Cxcl10
IL-3
B
G-CSF chr11:98,699,313-98,705,629
ChIP-seq H3K4me3
WT-IDH1
mIDH1
G-CSF
C Mouse serum
D Mouse CM
E Human CM
F TCGA-LGG
G-CSF (pg/ml)
CSF3 expression (log2)
G scRNA-seq SB mIDH1 glioma
tSNE 1
tSNE 2
1 Stem-like Cells C1
2 Stem-like Cells C2
3 Microglia
4 Erythro
5 Granulocytes
6 Myeloid progenitors
7 Neuronal progenitors C1
8 Neuronal progenitors C2
9 NKT Cells
10 Macrophages
11 DC
H
CSF3 expression in scRNA-seq clusters
CSF3 expression

Figure 7

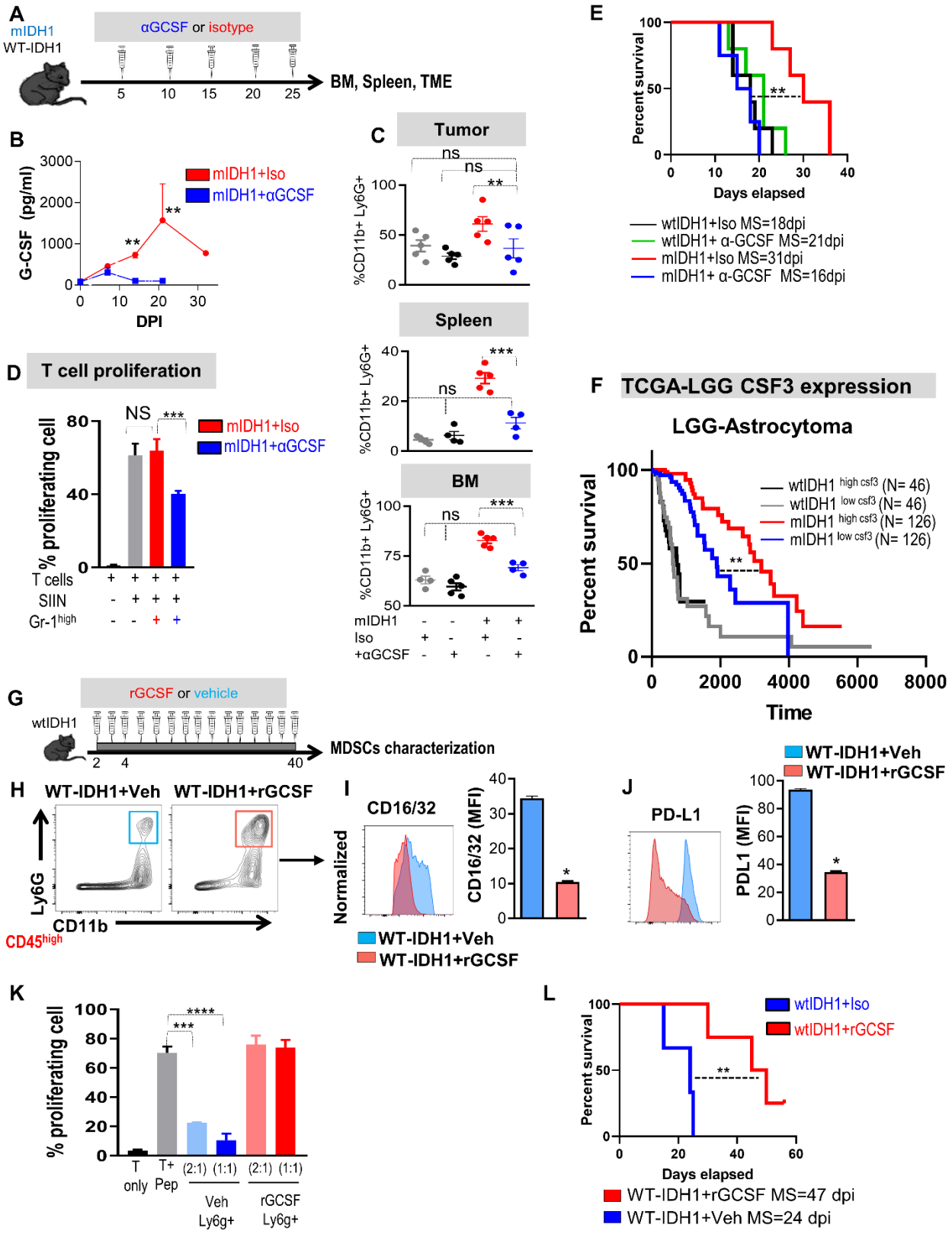
A
mIDH1
WT-IDH1
αGCSF or isotype
5
10
15
20
25
BM, Spleen, TME
B
G-CSF (pg/ml)
mIDH1+Iso
mIDH1+αGCSF
DPI
C
Tumor
%CD11b+ Ly6G+
ns
**
Spleen
***
BM
mIDH1
Iso
+αGCSF
D
T cell proliferation
% proliferating cell
NS
***
T cells
SIIN
Gr-1high
E
Percent survival
Days elapsed
wtIDH1+Iso MS=18dpi
wtIDH1+ α-GCSF MS=21dpi
mIDH1+Iso MS=31dpi
mIDH1+ α-GCSF MS=16dpi
F
TCGA-LGG CSF3 expression
LGG-Astrocytoma
wtIDH1 high csf3 (N= 46)
wtIDH1 low csf3 (N= 46)
mIDH1 high csf3 (N= 126)
mIDH1 low csf3 (N= 126)
Time
G
wtIDH1
rGCSF or vehicle
MDSCs characterization
H
WT-IDH1+Veh
WT-IDH1+rGCSF
Ly6G
CD11b
CD45high
I
CD16/32
Normalized
CD16/32 (MFI)
J
PD-L1
PDL1 (MFI)
K
% proliferating cell
****
T only
T+ Pep
(2:1)
(1:1)
Veh Ly6g+
rGCSF Ly6g+
L
wtIDH1+Iso
wtIDH1+rGCSF
WT-IDH1+rGCSF MS=47 dpi
WT-IDH1+Veh MS=24 dpi

Supplementary Materials

CONTACT FOR REAGENT AND RESOURCE SHARING

Further information and requests for resources and reagents should be directed to and will be fulfilled by the corresponding authors, Maria G. Castro (mariacas@med.umich.edu) or Pedro R Lowenstein (Pedrol@med.umich.edu).

EXPERIMENTAL MODEL AND SUBJECT DETAILS

6-8 weeks old wild type C57BL/6 female mice (Taconic) were housed under standard specific pathogen-free conditions. All animal procedures were carried out in accordance with the University of Michigan's Institutional Animal Care and Use Committee. All animals were housed in an AAALAC accredited animal facility.

Genetically engineered murine glioma models

A murine model of mIDH1 glioma and their cognate controls were created using the Sleeping Beauty (SB) Transposon system which allows the integration of genetic lesions into the genome of neonatal mice(46,97,98). Tumors then develop intracranially *de novo* from neural progenitor cells. Plasmids encoding these genetic lesions are (i) SB transposase and luciferase (pT2C-LucPGK-SB100X, henceforth referred to as SB/Luc) (47,48,61), (ii) a short hairpin against p53 (pT2-shp53-GFP4, henceforth referred to as shp53), (iii) an NRAS-G12V activating mutation (pT2CAG-NRASV12, henceforth referred to as NRAS), (iv) a short hairpin against ATRX (pT2-shATRX53-GFP4, henceforth referred to as shATRX)(46-48), and (v) mutant IDH1-R132H (pKT-IDH1(R132H)-IRES-Katushka, henceforth referred to as mIDH1(19), Supplementary Table S6. SB/Luc, shp53, and NRAS plasmids were the generous gift of Dr. John Ohlfest

(University of Minnesota). The genotype of the genetically engineered mice involved these combinations: (i) shp53, NRAS, and shATRX (wt-IDH1), (ii) shp53, NRAS, shATRX, and IDH1-R132H (mIDH1). Mice were injected according to a previously described protocol (48). Briefly, plasmids were mixed in mass ratios of 1:2:2; 1:2:2:2, or 1:2:2:2:2 (20 µg plasmid in a total of 40 µL plasmid mixture) with *in vivo*-jetPEI reagent (Polyplus Transfection) (2.8 µL per 40 µL plasmid mixture) and dextrose (5% total). The transfection mixture was incubated for 20 min at room temperature and then maintained in ice before injection. The lateral ventricle (1.5 mm AP, 0.7 mm lateral, and 1.5 mm deep from lambda) of neonatal mice (P01) was injected with 0.75 µL plasmid mixture (0.5 µL/min) that included: (1) SB/Luc, (2) NRAS, (3) shp53, (4) with or without shATRX, and (5) with or without IDH1-R132H (46).

Generation of primary mouse glioma neurospheres (NS)

Mouse glioma neurospheres were generated by harvesting brain tumors at the time of euthanasia by transcardial perfusion with Tyrode's solution only. The brains were excised, and the tumors generated using the SB Transposon System were identified by GFP and Katushka expression under an epifluorescence microscope at the time of resection (Fig 1a). The tumor mass was dissociated using non-enzymatic cell dissociation buffer (Gibco, 13151-014), filtered through a 70 µm strainer and maintained in neural stem cell medium [DMEM/F12 with L-Glutamine (Gibco, 11320-033), B-27 supplement (1X) (Gibco, 12587-010), N-2 supplement (1X) (Gibco, 17502-048), penicillin-streptomycin (100 U/mL) (Cellgro, 30-001-CI), and Normocin (1X) (InvivoGen, ant-nr-1)] at 37 °C, 5% CO2. FGF and EGF (Shenandoah Biotech, 100-26, 100-146) were added twice weekly at 1 µL (20 ng/µL each stock, 1000x formulation) per 1 mL medium. Cells expressing GFP and Katushka were sorted by Flow cytometry.

Generation of a mouse mIDH1 glioma model independent of RAS activating mutations

Mice: Previously characterized Ntv-a/Ink4a-Arf$^{-/-}$ / Pten$^{fl/fl}$ and Ntv-a/Pten$^{fl/fl}$ mice in the age range of 4-8 weeks were used. Ntv-a/Ink4a-Arf-/-/Pten$^{fl/fl}$ was in a mixed genetic background, whereas Ntv-a/Ptenfl/fl was in C57BL/6 background, and they were generated by 10 generations of crosses (46,100).

RCAS transfections: Tumors were generated by injection of DF-1 (ATCC, CRL-12203) cells transfected with a combination of RCAS plasmids (RCAS PDGFB-HA, RCAS shp53-RFP, and RCAS IDH1 wildtype or RCAS IDH1 R132H) using the Fugene 6 transfection kit (Roche, 11814443001) according to the manufacturer's protocol and as previously described (36,50).

Intracranial injections of transfected DF-1 cells: Injections were performed using a stereotactic fixation device (Stoelting). Mice were first anesthetized with ip injections of ketamine (0.1 mg/g) and xylazine (0.01 mg/g). A local injection of bupivacaine was used as an analgesic. One microliter of $4x10^4$ transfected DF-1 cells in suspension was delivered using a 30-gauge needle attached to a Hamilton syringe. The location of injection was AP 1.7 mm from bregma, Lat 0.5 mm, and depth 2 mm from the dural surface, was determined according to the coordinates in the mouse brain atlas to target the right frontal striatum. Buprenorphine was administered to mice for pain relief post-injection. They were continually monitored and sacrificed when they displayed endpoint symptoms (lethargy, scruffy coat, hunched posture).

Tissue processing and generation of primary neurospheres: Upon development of terminal symptoms, mice were anesthetized with ip injections of ketamine (0.1 mg/g) and xylazine (0.01 mg/g) and perfused with cold, sterile Ringer's solution (Sigma-Aldrich, 96724). The brains were then extracted, placed in NeuroCult basal medium (Stemcell Technologies, 05701). The tumor mass was dissociated mechanically by using a sterile pestle and moving it in up and down motion 20 times under laminar flow hood, then 1 ml non-enzymatic cell dissociation buffer (Thermo Hyqtase, Fisher Scientific, Gibco, 13151-014) was added and the mixture was incubated for 5 min at 37 °C. Subsequently, the suspension was filtered through a 70 µm strainer and maintained in neural stem cell medium [DMEM/F12 with L-Glutamine (Gibco, 11320-033), B-27 supplement (1X) (Gibco, 12587-010), N-2 supplement (1X) (Gibco, 17502-048), penicillin-streptomycin (100 U/mL) (Corning, Cellgro, 30-001-CI), and Normocin (1X) (InvivoGen, ant-nr-1)]. To collect the neurospheres, the cell suspension was centrifuged at 500 × *g*, the supernatant was discarded, and neurospheres were re-suspended into 6 mL of NS media, plated into a T-25 (Thermofisher scientific) culture flask and maintained at 37 °C (5% CO_2). FGF and EGF (Shenandoah Biotech, 100-26, 100-146) were added twice weekly at 1 µL (20 ng/µL each stock, 1000x formulation) per 1 mL medium (46). After 3 days in culture a mixed population of cells can be identified morphologically as: (i) adherent cells; (ii) dead cells and (iii) glioma neurospheres. Glioma neurospheres population can be identified by the floating cell clusters, they were isolated and plated in a new T-25 culture flask.

Mouse glioma cells stably transfected to knock down ATRX: Neurospheres were generated as detailed above from both the wtIDH1 and mIDH1 glioma models in the context of PDGFB/shP53/Ink4a/Arf$^{-/-}$, which do not encode RAS activating mutations. Neurospheres were

transfected with pT2-shATRX-GFP (Addgene plasmid number 124259), or pMax-GFP™ vector (Lonza) using the P3 primary cell 4D-Nucleofector™ X kit (Lonza, Allendale, NJ). The procedure

was as follow: neurospheres from 80–90% confluent T75 flask were centrifuge at 500 × *g*, and the supernatant was discarded by decantation. Neurospheres were dissociated by using 1 mL of Accutase® cell detachment solution (Biolegend), incubated for 90 sec at 37 °C, then the accutase was neutralized with 9 mL HBSS. Neurospheres were centrifuged again at 500 × *g* to separate the supernatant. Neurospheres were resuspended again in 10 ml HBSS, counted, and 200,000 cells were transferred into another tube. Each tube was spun at 90 × *g* for 10min at room temperature. Neurospheres were re-suspended with 20µl of transfection solution (4D-Nucleofector solution), and 500ng of either pT2-shATRX-GFP or pMax-GFP™ vector were added to each tube in duplicate. Each tube was mixed gently by pipetting and incubated for 5 min at room temperature. The mixture was transferred into Nucleocuvette™ Vessel, placed into the retainer of the 4D-Nucleofector™ X Unit, and ran using pulse code: EN138. Successful transfection was confirmed and neurospheres were sorted for at least 3 passages (based on GFP expression) before they were used for implantation.

Intracranial Implantation: Tumor implantation was done as described before (101). Briefly, mice are anesthetized using ketamine and dexmedetomidine prior to stereotactic implantation with 5 x 10^4 PDGFB/shP53/shATRX/Ink4a/Arf$^{-/-}$ wtIDH1 or mIDH1 neurospheres in the right striatum. The coordinates for implantation are 0.5 mm anterior and 2.0 mm lateral from the bregma and 3.0 mm ventral from the dura. Neurospheres were injected at a rate of 1 µL/min. Mice were

given a combination of buprenorphine (0.1mg/kg) and carprofen (5mg/kg) for analgesia. At symptomatic stage, tumors were isolated and immune cells were characterized as described in the flow cytometry section (see below).

Human glioma cells stably transfected to express IDH1^{R132H}

SJGBM2 pediatric glioma cells are ATRX mutant (original female donor) and they were a kind gift by the Children's Oncology Group (COG) Repository, Health Science Center, Texas Tech University; these cells were cultured in IMDM medium with L-glutamine (0.3 mg/mL) (Gibco,12440-053), 20% FBS (Gibco,10437-028), and antibiotic-antimycotic (1X) (Gibco, 15240-062) at 37 °C, 5% CO2. SJGBM2 cells (1.5 x 105 each per well) were seeded in a 6-well plate, and after 24 hours they were transfected with p-CMV-IDH1-R132H-Entry plasmid (Origene, RC400096) using jetPRIME transfection system (Polyplus, 114-07) according to the manufacturer's instructions and as described before (19). One day after transfection, the medium was replaced by a selection medium containing G418 (Geneticin; Gibco, 10131-035) at a concentration of 800 µg/mL cells. On day 15 of selection, individual cell colonies were taken from the well using autoclaved filter paper (Whatman, 1001-185) squares (2x2 mm approx.) previously embedded in HyQTase Cell Detachment Solution (GE Healthcare Life Science, HyClone, SV30030.01) and placed in wells of 24-well plates with the appropriate cell culture medium. After 24 hours, the medium was replaced with selection medium.

***In vivo* imaging**

In vivo imaging was performed as described previously (25,47). Briefly, *in vivo* bioluminescence was measured using an IVIS Spectrum (Perkin Elmer, 124262) imaging system. For the IVIS spectrum, the following settings were used: automatic exposure, large binning, and aperture f =

1. To monitor the SB plasmid uptake in neonatal pups, 30 µL of luciferin (30 mg/mL) was injected subcutaneously into each pup 24 hours after plasmid injection. For *in vivo* imaging of tumor formation and progression in adult mice, 100 µL of luciferin solution was injected ip, and mice were then anesthetized with oxygen/isoflurane (1.5-2.5% isoflurane). To score luminescence, Living Image Software Version 4.3.1 (Caliper Life Sciences) was used. A region of interest (ROI) was defined as a circle over the head, and luminescence intensity was measured using the calibrated unit's photons/s/cm2/sr. Multiple images were taken over 15 minutes following injection, and maximal intensity was reported. For survival studies, animals were monitored daily for signs of morbidity, including ataxia, impaired mobility, hunched posture, seizures, and scruffy fur. Animals displaying symptoms of morbidity were euthanized.

Flow cytometry

For isolation and characterization of tumor-infiltrating immune cells, mice were euthanized and tumors were extracted. Tumor mass within the brain was carefully dissected and homogenized using Tenbroeck (Corning) homogenizer in DMEM media containing 10% FBS. Then, the tumor was placed onto a 70 µm strainer attached to a 50 mL conical tube, filled with 10 mL of DMEM media supplemented with 10% FBS. Using the plunger end of a syringe, isolated tumor was carefully mashed and cells were forced through the 70 µm strained (Alkali Scientific Inc.,) on ice. The strainer was washed two times with 10 mL complete media to force cells through and to minimize cell loss. Then, tumor-infiltrating immune cells were enriched using with 30% / 70% Percoll (GE Lifesciences) density gradient. Briefly, cells were centrifuged and the supernatant was discarded. Then, cells were resuspended in 7 mL of complete media (in 15 mL Falcon tube), and 3 ml of 90% stock isotonic percoll™ (SIP, GE Healthcare) were added and mixed well by

pipetting up and down 3–5 times. To layer the 70% percoll™ under the 30% percoll™ gradient, 1 mL serological pipette was filled with 1 mL of 70% percoll™ and pushed it to the bottom of the 15 mL falcon tube and the 70% percoll™ was slowly released making sure a clear interface is formed between the two gradients. Finally, the solution was spun at 800 × *g* for 20 min at room temperature and the tumor-infiltrating immune cells were collected by carefully isolating the white band that formed at the interface between the two gradients. For splenocytes isolation, freshly isolated spleens were mashed on the surface of 70µm sterile cell strainer (Alkali Scientific Inc.,) using a syringe plunger. Cells were flushed with 20ml of DMEM+10% FBS to force cells through the strainer and to minimize cell loss. Blood was isolated from anesthetized mice by decapitation and was directly added to an EDTA-coated tubes (Fisher Scientific). Bone marrow cells were extracted by flushing freshly isolated tibia and femur with DMEM+10% FBS using a syringe with a 30G needle until the bone is clear. All cells were then centrifuged, and RBCs were lysed using 2 ml RBCs lysis buffer (Biolegend) after which they were washed with DPBS and prepared for antibody staining.

For antibody staining, cells were resuspended in PBS containing 2% FBS and non-specific antibody binding was blocked with FC block (CD16/CD32). Dendritic cells were labeled with CD45, CD11c, CD11b, and MHCII antibodies. Macrophages were labeled with CD45, F4/80, CD11b, and CD206 antibodies. T-cells were labeled with CD45, CD3, and CD8 or CD4 for CD8 T-cells and CD4 T-cells, respectively. Cells were first stained with viability dye (Amcyan or Alexa Fluor® 780, fisher scientific) to label the dead cells. After which cells were blocked with either fluorescence conjugated CD16/32 or FC block according to the experimental design for 10 min at 4° C. Cells were then stained with fluorescence conjugated antibodies cocktail for 30 min at 4° C after which they were washed 2X with BD FACS Flow Sheath Fluid (Becton Dickinson).

All flow data were acquired on FACSAria II flow cytometer (BD Biosciences) and analyzed using Flow Jo version 10 (Treestar Inc.). All primary fluorescence-labeled antibodies used for flow cytometry staining are listed in Supplementary Table S2. The expression of immunosuppressive/ co-stimulatory molecules was calculated using the geometric mean by the flow jo software after performing appropriate gating and data normalization to the matching antibody isotype control. All gating strategies used to identify the immune cells are listed in Supplementary Table S3. For the hematopoietic stem cells (HSCs) and myeloid progenitors (MPs), cells from BM or spleens were extracted as described above, counted, and were first stained with CD16/CD32 (FcγRII/III) for 20 mins on ice to prevent non-specific binding of antibodies to the FC receptors. Cells were then centrifuged at 300 *x g* at 4° C for 5 mins, followed by staining with the following antibodies cocktail: lineage cocktail, c-kit, Sca-1, CD34, and IL7Rα antibodies. 5–6 × 10^6 cells were used for staining from each sample to be able to acquire a sufficient number of stem cells and myeloid progenitor populations. HSCs were identified as Lin^-, $Thy1.1^{low}$, $ckit^+$, and $Sca\text{-}1^+$, MPs were identified as Lin^-, $Thy1.1^{low}$, $ckit^+$, and $Sca\text{-}1^-$ (102). The Granulocyte-macrophages progenitors (GMP) were gated from MPs population and were identified using Lin^-, IL-7Rα^-, c-kit^+, $Sca\text{-}1^-$, $CD34^+$, $FcyRII/III^{high}$, whereas common lymphocyte progenitors (CLPs) population were determined as c-kit^{low}, $Sca\text{-}1^{low}$, Lin^-, IL-7Rα^+. All staining was carried out at 4°C for 30 mins. Post staining, cells were washed twice with BD FACS Flow Sheath Fluid and run on the FACSAria flow cytometer (BD Biosciences). Data were analyzed using Flow Jo version 10 (Tree Star, Inc.).

Mass cytometry

Mass cytometry was performed in collaboration with Indiana University Flow Cytometry Core using Cytof2 system. All antibodies were titrated and validated for overlapping using Maxpar Panel Designer tool (Fluidigm). For titration, all antibodies were separated into two panels to avoid overlapping spectrum. After the two panels were created, each antibody was diluted to a concentration of 5µg/ml in Maxpar cell staining buffer (Cat no. 201068). Then, serial dilutions of each panel were performed to obtain the following dilutions 2.5µg/ml, 1.25µg/ml, 0.6 µg/ml, 0.32µg/ml, and 0.15µg/ml. Splenocytes isolated from a naïve wild type mouse were used to perform the antibody staining for each tube (see staining protocol in the next paragraph) and the optimal concentration for each antibody was determined based on the ideal separation between the positive and negative population.

The staining was performed following the manufacturer protocol as follows: single-cell suspensions were extracted from brain, blood, spleen, and bone marrow as described in the flow cytometry section (see above). First, up to 1×10^7 cells were cleaned by removing debris and dead cells using dead cell removal kit (Miltenyi Biotec). Next, cells were stained with cisplatin 1.67µM (Cell-ID Cisplatin; Fluidigm) form 5 min at room temperature to label dead cells. After quenching Cisplatin reaction with 5X volume of MaxPar® Cell Staining Buffer, cells were counted and centrifuged at 300 × g for 5 minutes. Then, $2\text{-}3\times10^6$ cells were stained with a cocktail of pre-titrated metal-conjugated surface antibodies which were added at the appropriate concentration (determined by the antibodies titration) to each sample for 30min. Samples were washed 2X with MaxPar® Cell Staining Buffer. Samples were fixed and permeabilized with 1.6% of freshly prepared formaldehyde and incubated for 10 min at room temperature. After being washed twice in 1ml MaxPar® Fix and Perm Buffer, they were stained with an intracellular antibody cocktail and incubated for 30 min at room temperature. After being washed

once with 2 ml MaxPar® Cell Staining Buffer, cells were re-suspended in 2 ml cell intercalation solution (125 nM Cell-ID Intercalator-Ir in Maxpar Fix and Perm Buffer) for 24 hrs at 4°C to labels the nucleated cells and shipped to Indiana University Simon Cancer Center Flow Cytometry for CyTOF2 Mass Cytometer analysis. Before loading the samples, cells were washed with Maxpar® water counted, and diluted to the appropriate concentration. The output signals were normalized using EQ™ Four Element Calibration beads. Cytobank software was used to perform population gating and advanced data analysis (103).

Mass cytometry data analysis

FCS files were analyzed using the Premium CytoBank Software (cytobank.org). Data were checked for quality of staining and normalized by the use of internal bead standards. First, Cells were separated from the beads by Ir191 DNA Intercalator which labeled nucleated cells. Then, singlets live cells were identified based on the event length cells and Pt195 Cisplatin stain intensity. Finally, immune cells were gated base on $CD45^{high}$ and downstream gating was performed as described in the flow cytometry section (see above) and in the gating strategy in Supplementary Table S3. Unbiased identification of cellular subpopulations was performed in parallel using two approaches – visualization through either viSNE within CytoBank (49) and the SPADE (104). SPADE clustering parameters were as follow: ArcSinh transformation with a factor of 5, target number of nodes= 100 for the minimum spanning tree graph, downsampling to **10 percent, and using symmetric scaling**. For viSNE visualization, cells were gated on live $CD45^{+}$ $CD11b^{+}$ $Ly6G^{+}$ population, and only myeloid-specific markers were selected by performing viSNE clustering in both wtIDH1 and mIDH1 TME. For heatmap visualization of myeloid markers of clusters C1, C2, and C3, the transformed median marker intensities for each

cluster were exported and visualized using Morpheus software, (https://software.broadinstitute.org/morpheus). All antibodies used for mass cytometry are listed in Supplementary Table S1.

Total RNA sequencing

RNA-sequencing was performed in collaboration with the University of Michigan Sequencing Core. Total RNA was isolated from sorted tumor-infiltrating CD11b+ Gr-1+ cells using RNeasy Plus Mini Kit (Qiagen, 74134), and 100 ng samples of purified RNA were sent for analysis. RNA quality was assessed using a TapeStation (Agilent Technologies) following the manufacturer's recommended protocol. Samples with RINs (RNA Integrity Numbers) of 8 or greater were prepared using the Illumina TruSeq mRNA Sample Prep Kit v2 (Illumina, RS-122-2001, RS-122-2002). An amount of 0.1-3 μg of total RNA was converted to mRNA using polyA purification. The mRNA was then fragmented and copied into first-strand cDNA using reverse transcriptase and random primers. The 3' ends of the cDNA were then adenylated and ligated to adapters. Each ligated adapter had a unique 6 nucleotide barcode to identify each sample, enabling multiple samples to be sequenced from each lane of a HiSeq flow cell (Illumina). The products were purified and enriched by PCR to create the final cDNA library. Libraries were checked for quality and quantity by TapeStation (Agilent Technologies) and qPCR using Kapa's library quantification kit for Illumina Sequencing platforms (Kapa Biosystems, KK4835) using the manufacturer's recommended protocols. They were clustered on the cBot (Illumina) and sequenced 4 samples per lane on a 50-cycle single end on a HiSeq 4000 (Illumina) in High Output mode using version 4 reagents according to manufacturer's recommended protocols. Results were obtained from three biological replicates.

Total RNA sequencing analysis

All sequencing was performed by the University of Michigan DNA Sequencing Core, using the Illumina Hi-Seq 4000 platform. Fastq files were processed using the Tuxedo Suite for alignment and differential expression analysis. TopHat version 2.0.13 and Bowtie version 2.2.1 were used for alignment, based on the UCSC mm10 genome build. (105-107). Cufflinks/CuffDiff (version 2.1.1) were used for quantification and differential expression. Genes and transcripts were identified as differentially expressed based on three criteria: test status = "OK", FDR ≤ 0.05 and fold change $\geq \pm$ 1.5. Hierarchical clustering, using Ward's method, was implemented in R using the *cluster* package (version 2.0.5), and heatmaps were produced using the *gplots* package (version 3.0.1).

Gene Set Enrichment Analysis was done as previously described (108). Briefly, differentially expressed genes were ranked according to $\log_2$ (fold change). We then performed gene set enrichment analysis (GSEA) using this fold-change ranking. We downloaded the gmt file of all GO sets from the broad institute website (http://software.broadinstitute.org/gsea/index.jsp) and used it for GSEA analysis. Then, we used the Cytoscape enrichment map plugin and the rank and gmt files along with the positive/negative GSEA report files set to a nominal $p < 0.05$ and false discovery rate (FDR) at 0.5 to view enriched GO groups with $P < 0.05$.

$p < 0.05$ and false discovery rate (FDR) at 0.5 to view enriched GO groups with $P < 0.05$.

T cell proliferation assays

Granulocytes were purified from freshly isolated brain or spleen at symptomatic of wtIDH1 and mIDH1 tumor-bearing mice by flow sorting using the specific markers $CD45^+$, $CD11b^+$ and $Ly6G^+$. The inhibitory potential of these cells was assessed by co-culturing with Carboxyfluorescein succinimidyl ester (CFSE, Fisher scientific) labeled total splenocytes from *Rag2* Knockout/Transgenic OT-I T cell receptor mice (Taconic) at various ratios. The procedure is as follow: OT-1 *Rag2* knockout mouse was euthanized by injecting intraperitoneally (i.p.) 400 μL of anesthetics containing Ketamine (75 mg/Kg, Pfizer, NY) and dexmedetomidine (1 mg/kg). Spleen was carefully dissected, mashed through 70μm strainer using the plunger end of a syringe, and washed with 20 ml of Roswell Park Memorial Institute (RPMI, Gibco) media supplemented with 10% FBS, 100 unit/mL penicillin, and 55 μM 2-mercaptoethanol. Isolated cells were centrifuged 500 × *g* for 5 min, RBCs were lysed by adding 2 ml of RBC lysis buffer (Biolegend) and cells were incubated at 4 °C for 2 min. Lysis buffer was neutralized, and cells were washed 2x with DPBS (Gibco). Finally, OT-1 cells were counted, checked for viability, and resuspended in DPBS (Gibco) at a concentration of 1.0×10^6 cells/mL Cells were then labeled with CFSE by adding 1ml of freshly prepared CSFE solution (5 μM) to obtain a final concentration of 2.5 μM, and cells were incubated for 5 min at 37 °C with occasional shaking. The labeling was quenched by adding 2 mL of pure FBS (Gibco), splenocytes were washed 2x with RPMI, counted, and plated at a concentration of 100,000 cells/ 50 μL. Tumor-infiltrating granulocytes were sorted from percoll™ purified immune cells as described in the flow cytometry section. Cells were first labeled with viability dye (Alexa Fluor 780) to label dead cells, and granulocytes were FACS sorted using the following antibodies CD45, CD11b, and Ly6G. Purified granulocytes were counted and diluted to 100,000 cells/50 μl in RPMI media containing 2-mercaptoethanol and were added to the cultured OT-1 splenocytes

in the following ratios (1:1, 1:2, and 1:4). Finally, 100µl of 200 nM SIINFEKL peptide (AnaSpec Inc.) were added to the mixture to stimulate the OT-1 splenocytes proliferation for 4 days (52,99). After 4 days, cells were stained with anti-mouse CD3 and CD8 antibodies (listed in Supplementary Table S2) diluted in BD FACS Flow Sheath Fluid and T-cell proliferation was analyzed by CFSE dye dilution. In condition where SIINFEKL was not added, all cells were at resting state (100% resting T-cells, 0% proliferating T-cells). In all conditions where SIINFEKL was added, the percentage of proliferating T cells were determined as [(Fluorescence intensity of proliferating cells/Fluorescence intensity of the resting T-cells) X 100] (52).

Single cell-RNA sequencing

Tumors from SB mice harboring either wtIDH1 or mIDH1 were harvested and kept in Roswell Park Memorial Institute media (RPMI, Gibco, NH). They were cut into small pieces (1 mm^3). The whole solution containing the tumor pieces was then transferred into a 50 ml tube and centrifuged at 1500 RPMI for 5 minutes. Using large pore pipette tips, the pellet was re-suspended in 1ml StemPro Accutase® cell dissociation reagent (Gibco, NH) and incubated for 5-10 min at 37°C (all tumor pieces are dissociated at that point). The Accutase® was neutralized with 9 mL RPMI media and mixed by pipetting. Cells were then passed through 70 µm strainer (Alkali Inc.,) attached to a 50 mL conical tube, and centrifuged at 1500 RPM for 5 minutes. Debris and dead cells were removed using the dead cells removal column (Miltenyi Biotec). After that, cells were washed twice with PBS, counted, and resuspended at a concentration of 1000 cells/µL. The cell viability was determined by Countess automated cell counter, and it was > 90%.

For human samples, freshly isolated primary tumor tissue was kept in DMEM/F12 media (Gibco). Tissue was cut into small pieces until a homogenous solution is obtained. Cells were dissociated using StemPro Accutase® cell dissociation reagent (Gibco) in two-cycle 5 min each until single-cell suspension was obtained. The cell suspension was passed through 70 µm strainer to remove debris and connective tissue, lysed with RBC's lysis buffer (Biolegend), and passed through dead cells removal column (Miltenyi Biotec). A yield of at least > 90% live cells was considered adequate for single-cell RNA-sequencing.

Single cell suspensions were subjected to final cell counting on the Countess II Automated Cell Counter (ThermoFisher) and diluted to a concentration of 700 -1000 cells/ul. 3' single cell libraries were generated using the 10X Genomics Chromium Controller and following the manufacturer's protocol for 3' V3.1 chemistry with NextGEM Chip G reagents (10X Genomics). Final library quality was assessed using the Tapestation 4200 (Agilent) and libraries were quantified by Kapa qPCR (Roche). Pooled libraries were subjected to 150 bp paired-end sequencing according to the manufacturer's protocol (Illumina NovaSeq 6000). Bcl2fastq2 Conversion Software (Illumina) was used to generate de-multiplexed Fastq files and CellRanger Pipeline (10X Genomics) was used to align reads and generate count matrices. Two biological replicates for each condition (*wtIDH1* and *mIDH1*) were analyzed. An average sequencing depth of 20,000 reads/cell was recovered for each sample we processed.

Single-cell RNA sequencing analysis

Raw sequencing data files were converted to fastq files and aligned to the mouse/human reference genome (mm10 and hg38, respectively) [http://cf.10xgenomics.com/supp/cell-exp/refdata-cellranger-mm10-3.1.0.tar.gz] using the Cell Ranger Pipeline version 3.1.0. Filtered

digital gene expression matrix files (DGE) containing the number of unique molecular identifiers (UMI) counts per gene per cell were analyzed using the Seurat R package version 3.1.4. Matrix files were loaded using the Seurat *Read10X* function, and Seurat objects created retaining cells with a default minimum of 300 features (genes) and retaining features present in at least three cells. We merged DGE matrices from samples belonging to each condition (*wtIDH1* or *mIDH1*), yielding two DGE matrices. Possible doublet cells with more than 3000 unique expressed genes, or cells with more than 10% mitochondrial genome content, were filtered. Size normalization (natural-log transformed) for each cell was performed using the Seurat *NormalizeData* function with the default scale factor of 10,000. Feature selection was performed using *FindVariableFeatures* ('vst' selection method) to identify 4000 highly variable features in each condition. Next, *ScaleData* was used to center the expression vectors and scale the mean and variance of each feature across cells. We then performed unsupervised clustering analysis following the procedure described in the Seurat3 package. First, the high-dimensional expression space was reduced using PCA. The number of informative components of each dataset was inferred from a jackstraw plot of each principal component. The component space was utilized to construct a neighborhood graph of cells using the *FindNeighbors* function with the default k of 20, followed by the Seurat Louvain-based *FindClusters* method with a resolution of 0.4 (109). Cell clusters were embedded in 2D and visualized using the *RunUMAP* or *RunTSNE* function. Cluster-specific genes were obtained using the function *FindAllMarkers*. Clusters were annotated based on the feature markers expressed in each cluster.

For data integration, data from *wtIDH1* and *mIDH1* were processed and normalized as described above. We then identified anchors in each dataset—cells with common expression profiles—

using the *FindIntegrationAnchors* function with the following settings: dims = 1:30, k.anchor = 5, k.filter = 200, k.score = 30, and anchor.features = 2000. The two datasets were then integrated into a single Seurat object using the *IntegrateData* function. The integrated data were then scaled and PCA ran as described above. Finally, after switching to the 'RNA' assay in Seurat, we ran *FindConservedMarkers* to identify 50 cell type marker genes that are conserved across conditions.

For human samples, we merged DGE matrices from samples belonging to each condition (*wtIDH1* or *mIDH1*), filtered, normalized, and scaled data as described above. We then used the function *AddModuleScore* to obtain a score for each cluster of the following PMN-MDSCs gene signature (*S100A8, S100A9, TGFβ, Arg2, IL1β*) across the combined samples. A positive number indicates that the selection of genes is expressed higher in a (cluster/cell) than the expected average expression. PMN-MDSCs cellular fraction was determined by dividing the total number of cells with positive scores by the total immune cells (cells expressing *PTPRC*).

MDSCs and glioma neurospheres Co-culture system

Bone marrow (BM) cells were obtained from the femur and tibia of wild type mice as described in the flow cytometry section (see above). First, a C57/Bl6 mouse was euthanized by injecting intraperitoneally (i.p.) 400 µL of anesthetics containing Ketamine (75 mg/Kg, Pfizer, NY) and dexmedetomidine (1 mg/kg). Bone marrow cells were extracted by flushing freshly isolated tibia and femur with DMEM+10% FBS using a syringe with a 30G needle until the bone is clear. Cells were then centrifuged, and RBCs were lysed using 2 ml RBC lysis buffer (90 sec at 4°C) after which they were washed with DPBS, counted and seeded at 2 x 10^5 cells per well in a 48

well plate and 0.2 mL media (RPMI + 10% FCS + Pen/Strep + β-mercaptoethanol). Neurospheres from *wtIDH1*, or *mIDH1* were added in a ratio of 2:1 (BM cells: neurospheres). Cells were supplemented with 100 µL of culture media every other day to maintain cell viability. Cultures were maintained for 7 days after which they were stained with CD45, CD11b, Ly6G, iNOS, Arg1, PD-L1, and CD80. The procedure for antibody staining and gating is the same as described in the flow cytometry section.

α-GCSF neutralization

Mice were injected i.p. with five doses (100 µg each dose diluted in PBS) of α-GCSF (R&D system; Clone: 67604) or isotype every 4-5 days after tumor implantation. Blood was collected from animals one day after α-GCSF treatment, and serum level of G-CSF was quantified by quantitative ELISA (see details below).

Quantitative ELISA

Conditioned media from mouse neurospheres and from human glioma cells (*wtIDH1*-SJGBM2 or *mIDH1*-SJGBM2) were harvested after culturing of 2 x 10^5 cells/ 1mL for 48 hours in appropriate neurospheres culture media (IMDM medium with L-glutamine (0.3 mg/mL), 20% FBS, and antibiotic-antimycotic (1X)). Quantitation of G-CSF was determined by ELISA (Duosets, R&D Systems, Minneapolis, MN) using the manufacturer's suggested protocol with few modifications. Briefly, diluted coating Ab was added to ELISA microplates (Greiner Bio-One, Monroe, NC) and incubated overnight. Assay plates were then washed, blocked, and samples & standards added and incubated overnight @ 4C. Diluted secondary Ab was added after washing and incubated for 3 hours at room temperature, followed by washing and HRP

incubation for 90 minutes. Following a final series of washes, plates were developed with TMBX substrate (Surmodics, Eden Prairie, MN), and stopped by the addition of an equal volume of 0.4% NaF. Absorbances were obtained @ 620 nm and sample concentrations determined by comparison to the G-CSF standards using a 4-parameter curve fit (Synergy HT & Gen5 Software, BioTek Instruments, Winooski, VT)

Cytokine array

Proteome Profiler Mouse Cytokine Array Kit, Panel A (R&D Systems) was used to analyze cytokine secretion from the conditioned media of tumor derived-neurospheres according to the manufacturer instructions. Total 1 x 10^6 neurospheres were cultures in 1 mL of media for 24 hrs. The conditioned media from this culture was collected, diluted with 0.5 mL of DMEM/F12 media, and incubated with pre-activated membranes according to the manufacturer protocol. The membranes were washed 2X with washing buffer (R and D, ARY006) before they were incubated with HRP conjugated antibodies mix. The spot pixel area for each cytokine was calculated using Image Lab software (Bio-rad) and was subtracted from the pixel intensity of the background spot pixel (generated by measuring the pixel intensity of the negative control). Each cytokine was analyzed in duplicate, and the average intensity was blotted.

Real-Time Quantitative Polymerase Chain Reaction (RT-qPCR)

Two-step QRT-PCR was performed following the manufacturer's instructions. Total RNA was isolated using the RNeasy Plus Mini Kit (Qiagen) and 2 μg RNA was reverse transcribed to complementary DNA with the AffinityScript QPCR cDNA Synthesis Kit (Agilent Technologies). Quantitative real-time PCR (QPCR) analysis was performed using the Fast

SYBR™ Green Master Mix (Thermo-Fisher Scientific) in a ViiA™ 7 Real-Time PCR System (Thermo-Fisher Scientific). Mouse Csf3 mRNA was amplified using primers 5′-ATCCCGAAGGCTTCCCTGAGTG-3′ and 5′-AGGAGACCTTGGTAGAGGCAGA-3′, and mouse Tbp mRNA was amplified using primers 5′-ACCCTTCACCAATGACTCCTATG-3′ and 5′-ATGATGACTGCAGCAAATCGC-3′. The relative expression level of Csf3 mRNA was calculated using the $2^{-\Delta\Delta Ct}$ method, normalized to the housekeeping gene: TATA-Box Binding Protein (*Tbp*). The qPCRs were performed in three biological triplicates.

ChIP-seq

ChIP-seq data from *Nunez et al. 2019* was used to examine epigenetic enrichment of G-CSF in neurospheres from *wtIDH1* or *mIDH1* (NCBI's Gene Expression Omnibus with identifier GSE99806)(46). Immunoprecipitation, quality control, read alignment, and peak annotation were performed as described before (46).

Data and Material availability

All data associated with this study are in the figure and/or the Supplementary Materials. The RNA-seq and sc-RNA-seq datasets have been deposited in NCBI's Gene Expression Omnibus with identifiers GSE152277. The materials generated in this study will be provided upon request to M.G.C.; all plasmids described in this study have been deposited in Addgene (Supplementary Table S6).

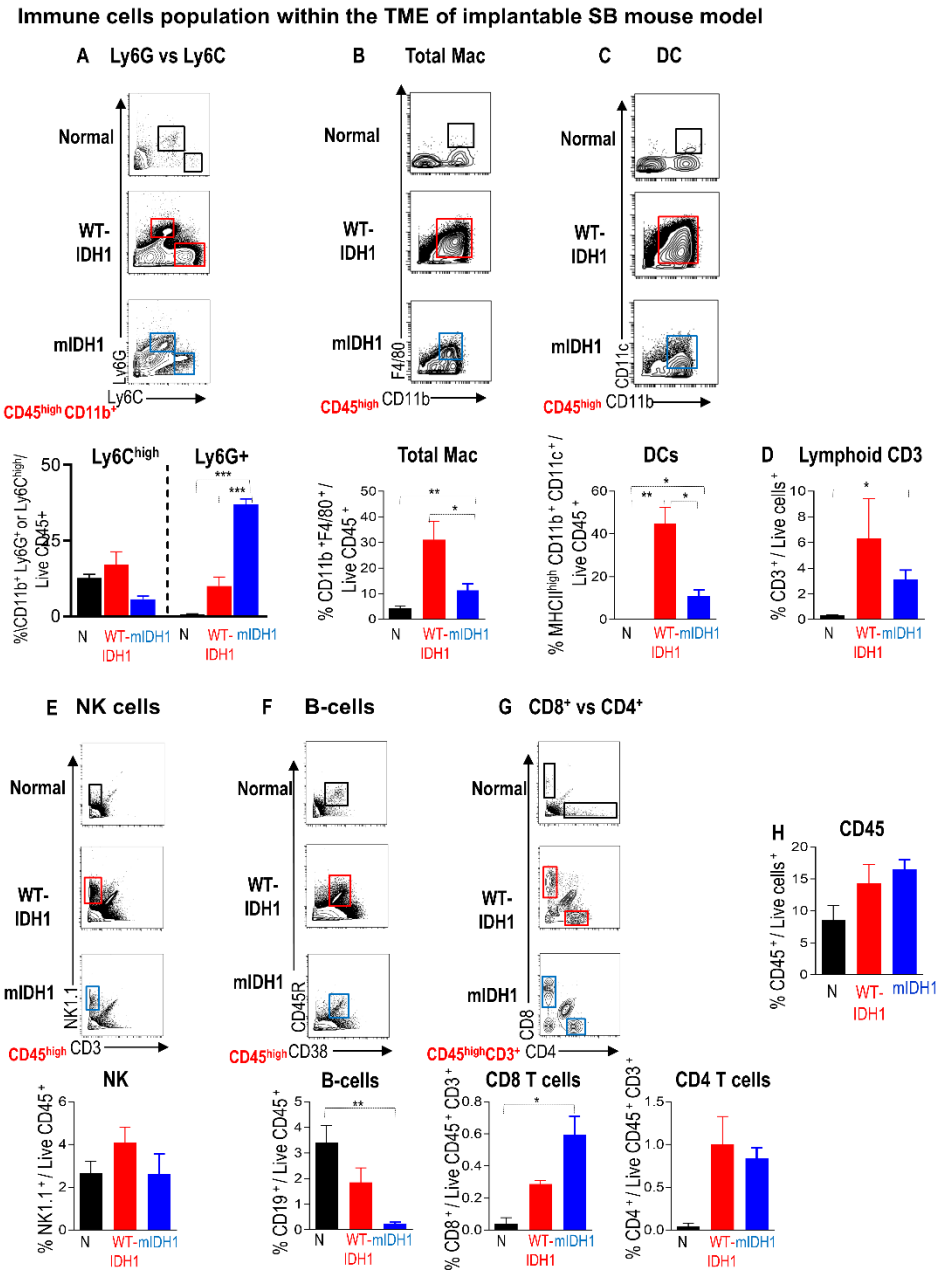

Supplementary Figure S1. Characterization of infiltrating immune cells in normal (N), SB induced *wtIDH1*, or SB induced *mIDH1* tumors. Mass cytometry analysis of the percentage of **(A)** Natural killer (NK1.1^{+}), **(B)** B-cells (CD19^{+} CD38^{+}), **(C)** Naïve CD8^{+}, CD4^{+} cells and activated T-cells (gated from CD45^{+}CD3^{+}), **(D)** Lymphoid CD3^{+} population, **(E)** Total macrophages (CD11b^{+} F4/80^{+}), **(F)** Granulocytic (Ly6G^{+}) vs monocytic (Ly6C^{+}) MDSCs (gated from CD45^{+} CD11b^{+}), **(G)** Conventional DC (CD11b^{+} CD11c^{+} MHCII^{+}), and **(H)** Total frequency of CD45^{+}. Frequency was calculated as a percentage of live CD45^{+} unless otherwise indicated. (N=3-5 animals) * *P<0.05,* ** *P<0.01,* *** *P<0.005.* One-way ANOVA

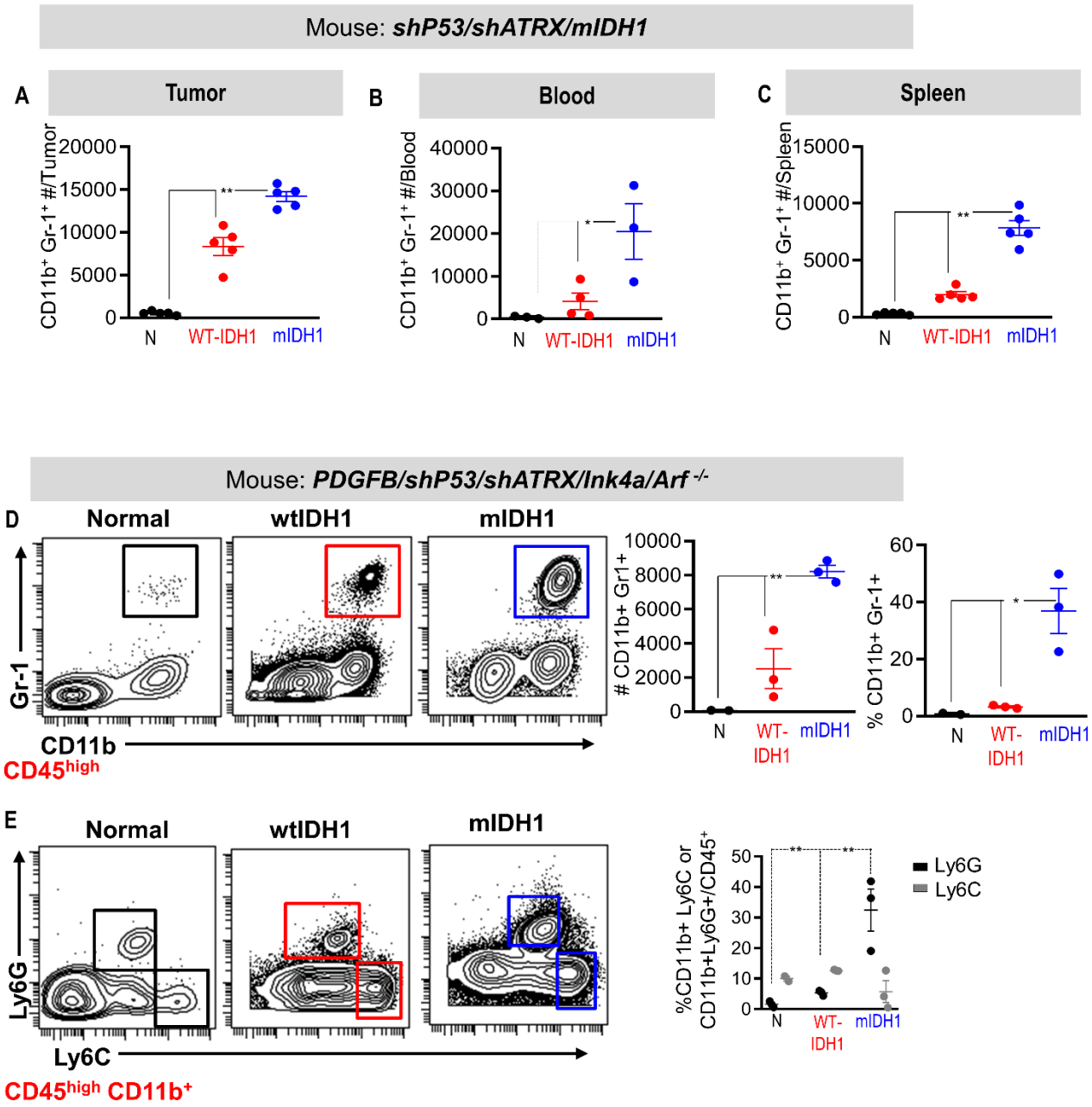

Supplementary Figure S2. Flow cytometry analysis of CD11b$^+$/Gr-1$^+$ counts in **(A)** tumor, **(B)** blood, and **(C)** spleen of naive mice, and mice implanted with *wtIDH1* or *mIDH1* neurospheres developed using the sleeping beauty system. **(D)** Flow cytometry analysis of CD11b$^+$ Gr-1$^+$ cell frequency in normal mice, mice implanted with *wtIDH1* or *mIDH1* neurospheres developed using the RCAS system. *mIDH1* group showed a higher frequency of CD11b$^+$ Gr-1$^+$ compared to the *wtIDH1* and normal mice. **(E)** MDSC phenotypic characterization in normal mice, mice implanted with *wtIDH1* or *mIDH1* neurospheres developed using the RCAS system. The expanded CD11b$^+$ Gr-1$^+$ in *mIDH1* were mainly Ly6G$^+$ cells. * *P<0.05,* ** *P<0.01,* *** *P<0.005.* One-way ANOVA

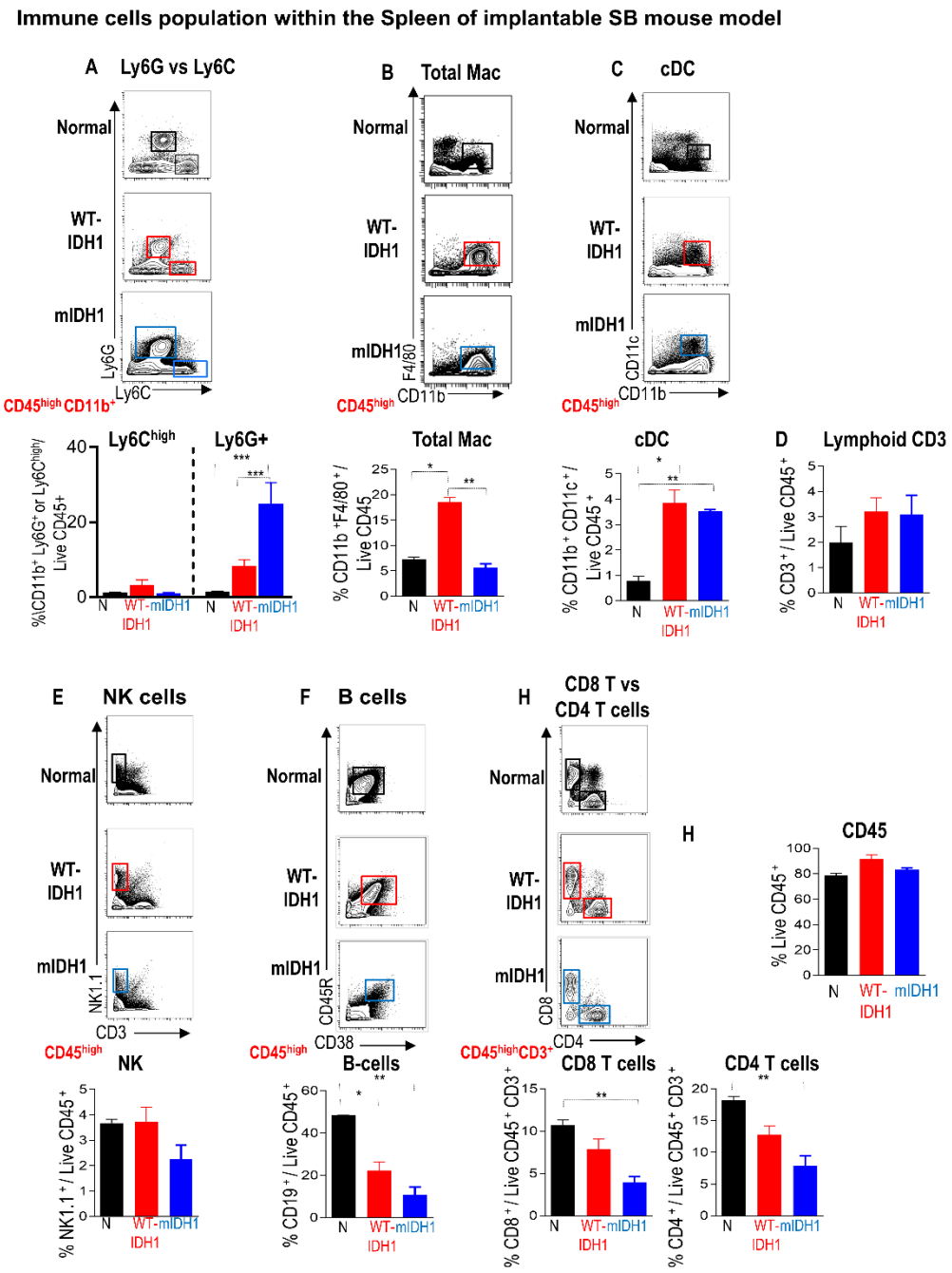

Supplementary Figure S3. Immune cell characterization of spleen from normal (N), SB induced *wtIDH1*, or SB induced *mIDH1* tumor. Mass cytometry analysis of the percentage of **(A)** Natural killer (NK1.1^{+}), **(B)** B-cells (CD19^{+} CD38^{+}), **(C)** Naïve CD8^{+}, CD4^{+} cells and activated T-cells (gated from CD45^{+}CD3^{+}), **(D)** Lymphoid CD3^{+} population, **(E)** Total macrophages (CD11b^{+} F4/80^{+}), **(F)** Granulocytic (Ly6G^{+}) vs monocytic (Ly6C^{+}) MDSCs (gated from CD45^{+} CD11b^{+}), **(G)** Conventional DC (CD11b^{+} CD11c^{+} MHCII^{+}), and **(H)** Total frequency of CD45^{+}. Frequency was calculated as a percentage of live CD45^{+} unless otherwise indicated. (N=3-5 animals) * *P<0.05,* ** *P<0.01,* *** *P<0.005.* One-way ANOVA

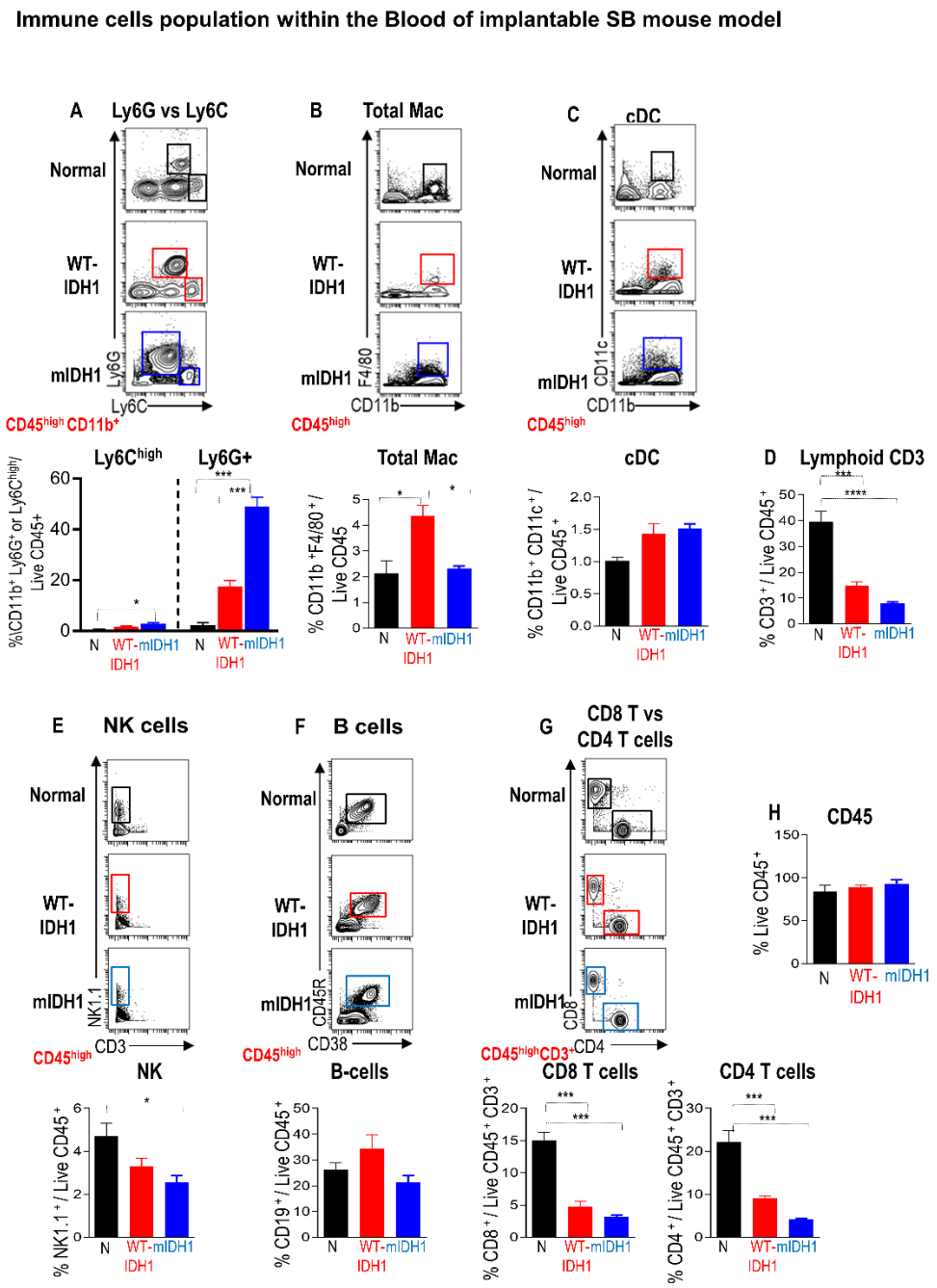

Supplementary Figure S4. Immune cells characterization of blood from normal (N), SB induced *wtIDH1*, or SB induced *mIDH1* tumor. Mass cytometry analysis of the percentage of **(A)** Natural killer (NK1.1^{+}), **(B)** B-cells (CD19^{+} CD38^{+}), **(C)** Naïve CD8^{+}, CD4^{+} cells and activated T-cells (gated from CD45^{+}CD3^{+}), **(D)** Lymphoid CD3^{+} population, **(E)** Total macrophages (CD11b^{+} F4/80^{+}), **(F)** Granulocytic (Ly6G^{+}) vs monocytic (Ly6C^{+}) MDSCs (gated from CD45^{+} CD11b^{+}), **(G)** Conventional DC (CD11b^{+} CD11c^{+} MHCII^{+}), and **(H)** Total frequency of CD45^{+}. Frequency was calculated as a percentage of live CD45^{+} unless otherwise indicated. (N=3-5 animals) * *P<0.05,* ** *P<0.01,* *** *P<0.005*. One-way ANOVA

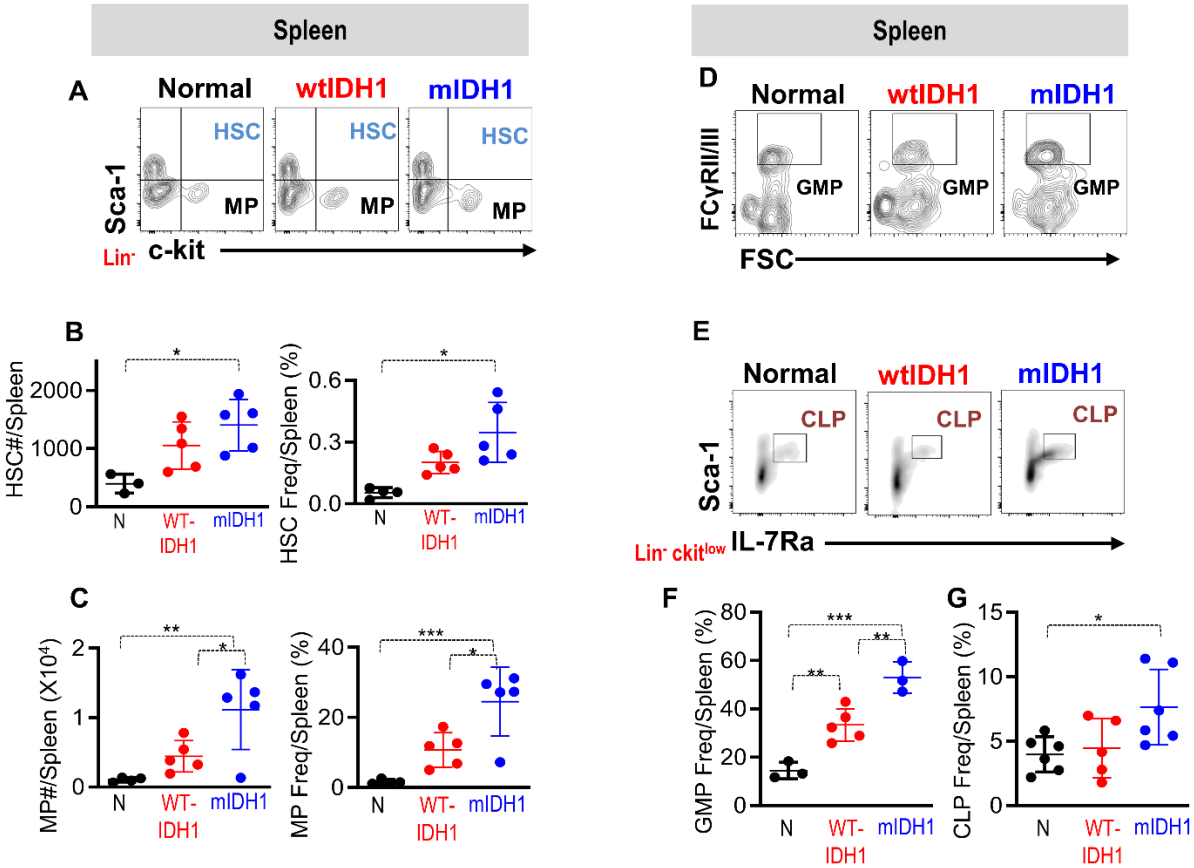

Supplementary Figure S5. *mIDH1* glioma development results in profound alteration in hematopoiesis. (A) Representative flow cytometry plots showing the percentage of HSCs and MPs in spleen from *wtIDH1* or *mIDH1* tumor-bearing animals. **(B, C)** Quantification of the absolute number and frequency of **(B)** HSCs and **(C)** MPs in the spleen of tumor-bearing animals at the symptomatic stage. Mice with *mIDH1* tumors have a higher number and frequency of MPs. **(D, E)** Representative flow cytometry plot showing the frequency of common lymphoid progenitors CLPs and GMPs in spleens from *wtIDH1* and *mIDH1* tumor-bearing animals. **(F, G)** Flow cytometry analysis of the frequency of **(F)** GMPs and **(G)** CLPs in the spleen from *wtIDH1* or *mIDH1* tumor-bearing animals. *mIDH1* tumor-bearing mice had a higher frequency of GMPs but not CLPs in the spleen compared to the *wtIDH1* group.

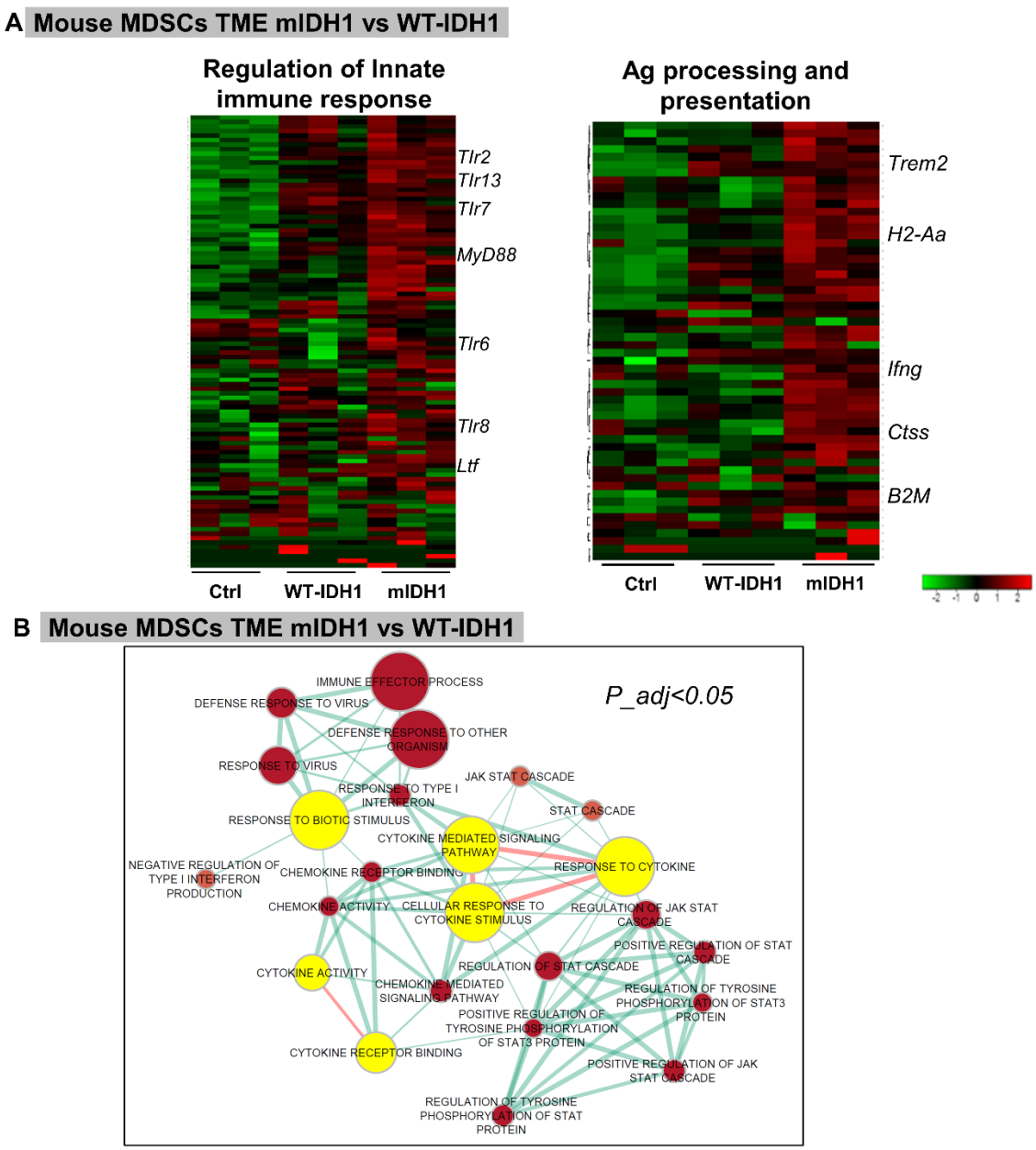

Supplementary Figure S6. Granulocytes from *mIDH1* tumors are enriched in immune regulation gene sets. (A) Heat maps showing the expression level of genes belonging to antigen processing and presentation and regulation of innate immunity gene sets in granulocytes from Ctrl (*NRAS, TP53*), *mIDH1*, and *wtIDH1* TMEs. **(B)** Enrichment map visualization for the differentially expressed genes shows the upregulated gene sets (red) in granulocytes from *mIDH1* TME compared to granulocytes from *wtIDH1* tumor. Highlighted groups (yellow) belong to pathways affected by the granulocytes differentiation pathway. Node size corresponds to the size of the gene set. Enriched gene sets are shown at FDR= 0.1.

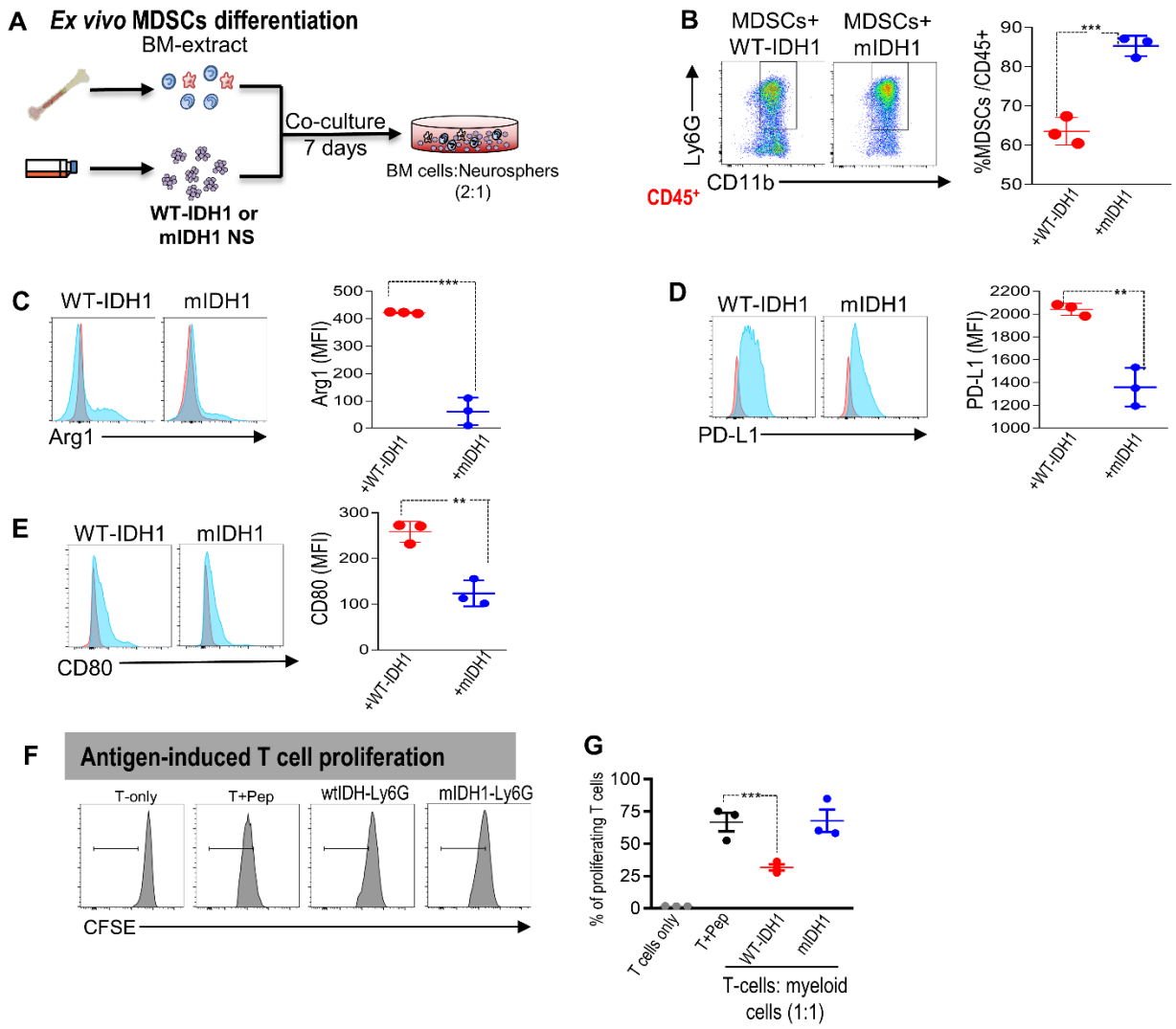

Supplementary Figure S7. Granulocytes derived from *ex vivo* co-culture with *mIDH1* neurospheres are not inhibitory. (A) Schematic figure of the *ex vivo* differentiation assay using the neurospheres co-culturing system. **(B)** $CD11b^+$ $Ly6G^+$ characterization after co-culturing with *wtIDH1*, or *mIDH1* neurospheres for 7 days. Expression of **(C)** Arg1, **(D)** PD-L1, (E) CD80 on BM-derived $CD11b^+$ $Ly6G^+$ cells after co-culturing with *wtIDH1*, or *mIDH1* neurospheres. $CD11b^+$ $Ly6G^+$ cells from *mIDH1* co-culture express a lower level of inhibitory markers. **(F, G)** T-cell proliferation assay to assess the inhibitory potential of *ex vivo* derived PMN-MDSCs. BM-derived $CD11b^+$ $Ly6G^+$ cells from *mIDH1* neurospheres co-culture do not inhibit T-cell proliferation. * $P<0.05$, ** $P<0.01$, *** $P<0.005$. One-way ANOVA

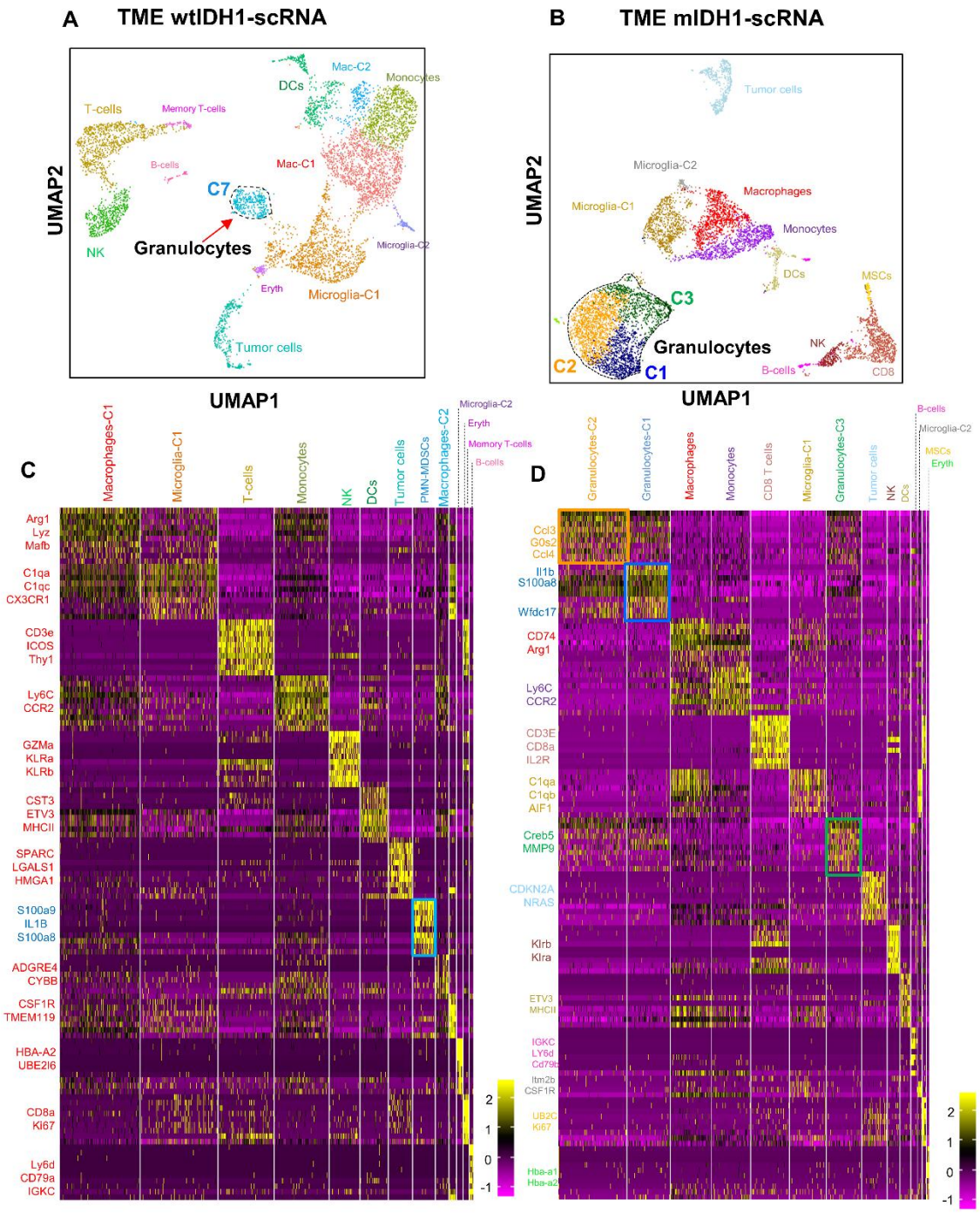

Supplementary Figure S8. Single-cell sequencing analysis of immune cells isolated from TME of SB induced *wtIDH1* or *mIDH1* tumors. (A, B) Combined Seurat analysis of immune cells from the TME of *wtIDH1* and *mIDH1* tumors results in various distinct lusters. Granulocytes were identified in one cluster (C7) in the *wtIDH1*, whereas the *mIDH1* granulocytic population was composed of three granulocytic clusters (C1, C2, C3), (N=2). **(C, D)** Heat map showing the top 10 differentially expressed genes in each cell cluster within **(C)** *wtIDH1* or **(D)** *mIDH1* tumor samples.

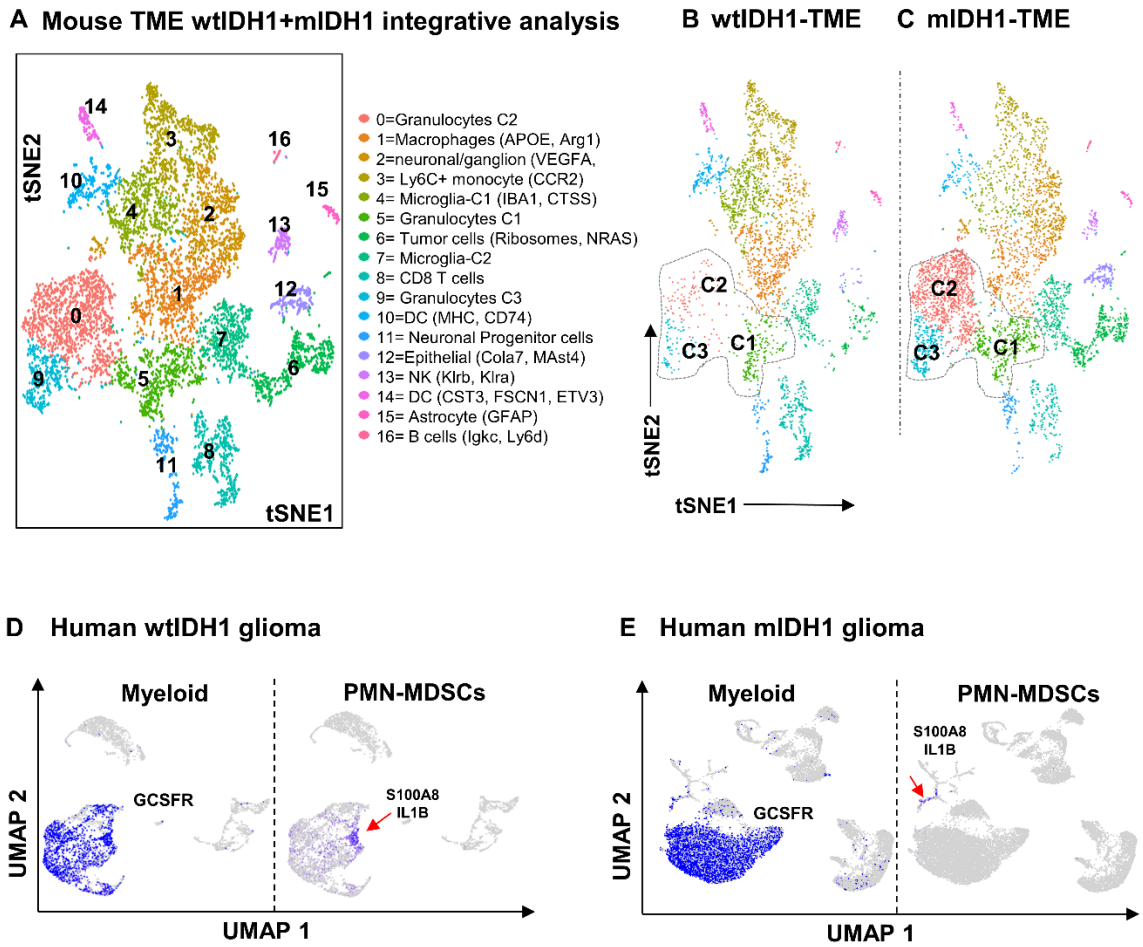

Supplementary Figure S9. Granulocytes infiltrating the *wtIDH1* tumors are similar to C1 granulocytes infiltrating the *mIDH1* tumors. (A) Seurat integrative analysis of immune cells from TME of *wtIDH1* and *mIDH1* genetically engineered mouse tumors results in various distinct clusters of TME CD45^{+} cells. **(B, C)** Split view of Seurat integrative analysis of immune cells isolated from *wtIDH1* **(B)** and *mIDH1* **(C)** tumors. The majority of granulocytes from *wtIDH1* are clustered with C1 in the *mIDH1*. **(D)** Feature plots represent the expression of the granulocyte receptor *CSF3R* gene (left) and genes related to PMN-MDSCs signature (*IL1β, S100A8, S100A9, Arg1, TGFβ1*) (right). Low gene expression is shown in grey and high expression in dark blue in *wtIDH1*. **(E)** Feature plots represent the expression of the granulocyte receptor *CSF3R* (left) and genes related to PMN-MDSCs signature (*IL1β, S100A8, S100A9, ARG1, TGFβ1*) (right) with low expression in grey to high expression in dark blue in *mIDH1*.

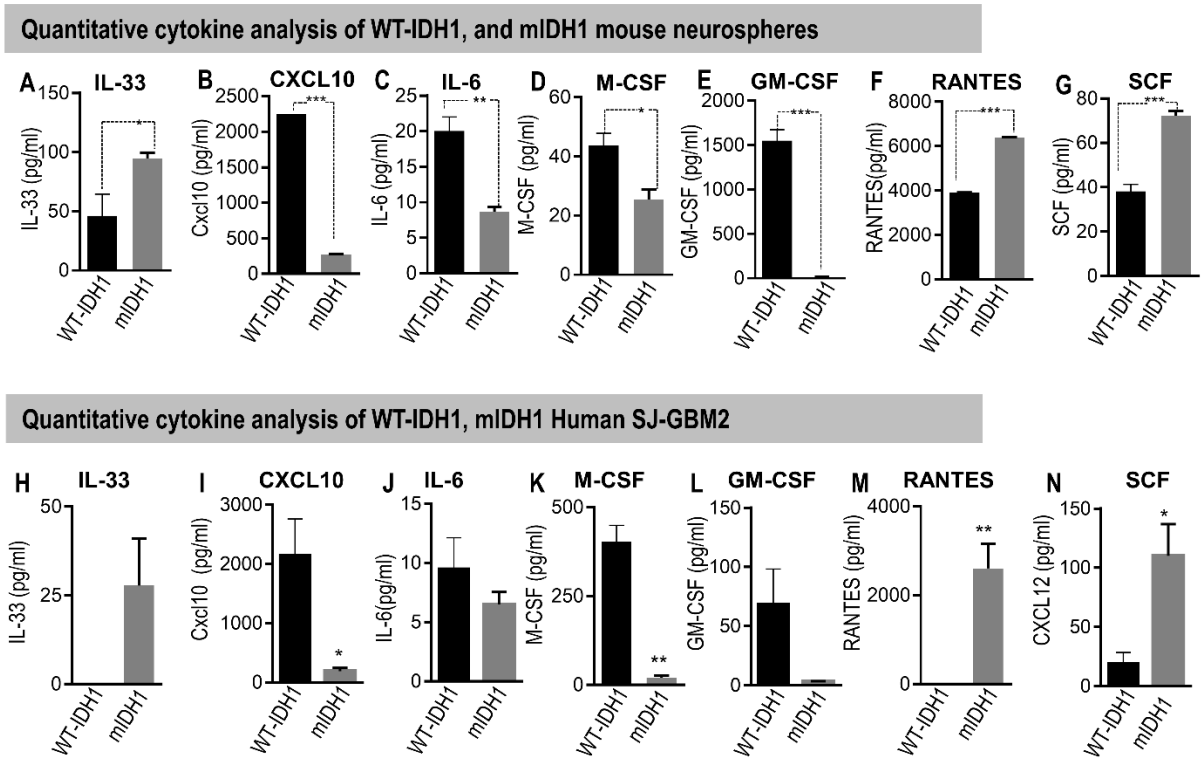

Supplementary Figure S10. Quantitative ELISA analysis of cytokines from conditioned media of cultured *wtIDH1* and *mIDH1* neurospheres. (A-G) Quantitative ELISA analysis of the differentially secreted cytokines and chemokines in CM of cultures mouse *wtIDH1*, and *mIDH1* neurospheres. **(H-N)** Quantitative ELISA analysis of the differentially secreted cytokines and chemokines from CM of SJ-GBM *wtIDH1* and SJ-GBM *mIDH1* cell cultures. * *P<0.05,* ** *P<0.01,* *** *P<0.005.* One-way ANOVA

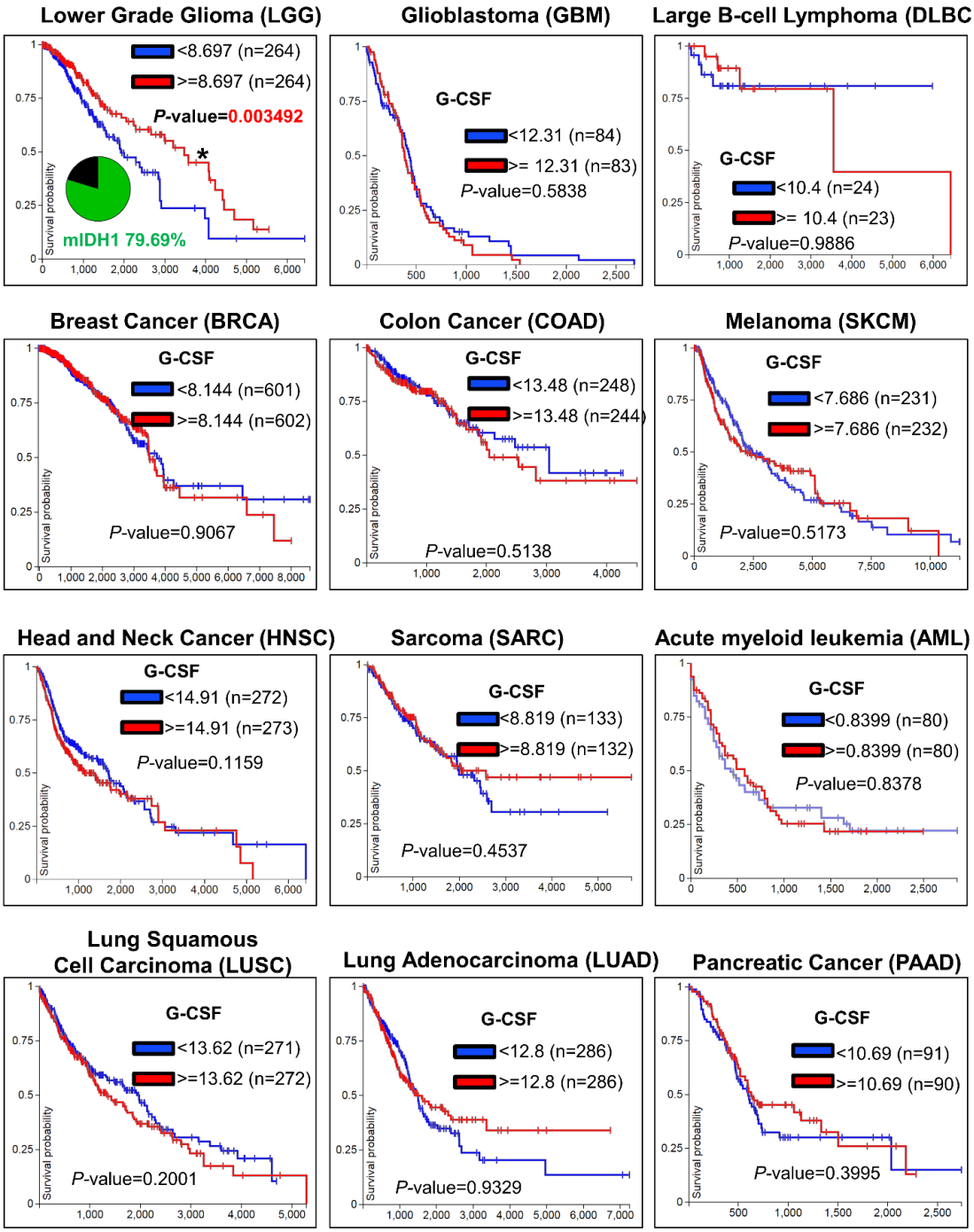

Supplementary Figure S11. Kaplan-Meier survival analysis of the different types of tumors in the TCGA data according to *CSF3* expression (high vs low). LGG is the sole tumor within the TCGA database in which patients who express a high level of *CSF3* have a favorable prognosis compared to patients with low *CSF3* expression. * *P<0.05,* ** *P<0.01,* *** *P<0.005*

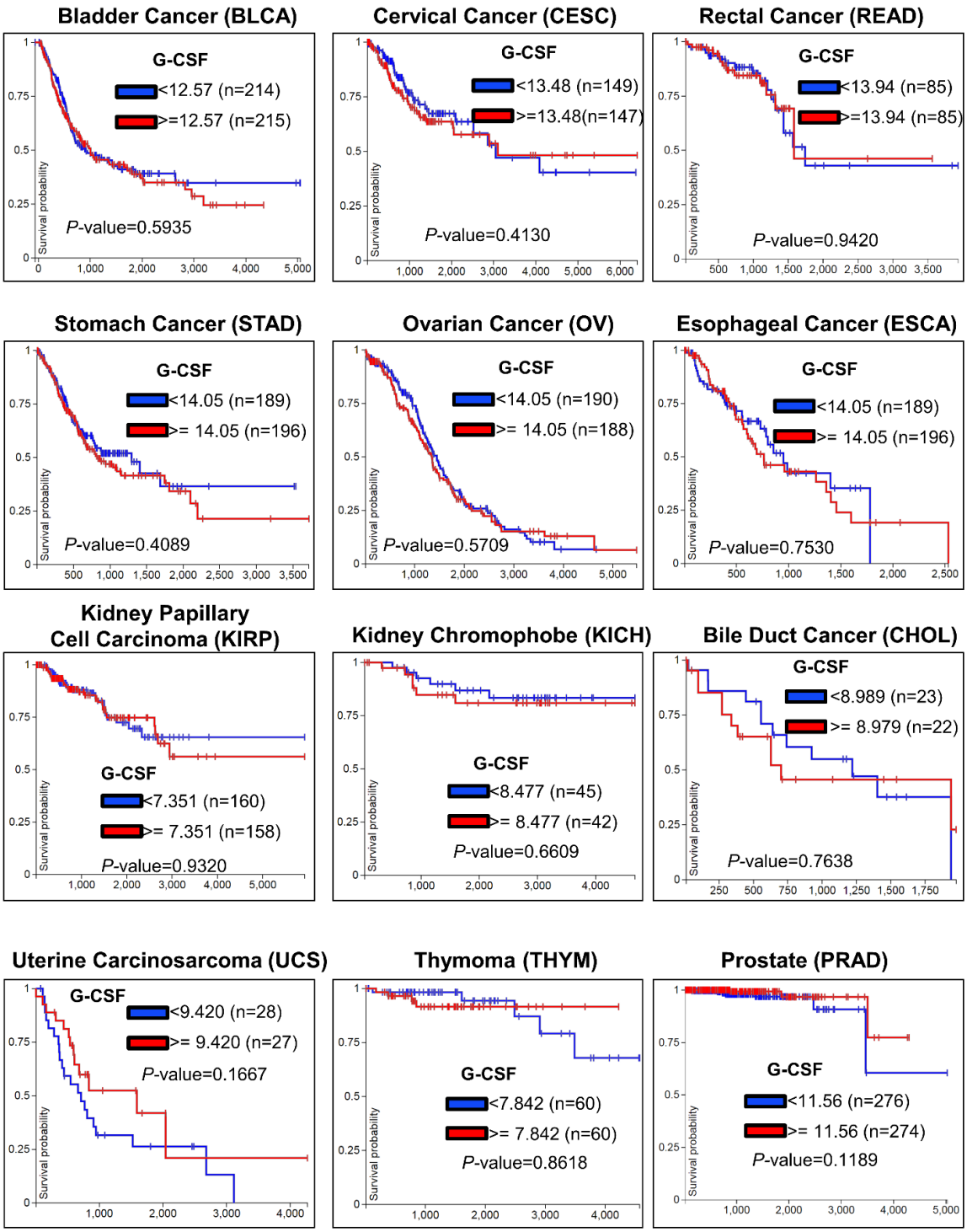

Supplementary Figure S11 (Cont.). Kaplan-Meier survival analysis of the different types of tumors in the TCGA data according to *CSF3* expression (high vs low). LGG is the sole tumor within the TCGA database in which patients who express a high level of *CSF3* have a favorable prognosis compared to patients with low *CSF3* expression. * *P<0.05,* ** *P<0.01,* *** *P<0.005*

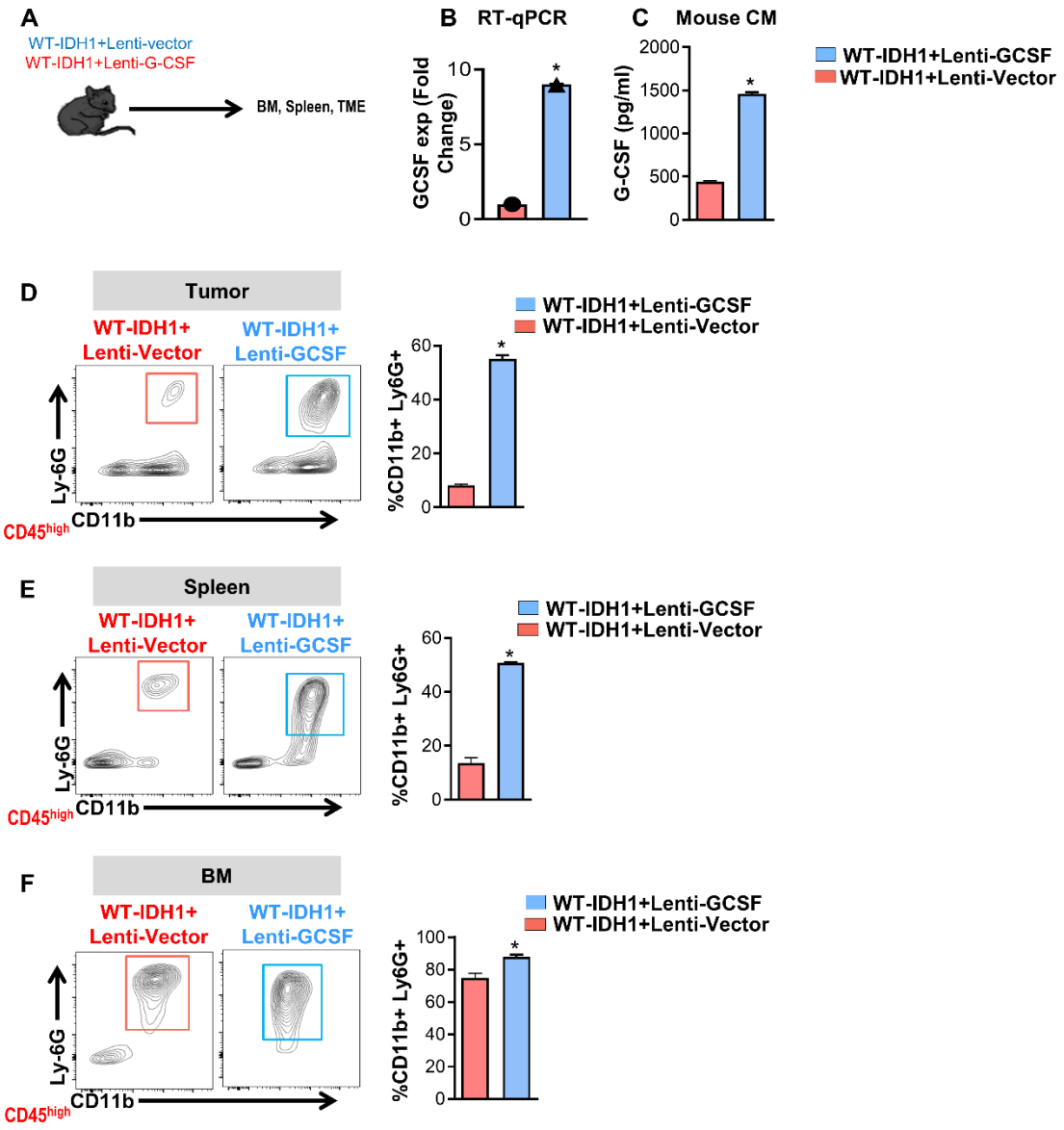

Supplementary Figure S12. G-CSF expressing neurospheres resulted in global expansion of granulocytes in *wtIDH1* tumor-bearing animals. (A) Schematic shows experimental design for implantation of G-CSF-expressing *wtIDH1* neurospheres using Lentivector. **(B)** RT-qPCR for *CSF3* in *wtIDH1* neurospheres transduced with lentivirus expressing empty vector (red) or with Lentivirus encoding for *CSF3*. **(C)** Quantitative ELISA measuring G-CSF secretion in conditioned media from cultured mouse neurospheres with *wtIDH1* transduced with the empty vector (red) or the lentivirus encoding *CSF3* (blue). Representative flow plots and flow analysis show the frequency of granulocytes in **(D)** Tumors, **(E)** Spleen, and **(F)** BM of implanted animals with *wtIDH1*+Lenti-vector or *wtIDH1*+Lenti-GCSF. Animals implanted with *wtIDH1*+Lenti-GCSF has an expansion of granulocytes in the tumor, spleen, and BM compared to *wtIDH1*+Lenti-vector. * *P<0.05,* Student t-test.

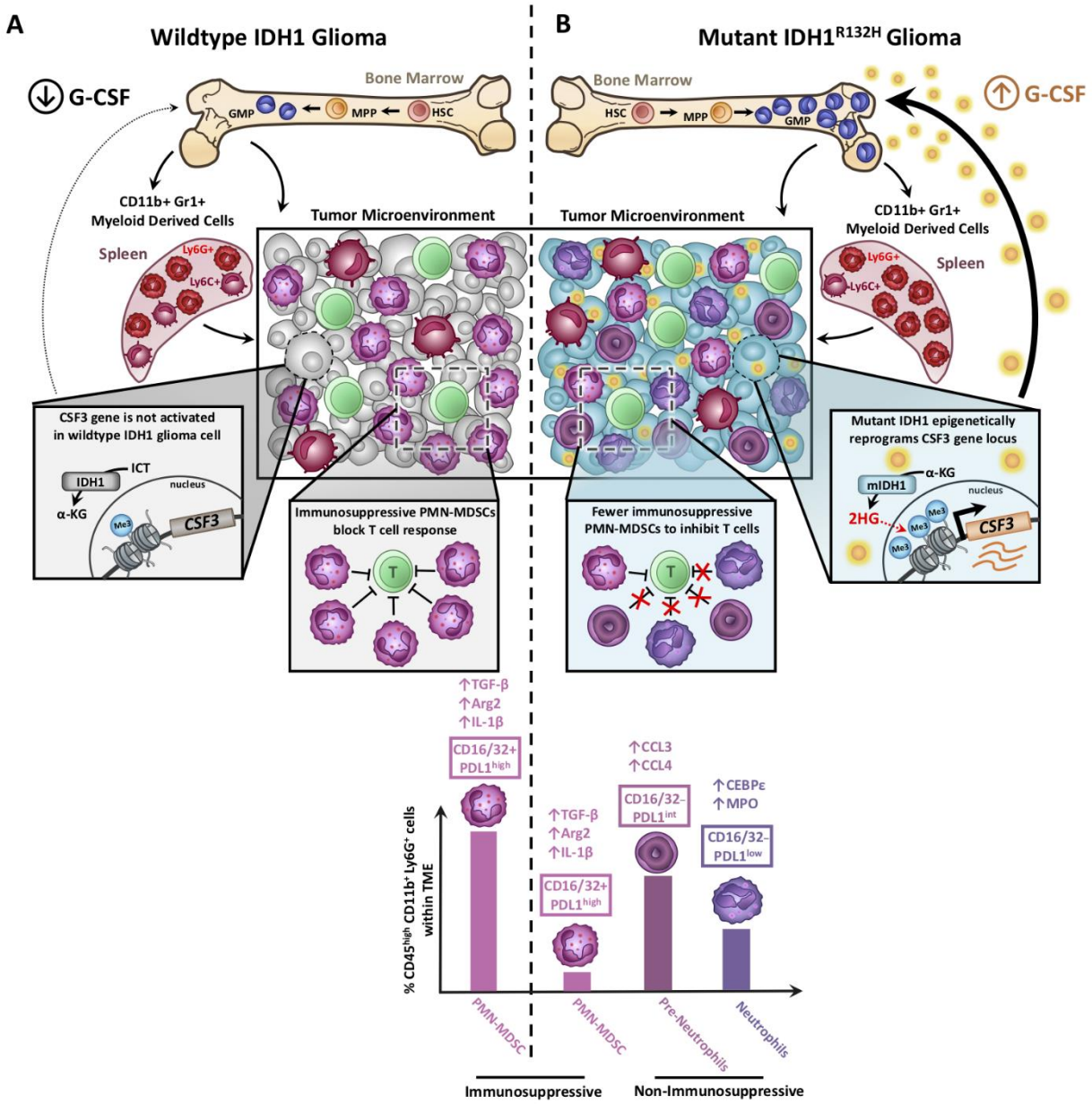

Supplementary Figure S13. Epigenetic reprogramming of granulocytes' differentiation in *mIDH1* glioma. (A) In wtIDH1 glioma, tumor cells express cytokines such as GM-CSF and IL-6 and low levels of G-CSF which affect hematopoiesis in the BM and spleen of glioma bearing animals to produce immunosuppressive granulocytic MDSCs (PMN-MDSCs: $CD45^{hi}$/PD-$L1^{high}$/$CD16/32^{+}$). **(B)** Through epigenetic reprogramming, *mIDH1* glioma stem-like cells express and secrete high levels of G-CSF. Circulating G-CSF impacts hematopoiesis in the BM and spleen, promoting the expansion, differentiation, and mobilization of granulocytic myeloid cells to the TME. The granulocytes recruited to the TME are mainly neutrophils ($CD45^{hi}$/PD-$L1^{low}$/$CD16/32^{-}$) and pre-neutrophils (PD-$L1^{int}$/$CD16/32^{-}$) with PMN-MDSCs ($CD45^{hi}$/PD-$L1^{high}$/$CD16/32^{+}$) constituting a small fraction of the total granulocytes in the *mIDH1* glioma TME.

Supplementary Table S1. Metal conjugated antibodies used in this study

Label	Target	Clone
143Nd	CD11a	H155-78
147Sm	CD48	HM48-1
148Nd	CD16/32	93
149Sm	Ly-6B	7/4
151Eu	CD103	QA17A24
155Gd	CxCR2	SA044G4
158Gd	Ly-6A/E (Sca-1)	D7
161Dy	CD90.2/Thy-1.2	30-H12
163Dy	CD162	4RA10
173Yb	CD43	S11
170Er	CD170/siglec-F	S17007L
141Pr	Ly-6G	1A8
142Nd	CD11c	N418
144Nd	CD115	AFS98
145Nd	CD4	RM4-5
146Nd	F4/80	BM8
150Nd	CD24	M1/69
152Sm	CD3e	145-2C11
153Eu	CD274 (PD-L1)	10F.9G2
154Sm	TER-119 (Glycophorin A)	TER-119
156Gd	CD14	Sa14-2
159Tb	CD184 (CXCR4)	L276F12
160Gd	CD45R (B220)	RA3-6B2
162Dy	Ly-6C	HK1.4
164Dy	CD62L (L-selectin)	MEL-14
165Ho	CD161 (NK1.1)	PK136
166Er	CD117 (ckit)	2B8
167Er	CD335 (NKp46)	29A1.4
168Er	CD8a	53-6.7
169Tm	CD206 (MMR)	C068C2
171Yb	CD44	IM7
172Yb	CD11b (Mac-1)	M1/70
174Yb	Ly-6G/C (Gr-1)	RB6-8C5
175Lu	CD38	90
176Yb	FceR1a	Mar-1
209Bi	I-A/I-E	M5/114.15.2
89Y	CD45	30-F11

Supplementary Table S2. Fluorescence-conjugated antibodies used in the study

Antibody	Manufacturer	Cat #
PerCP/Cy5.5 anti-mouse CD3e	Biolegend	100328
PE anti-mouse CD4	Biolegend	100512
APC anti-mouse CD8	Biolegend	100712
Alexa fluor 700 anti-mouse CD45	Biolegend	103112
PE/Cy7 anti-mouse CD45	Biolegend	103114
APC anti-mouse/human CD11b	Biolegend	101212
Pacific BlueTM anti-mouse/human CD11b	Biolegend	101224
PE anti-mouse/human CD11b	Biolegend	101208
PE-Dazzle Ly-6G/Ly-6C (Gr-1)	Biolegend	108452
FITC anti-mouse Ly-6G/Ly-6C (Gr-1)	Biolegend	108406
PE anti-mouse Ly-6G	Biolegend	127608
PerCP/Cy5.5 anti-mouse Ly-6C	Biolegend	128012
APC anti-mouse F4/80	Biolegend	123116
FITC anti-mouse I-A/I-E	Biolegend	107606
APC anti-mouse CD80	Biolegend	104714
PE anti-mouse CD86	Biolegend	105008
PE anti-mouse/human CD45R/B220	Biolegend	103208
APC anti-mouse CD117 (c-Kit)	Biolegend	105812
APC-Cy7 anti-mouse Ly-6A/E (Sca-1)	Biolegend	108126
PE anti-mouse Lineage Cocktail with Isotype Ctrl	Biolegend	133303
PE-Cy7 anti-mouse CD16/32	Biolegend	101302
APC anti-mouse CD274 (Rat anti LyG25)	Biolegend	124311
PE anti-mouse CD124 (IL-4 Receptor alpha)	Biolegend	144803
Anti-Mouse CD16/32 (FC Block)	Biolegend	101302

Supplementary Table S3. Gating strategies used to define immune cells

Immune Cells	Gating Strategy
CD4 T cells	$CD45^+$, $CD3^+$, $CD4^+$
CD8 T cells	$CD45^+$, $CD3^+$, $CD8^+$
Monocytes	$CD45^+$, $CD14^+$
Macrophages	$CD45^+$, $CD11b^+$, $F4/80^+$
M1 Macrophages	$CD45^+$, $CD11b^+$, $CD206^-$, $MHCII^+$
M2 Macrophages	$CD45^+$, $CD11b^+$, $CD206^+$, $Arginase^+$
PMN MDSCs	$CD45^+$, $CD11b^+$, $Ly6G^+$, $Ly6C^{low}$
Monocytic MDSCs	$CD45^+$, $CD11b^+$, $Ly6G^-$, $Ly6C^+$
MDSCs	$CD45^+$, $CD11b^+$, $Gr\text{-}1^+$
DCs	$CD45^+$, $CD11c^+$, $MHCII^+$
B cells	$CD45^+$, $CD19^+$, $CD38^+$
NK Cells	$CD45^+$, $CD11b^{int}$, $NK1.1^+$
HSC	Lin^-, $c\text{-}kit^+$, $Sca\text{-}1^+$, $Thy1.1^{low}$
CLP	$c\text{-}kit^{low}$, $Sca\text{-}1^{low}$, Lin^-, $IL\text{-}7R\alpha^+$
MP	$c\text{-}kit^+$, $Sca\text{-}1^-$, Lin^-, $Thy1.1^{low}$
GMP	Lin^-, $IL\text{-}7R\alpha^-$, $c\text{-}kit^+$, $Sca\text{-}1^-$, $CD34^+$, $FcyRII/III^{high}$

Supplementary Table S6. Expressing vectors used in this study

Plasmid number	Repository/source	Plasmid Name	Insert
124259	Addgene	pT2-shATRX-GFP	shATRX
124261	Addgene	pT2-shP53	shP53
124257	Addgene	pKT-IDH1(R132H)-IRES-Katushka	IDH1
LV455868	Applied Biological Materials	pLenti-GIII-CMV-RFP-2A-Puro	CSF3